

# Development of Zn-IV-Nitride Semiconductor Materials and Devices

Thesis by  
Amanda M Shing

In Partial Fulfillment of the Requirements  
for the Degree of  
Doctor of Philosophy



California Institute of Technology  
Pasadena, California

Defended May 9, 2016



## Acknowledgments

I want to acknowledge my advisors Harry Atwater and Nate Lewis for letting me join their groups and work freely on the different projects I've encountered. In addition, Bruce Brunshwig and Kimberly Papadantonakis have been most valuable in getting the important things done. I appreciate the funding and instrumentation from the Molecular Materials Research Center in addition to instrumentation in the Joint Center for Artificial Photosynthesis. Funding and support from the Dow Chemical Company has made most of my work possible. I thank Robert Wright and Rebekah Feist for leading the Caltech-Dow Earth-Abundant Semiconductor partnership for the numerous years and graduate projects it has helped complete. I thank Alireza Ghaffari for technical instrument assistance, and Mike Roy, Steve Olsen, Carol Garland, Rick Gerhart, and Jeff Groseth for their professional work and analysis. I thank Barbara Miralles, Tiffany Kimoto, Jennifer Blankenship, Christy Jenstad, Liz Jennings, and Lyann Lau for their administrative assistance in planning great parties and important events.

The Earth-Abundant Semiconductor Team members Yulia Tolstova, Stefan Omelchenko, Naomi Coronel, Lise Lahourcade, Samantha Wilson, Jeff Bosco, Seokmin Jeon and Greg Kimball have given good insight and advice to areas of my projects. In taking care of the instruments I've used, the sputterer GLAs Ivan Moreno, Ke Sun, Erik Verlage, Matt McDowell, Josh Spurgeon, Sunita Darbe, Jing-Shun Huang, Carissa Eisler, and Naomi have helped tremendously in getting my experiments done. And our XPS GLA team members Noah Plymale, Jonathan Thompson, Annelise Thompson, Adam Nielander, Joseph Beardslee, and Judy Lattimer have spent many hours with me fixing and troubleshooting the instruments in the subbasement.

In the Atwater Group, Ana Brown, Matt Escarra, Dennis Callihan, Mike Kelzenberg, Dan Turner-Evans, Cris Flowers, Rob Usiskin, Ryan Briggs, and Jim Fakonas have been fun in creating Muskrat Water together. I thank Michelle Sherrott, Will Whitney, Anna Beck, Joelson Wong, Laura Kim, Ghazaleh Kafaie Shirmanesh, Kelly Mauser, Ragip Pala, Howard Lee, Jeremy Brouillet, Krishnan Thyagarajan, Yury Tokpanov, Georgia Papadakis, Dagny Fleischman, Seyoon Kim, Colton Bukowsky, Nick Batara, Siying Peng, Hal Emmer, and Muhammad Alam for letting me use their offices without bounds. I acknowledge Victor Brar for absolutely nothing. I thank Ruzan Sohkoyan for her tea and Rebecca Saive, Chris Chen, and Carissa Eisler for good advice and conversation. Although I have worked less immediately with them, I thank Sophia Cheng, Rebecca Glauddell, Phil Jahelka, Yonghwi Kim, Wei-Hsiang Lin, Anya Miskovets, Sisir Yalamanchili, Kate Fountaine, Pilar Espinet, Yury Lu, Giulia Tagliabue, Deep Jariwala, Artur Davoyan, Ali Naqavi, Emily Warmann, Jonathan Grandidier, Stan Burgos, Emily Kosten, Min Seok Jang, Andrew Leenheer, Morgan Putnam, Kelsey Whitesell, Raymond Weitekamp, Matt Shaner, and Matt Sheldon for their contribution to the Atwater Group and scientific perspective.

The many Lewis Group members I have worked with have also influenced my graduate career. I thank Dan Torelli and Victoria Dix for their group scheduling efforts. Our safety officers Josh Wiensch and Annelise Thompson deserve credit for the lab citations they need to continuously correct. Ron Grimm, Matt Bierman, Liz Santori, James McKone, Rob Coridan, and Azhar Carim have set up and maintained important Lewis Group equipment. Craig Wiggenhorn and Teddy Huang have been fantastic organizers for the Lewis Group Hiking Club. I thank Emily Warren and Mike Deceglie for their tomato plant, the Chalcogenators: Jesus Velazquez, Jimmy John, and Adam Pietrick for helping develop Group Retreat meetings, and Kyra Lee and Heather McCaig for BI subbasement office conversations. The postdocs “Hurricane” Shane Ardo, Betar Gallant, CX Xiang, Keith Wong, Mike Walter, Nick Strandwitz, Bryce Sadtler, Mike Rose, Qixi Mi, Fan Yang, Ke Sun, Miguel Caban-Acevedo, Mita, Dasog, Sonja Francis, and James Blakemore have shown me the different definitions of scientific research. I thank Fadl Saadi and Ethan Simonoff for their many laughs

during group meeting, and Noah for his enthusiasm- especially during Group Retreat. The JCAP lab members Michael Lichterman, Xinghao Zhou, Jingjing Jiang, Paul Nunez, and Matthias Richter have been generous for letting me invade their offices, and my actual Noyes officemates Leslie O’Leary, Jacob Good, Heather Audesirk, and Chance Crompton for keeping the office quiet.

I thank my friends and lab mates Chris Roske and Sid Creutz for the puzzles and adventures. I thank my friends and roommates Magnus Haw, Chris Marotta, David Case, Miki Nakajima, and Alex Xu for dealing with my dirty dishes and clutter. I thank Magnus Haw for Magnus Bear, Lava Hippo, and his efforts in everything. My friends and Materials Science/Applied Physics classmates Yinglu Tang and Yulia Tolstova have been good company for homework, racket sports, and pig feet. I acknowledge Lisa Mauger, Andrew Hoff, Samantha Johnson, Kevin Fiedler, Sunita Darbe, John Lloyd, Viki Chernow, and honorary Matt Gethers for exciting volleyball games, hanging out, and department ranting.

Alice Downing has been supportive in helping me with essential resources that I couldn’t get elsewhere. Harry Gray and the Solar Army have been instrumental in expanding my knowledge of solar cells and how to disseminate this knowledge to others.

Finally, I thank my many family members for their constant support and encouragement. My grandparents, parents, aunts, uncles, and sisters have provided me with plenty of food that has helped sustain my energy and give me time to do other things. They have bought me all the things that I am too cheap to buy for myself and given me all the necessary and unnecessary electronic devices for me to do my work. They make sure I am well entertained and cared for and that I am not taking anything too seriously to get upset about. They have helped me write this thesis to the end.

# Abstract

This thesis details explorations of the materials and device fabrication of Zn-IV-Nitride thin-films. Motivation in studying this materials series originates from its analogous properties to the III-Nitride semiconductor materials and its potential applications in photonic devices such as solar cells, light emitting diodes, and optical sensors. Building off of initial fabrication work from Coronel, Lahourcade, et al.,  $\text{ZnSn}_x\text{Ge}_{1-x}\text{N}_2$  thin-films have shown to be a non-phase-segregating, tunable alloy series and a possible earth-abundant alternative to  $\text{In}_x\text{Ga}_{1-x}\text{N}$  alloys. This thesis discusses further developments in fabrication of  $\text{ZnSn}_x\text{Ge}_{1-x}\text{N}_2$  alloys by three-target co-sputtering and molecular beam epitaxy, and the resulting structural and optoelectronic characterization. Devices from these developed alloys are also highlighted.

Initial fabrication was based on the reactive radio-frequency (RF) sputtering technique and was limited to two-target sources and produced nanocrystalline films. Progression to three-target reactive RF co-sputtering for  $\text{ZnSn}_x\text{Ge}_{1-x}\text{N}_2$  ( $x < 1$ ) alloys is presented, where three-target co-sputtered alloys follow the structural and optoelectronic trends of the initial alloy series. However, three-target co-sputtering further enabled synthesis of alloys having  $< 10\%$  atomic composition ( $x < 0.4$ ) of tin, exhibiting non-degenerate doping. The electronic structure of sputtered thin-film surfaces for the alloy series were also characterized by photoelectron spectroscopy to measure their work functions and relative band alignment for device implementation.

Low electronic mobilities, degenerate carrier concentrations, and limited photoreponse may stem from the defective and nanocrystalline nature of the sputtered films. To improve crystalline quality, films were grown by molecular beam epitaxy (MBE). MBE  $\text{ZnSn}_x\text{Ge}_{1-x}\text{N}_2$  films on sapphire and GaN were epitaxially grown, overall displaying single-crystalline quality films, higher electronic mobilities, and lower carrier

concentrations. Throughout experimentation, devices from both sputter deposited and MBE  $\text{ZnSn}_x\text{Ge}_{1-x}\text{N}_2$  alloys films were constructed. Attempts at solid-state and electrochemical devices are described. Devices exhibited some photoresponse, providing a positive outlook for employment of  $\text{ZnSn}_x\text{Ge}_{1-x}\text{N}_2$  alloys in solar cells or photon sensors.

## Published content:

AM Shing, HA Atwater, “Zn-IV-Nitride growth by MBE” (in progress)

AM Shing, NS Lewis, HA Atwater, “Chemical and electrochemical stability of ZnSnN<sub>2</sub>” (in progress)

AM Shing, Y Tolstova, NS Lewis, HA Atwater, “ZnSnN<sub>2</sub> work function by photoelectron spectroscopy and variations with surface treatment ” (pending submission to J. Phys. Chem. C 2016)

AM Shing, SA Ardo, M Boccard, C Battaglia, C Ballif, HA Atwater, NS Lewis “High-Aspect-Ratio Structures for Tandem Amorphous-Silicon— Crystalline-Silicon Solar Cells” (in progress)

Y Tolstova, ST Omelchenko, AM Shing, HA Atwater “Heteroepitaxial Growth of Pt and Au thin films on MgO single crystal by bias-assisted sputtering” (accepted Scientific Reports 2016)

AM Shing, NC Coronel, NS Lewis, HA Atwater, “Semiconducting ZnSn<sub>x</sub>Ge<sub>1-x</sub>N<sub>2</sub> alloys prepared by reactive radio-frequency sputtering,” APL Mat. 3, 076104, 2015

AM Shing, NC Coronel, NS Lewis, HA Atwater, “Fabrication and Characterization of ZnSn<sub>x</sub>Ge<sub>1-x</sub>N<sub>2</sub> Alloys for Light Absorbers” IEEE 42nd PVSC Manuscript, 2015

NC Coronel, L Lahourcade, KT Delaney, AM Shing, HA Atwater, “Characterization of ZnSn<sub>x</sub>Ge<sub>1-x</sub>N<sub>2</sub> for Photovoltaic Absorber Layers,” IEEE PVSC 38th Manuscript, 003204, 2012

# Contents

<b>Abstract</b>	<b>vi</b>
<b>1 Introduction</b>	<b>1</b>
1.1 Motivation and Background . . . . .	1
1.2 Scope of thesis . . . . .	6
<b>2 Reactive RF sputtered ZnSnN<sub>2</sub></b>	<b>7</b>
2.1 Variations in ZnSnN <sub>2</sub> growth . . . . .	7
2.2 Degenerate semiconducting properties . . . . .	12
2.3 Photoconductivity . . . . .	13
2.4 Improvements in reactive RF sputtered ZnSnN <sub>2</sub> films . . . . .	16
<b>3 Non-degenerate semiconducting ZnSn<sub>x</sub>Ge<sub>1-x</sub>N<sub>2</sub> alloys</b>	<b>17</b>
3.1 Comparison across the series . . . . .	18
3.2 Non-degenerate low-tin alloys . . . . .	20
3.3 Raman shifts for ZnSn <sub>x</sub> Ge <sub>1-x</sub> N <sub>2</sub> alloys . . . . .	23
3.4 ZnSn <sub>x</sub> Ge <sub>1-x</sub> N <sub>2</sub> solid-state devices . . . . .	26
<b>4 Electronic properties by photoelectron spectroscopy</b>	<b>29</b>
4.1 ZnSnN <sub>2</sub> work function measurements . . . . .	32
4.2 ZnSn <sub>x</sub> Ge <sub>1-x</sub> N <sub>2</sub> work function measurements . . . . .	43
4.3 XPS band alignment measurements . . . . .	44
<b>5 Growth by molecular beam epitaxy</b>	<b>45</b>
5.1 Motivation for MBE . . . . .	45

5.2	Growth of epitaxial hexagonal $\text{ZnSn}_x\text{Ge}_{1-x}\text{N}_2$ by MBE . . . . .	48
5.3	Improvements for MBE Growth . . . . .	65
<b>6</b>	<b>Chemical and electrochemical stability and non-aqueous electrochem-</b> <b>istry</b>	<b>66</b>
6.1	Chemical stability . . . . .	67
6.2	Non-aqueous photoelectrochemistry . . . . .	67
6.3	Aqueous electrochemistry . . . . .	70
<b>7</b>	<b>Summary and conclusions</b>	<b>73</b>

# List of Figures

1.1	Zn-IV-Nitrides theoretical band gaps at 0K versus $a$ lattice parameters plotted against the experimental data for III-Nitrides. Reference: Delaney, “First-Principles Assessment of Earth-Abundant Nitrides.” . . .	3
1.2	The $\text{ZnSnN}_2$ wurtzite lattice with a) $\text{Pna}2_1$ symmetry, b) $\text{Pmc}2_1$ symmetry, and c) random Zn and Sn cation positioning. Larger atoms are cations, while smaller grey/black atoms represent nitrogen. Reference: Coronel, Thesis 2015. . . . .	5
2.1	a) Scanning electron micrograph of sputtered $\text{ZnSnN}_2$ surface. Surface features are $< 100\text{nm}$ in width. b) High temperature growth comparison. Larger surface grain sizes are apparent. . . . .	9
2.2	Atomic force micrographs of $\text{ZnSnN}_2$ surfaces a) 45 min b) 5 hours c) 16 hours d) 24 hours and their RMS roughness. Each square is $5 \times 5$ micron area, with the vertical scale from $-60\text{nm}$ to $60\text{nm}$ . Longer growth times resulted in rougher surface morphologies. . . . .	10
2.3	XRD of $\text{ZnSnN}_2$ sputtered on various substrates: graphene, Ti foil, FTO, and Si. Diffractograms indicate the nanocrystalline films orient in the $\text{ZnSnN}_2$ [001] direction on all tested substrates. . . . .	11
2.4	Comparison of growths with sputter chamber base pressure $>10^{-5}$ torr and $<10^{-7}$ torr. Growths with higher base pressure result in less preferential (002) orientation. . . . .	12

2.5	Resistivity vs temperature measurement for ZnSnN <sub>2</sub> . Assuming the mobility of the nanocrystalline sputtered films throughout the temperature analysis constant, the resistivity is proportional to the carrier concentration. This indicates that the carrier concentration does not decrease an order of magnitude. . . . .	14
2.6	Photoconductivity response of a solid-state ZnSnN <sub>2</sub> device at 5V bias using white LED light. A long response time is observed when the light is turned on and persistent photoconductivity is observed after turning the light off. . . . .	15
3.1	a) X-ray diffraction of shifting (002) ZnSn <sub>x</sub> Ge <sub>1-x</sub> N <sub>2</sub> peak with varying Sn concentration. b) Position of the 2Theta peak versus Sn concentration. A linear relationship is apparent. . . . .	19
3.2	Optical band gap versus percent atomic concentration of Sn. Measurements for samples prepared for this work are indicated by (●) while measurements reported in (Reference: Coronel et al., IEEE PVSC 2012) for samples measured and modeled using the same methods employed herein are indicated by (Δ). . . . .	20
3.3	a) Resistivity of ZnSn <sub>x</sub> Ge <sub>1-x</sub> N <sub>2</sub> thin films with varying Sn concentration. The resistivity increases exponentially with decreasing Sn content. b) Respective carrier concentration, calculated assuming n-type carriers with 1 cm <sup>2</sup> V <sup>-1</sup> s <sup>-1</sup> mobility. . . . .	21

3.4	Resistivity vs. temperature for samples with a) 5% atomic concentration of Sn and b) 16% atomic concentration of Sn. The samples exhibit behavior characteristic of semiconductors, with increasing resistivity over decreasing temperature. The change in resistivity over decreasing temperature indicate 16%atSn samples acting degenerately and 5%at Sn samples acting non-degenerately. c) Arrhenius plot (log of resistivity versus inverse temperature) for 5%at and 16%at samples. The greater slope of the 5%at Sn trend line indicates a greater activation energy for thermalized carriers. . . . .	23
3.5	Raman spectra for $\text{ZnSnN}_2$ and several low-tin $\text{ZnSn}_x\text{Ge}_{1-x}\text{N}_2$ alloys. Peak 5 from $\text{ZnSnN}_2$ and Peak 4 from the $\text{ZnSn}_x\text{Ge}_{1-x}\text{N}_2$ alloys may be artifacts from the detector limits. Existence of broad peaks represent disorder from either random cation positioning or random stacking of pseudospin layers. . . . .	24
3.6	Raman shift vs Sn content for quaternary $\text{ZnSn}_x\text{Ge}_{1-x}\text{N}_2$ alloys. Peak 1 and Peak 2 show correlation with % atomic Sn, while the relationship is less clear for Peak 3 and Peak 4. . . . .	25
3.7	An asymmetric IV curve from a tungsten/low-tin alloy Schottky device resulting from some carrier transport blocking. . . . .	27
3.8	Amorphous growth of a low-tin $\text{ZnSn}_x\text{Ge}_{1-x}\text{N}_2$ . . . . .	28
4.1	UPS work function (bars) of vacuum-transferred $\text{ZnSnN}_2$ samples with standard deviations (red). Overlaid are the surface concentrations of C (green triangle) and O (blue dot). . . . .	33
4.2	XPS SECs used to determine work function and verify UPS values. . . . .	33

4.3	Comparison of UPS spectra for vacuum-transferred ZnSnN <sub>2</sub> samples with spectra obtained for ZnSnN <sub>2</sub> samples after a) air exposure, b) nitrogen plasma treatment, and c) argon-ion sputter treatment. Short air exposure was for < 10 seconds in atmosphere, and long air exposure was for < 1 minute. The spectra were obtained using a He I source ( $h\nu = 21.21$ eV). . . . .	34
4.4	ZnSnN <sub>2</sub> work function measurements of one sample after progressive air exposures and accumulated adventitious carbon and oxygen. Work functions increase with the oxygen surface concentration. For the plasma-treated film, chemical bonding with oxygen . . . . .	36
4.5	Work function of various ZnSnN <sub>2</sub> samples before and after air exposure. Across several sample, air exposed work functions have greater values than vacuum transferred values. . . . .	37
4.6	High resolution XPS regions of N 1s, Zn 2p, Sn 3d, and valence band regions for freshly vacuum-transferred samples and Ar <sup>+</sup> sputter-treated samples. . . . .	38
4.7	UPS spectrum of the ZnSnN <sub>2</sub> valence-band region. Significant electron emission is seen between the VBM and the Fermi level, indicating occupied surface states in the gap region for vacuum-transferred samples. Air-exposed surfaces do not have such high electron counts, showing that oxygen passivates these gap states. . . . .	39
4.8	Energy-band diagram for the vacuum/ZnSnN <sub>2</sub> interface prior to equilibration with mid-gap surface states (left) and after equilibration (right). Electrons from the bulk fill the empty surface states, causing the bands to bend upward, reducing the valence band onset at the surface from a degenerate position to 1.2 eV. . . . .	40

4.9	ZnSnN <sub>2</sub> Fermi level alignment with various common semiconductors and redox couples on the vacuum energy scale and Normal Hydrogen Electrode scale. In vacuum, the ZnSnN <sub>2</sub> valence band at the surface would be 1.2 eV below the Fermi level; however, the bulk ZnSnN <sub>2</sub> valence band is expected to be further below the Fermi energy. Reference: Al-Hilli, 2009. . . . .	41
4.10	Composition, work function, and valence band onset values for argon-ion sputter-cleaned surfaces. Due to the decrease in nitrogen, other elements show increased contribution in the composition. . . . .	42
4.11	a) Band gap, b) carrier concentration, and c) valence band onset versus work function for individual samples. . . . .	43
5.1	Schematic of nitride molecular beam epitaxy instrument. An RF atom source supplied with nitrogen gas provides activated nitrogen to the deposition, while elemental metals and semi-metals are emitted from the evaporation sources. The chamber is equipped with in-vacuo RHEED to analyze the surface structure of the substrates and films. . . . .	47
5.2	RHEED patterns for (001) Sapphire and GaN templates for both [11-20] and [10-10] azimuthal directions. . . . .	48
5.3	Grazing XRD of initial, nitrogen-flux limited ZnSnN <sub>2</sub> MBE growth on sapphire compared to ZnSnN <sub>2</sub> powder pattern. . . . .	49
5.4	ZnSnN <sub>2</sub> RHEED in [11-20] and [10-10] azimuthal directions for sapphire and GaN. For ZnSnN <sub>2</sub> on sapphire, spots instead of streaks are present due to 3D film growth, likely from the lattice mismatch between ZnSnN <sub>2</sub> and sapphire. . . . .	51

5.5	a) Simulated EMAPS (Reference: Zuo and Mabon, <i>Micosc. Microanal.</i> 2004) of selected area transmission diffraction pattern for a wurtzite GaN lattice compared to b) $\text{ZnSn}_x\text{Ge}_{1-x}\text{N}_2$ RHEED transmission diffraction. The $\text{ZnSn}_x\text{Ge}_{1-x}\text{N}_2$ RHEED reflections have similar symmetry as the simulated hexagonal GaN pattern for transmission diffraction, as expected for the $\text{ZnSn}_x\text{Ge}_{1-x}\text{N}_2$ crystal structure. . . . .	51
5.6	RHEED of $\text{ZnSn}_x\text{Ge}_{1-x}\text{N}_2$ on GaN in the [1120] and [10-10] azimuthal directions. All conditions grew smooth 2D films. Lattice parameter differences for $\text{ZnSnN}_2$ can be seen in the RHEED streak misalignment, where the $\text{ZnSnN}_2$ on [11-20] . . . . .	52
5.7	RHEED [11-20] azimuthal directions for Zn grown on GaN and sapphire. Better lattice matching is seen For $\text{ZnSn}_x\text{Ge}_{1-x}\text{N}_2$ on sapphire, at higher tin concentrations, 3D growth ensued. Going to lower tin concentrations and higher germanium concentrations, diffraction resulted from 2D film surfaces. Potential causes may be from relaxation from strained islands to coalescing into a smooth surface. . . . .	53
5.8	a) XRD patterns of MBE grown $\text{ZnSn}_x\text{Ge}_{1-x}\text{N}_2$ on (001) c-sapphire. Sole presence of (002) peak indicates films are oriented. b) The presence of periodic Pendellosung oscillations on the (002) peak indicate sharp interfaces between the film and substrate and pseudomorphic growth representative of heteroepitaxy. . . . .	54
5.9	a) XRD patterns of MBE grown $\text{ZnSn}_x\text{Ge}_{1-x}\text{N}_2$ on wurtzite (001) GaN. b) Pendellosung oscillations are present on both $\text{ZnSnN}_2$ and $\text{ZnSn}_x\text{Ge}_{1-x}\text{N}_2$ alloys indicating pseudomorphic growth. The $\text{ZnSnN}_2$ <i>a</i> parameter has less lattice mismatch with GaN than sapphire, allowing epitaxial growth to occur, and 2D, smooth films. . . . .	55
5.10	XRD of sputtered $\text{ZnSnN}_2$ compared to improved MBE growths on sapphire and GaN. Sputtered peak positions do not match with MBE films potentially due to strain. . . . .	56

5.11	Plot of $\text{ZnSn}_x\text{Ge}_{1-x}\text{N}_2$ peak positions vs tin concentration show sputtered films have a different shift compared to MBE films potentially due to strain. . . . .	57
5.12	Phi scan of MBE55 on sapphire with psi angle 60 degrees. Six major peaks appear, representing hexagonal symmetry. b) The sapphire phi scan. Alignment of peaks indicate a hexagon-on-hexagon growth. c) Phi scan of MBE64G on GaN. The intersecting substrate and film peaks also reflect hexagon-on-hexagon growth. . . . .	58
5.13	HRTEM of film-GaN substrate interface exhibiting epitaxy for $\text{ZnSnN}_2$ MBE46G. The image shows the film at $\sim 30\text{nm}$ thick with clean heteroepitaxy to the substrate, and single-crystal quality. Contrast in the film exhibits the strain present. TEM courtesy of Carol M Garland. . . . .	59
5.14	HRTEM of $\text{ZnSn}_x\text{Ge}_{1-x}\text{N}_2$ MBE57G on GaN substrate. It contains qualities similar to the HRTEM of $\text{ZnSnN}_2$ film on GaN. . . . .	60
5.15	Selected Area Electron Diffraction of a) $\text{ZnSnN}_2$ MBE46G and b) $\text{ZnSn}_x\text{Ge}_{1-x}\text{N}_2$ MBE57G on GaN. The substrate reflections are clearly separated from the $\text{ZnSnN}_2$ reflections, showing the lattice mismatch, whereas the $\text{ZnSn}_x\text{Ge}_{1-x}\text{N}_2$ reflections sit on the substrate peaks. The amorphous rings in the $\text{ZnSnN}_2$ SAD are from epoxy applied to the sample. Diffraction spots are labeled for the orthorhombic $\text{ZnSn}_x\text{Ge}_{1-x}\text{N}_2$ . . . . .	61
5.16	Resistivity increases with a similar trend as the sputtered films. Stoichiometry for sputtered films was measured by EDS, where stoichiometry for MBE films were measured by XPS. . . . .	62
5.17	Photoactivity using a 2-point probe at a 3V bias with 405nm laser illumination on low-tin MBE $\text{ZnSn}_x\text{Ge}_{1-x}\text{N}_2$ films on a) sapphire and b) GaN. . . . .	63
5.18	a) Raman for alloys and b) comparison to sputtered $\text{ZnSn}_x\text{Ge}_{1-x}\text{N}_2$ films	64

6.1	Optical micrographs of sputter-fabricated ZnSnN <sub>2</sub> films on sapphire after sitting in a) 10% HF solution and b) concentrated HCl. Pitting in the film is due to ZnSnN <sub>2</sub> dissolving in these acids. . . . .	68
6.2	Photoelectrochemical cell with three-electrode setup. Image credit: CX Xiang . . . . .	69
6.3	Photoelectrochemical devices in a) ferrocene and b) cobaltocene cells. ZnSnN <sub>2</sub> electrodes display ohmic behavior for both redox couples. The smaller concentrations of oxidized species (FeCp <sub>2</sub> <sup>+</sup> and CoCp <sub>2</sub> <sup>+</sup> ) cause the limiting current at negative potentials. No photoresponse is apparent. . . . .	69
6.4	Photoelectrochemical tests of a) ZnSnN <sub>2</sub> and b) ZnSn <sub>x</sub> Ge <sub>1-x</sub> N <sub>2</sub> electrodes. A small photoresponse is apparent for both materials. . . . .	70
6.5	Cyclic voltammograms for a ZnSnN <sub>2</sub> electrode in aqueous media. The decrease in current over two repeated cycles indicates that the electrode is affected by corrosion or oxidation. At -2V vs the solution potential, hydrogen bubbles begin to evolve. . . . .	71
6.6	Cyclic voltammograms for fresh ZnSnN <sub>2</sub> electrodes in a) the anodic region and b) the cathodic region in aqueous media. Oxidative effects may be the cause of the current decrease after multiple sweeps in a), while degradation through reductive pathways may be the case for b). The current values differ because they are not normalized to electrode areas, and because there is less ferricyanide for reduction to occur. Thus, the cathodic instability is less dramatic. . . . .	72
1	KF Flange for sputterer window. . . . .	84
2	Arm attachment for adjusting the height of the new stage holder. . . . .	85
3	The new stage holder for the sample holder adapter. . . . .	85
4	The sample holder adapter for the Kratos sample holder. . . . .	86
5	The Cu puck Kratos sample holder. . . . .	86

6	The assembly of sputterer substrate platform (transparent) with sample holder adapter (green) and Kratos sample holder (Cu puck). The substrate platform assembly sits on a new stage holder (light blue), which is held to the sputterer translation arm by the stage support (grey) . . .	87
7	The assembly in the sputterer load-lock and path where the suitcase arm travels. . . . .	87
8	The vacuum suitcase, equipped with a SAES ion and getter pump, used to transfer XPS/UPS samples. . . . .	88

# List of Tables

1.1	Theoretical and measured lattice parameters of substrates and orthorhombic-based Zn-IV-N <sub>2</sub> . ZnSnN <sub>2</sub> results are taken from a sputter deposited film on a sapphire substrate. . . . .	4
2.1	Parameters for ZnSnN <sub>2</sub> sputter deposition and resulting stoichiometry.	9
4.1	Average values for work function, valence band onset, and adventitious carbon and oxygen surface coverage. The error listed represents one standard deviation. * Listed are VBMs determined by both XPS and UPS. XPS penetrates deeper into the material bulk and has less convolution with surface states and satellite peaks, so it is a more representative VBM value than that of UPS [A]. We reported the UPS value to demonstrate the surface affects from the different treatments, which are not as apparent in the XPS derived VB onset because the XPS signal averages photoelectrons from deeper into the bulk of the film. **Although the linear extrapolation of the main body leads to this result, a significant tail of states into band gap exist. . . . .	42
4.2	Average sample properties . . . . .	43
5.1	Growth conditions and resulting stoichiometries by XPS for improved crystalline MBE samples. Samples labeled MBE###G used GaN substrates, while the remaining are on sapphire. * denotes surface stoichiometry different from bulk. . . . .	50

5.2	Interfacial lattice parameters calculated from SAED of MBE films on GaN substrates. MBE ZnSnN <sub>2</sub> films are strained on GaN and an average lattice parameters are given. Films are oriented on the substrate, so only $a$ and $c$ parameters can be calculated. . . . .	60
-----	--	----

# Chapter 1

## Introduction

### 1.1 Motivation and Background

$\text{In}_x\text{Ga}_{1-x}\text{N}$  alloys are used in light-emitting diodes (LEDs) and sensors, where alloying enables tuning of the band-gap energy,  $E_g$ , within the range set by the two binary compounds,  $\text{InN}$  ( $E_g = 0.69$  eV) and  $\text{GaN}$  ( $E_g = 3.51$  eV), allowing applications such as colored LEDs [1] and solar cells. However, the large lattice mismatch (10%) between  $\text{InN}$  and  $\text{GaN}$  results in phase segregation for In-rich alloys, limiting the ability of the  $\text{In}_x\text{Ga}_{1-x}\text{N}$  alloys to cover the full visible spectrum [2], especially the regime for efficient solar energy conversion.

The LED industry has attempted to overcome this limitation by using  $\text{Al}_x\text{Ga}_y\text{In}_{1-x-y}\text{P}$  alloys that span the longer wavelength regions for red and orange colors. However, the  $\text{Al}_x\text{Ga}_y\text{In}_{1-x-y}\text{P}$  series has a limited accessible range due to the appearance of an indirect gap [3]. The range of band gap energies that the  $\text{Al}_x\text{Ga}_y\text{In}_{1-x-y}\text{P}$  alloys covers does not overlap with the  $\text{In}_x\text{Ga}_{1-x}\text{N}$  alloys, leaving a gap [4] at 550-600nm (2-2.3 eV) and preventing a full spectrum of light emitting diodes. This gap is known as the “Green Gap.” Several research initiatives to fill the Green Gap involve different types of  $\text{In}_x\text{Ga}_{1-x}\text{N}$  growth to prevent the In segregation [5]. However, new II-IV-Nitride  $\text{ZnSn}_x\text{Ge}_{1-x}\text{N}_2$  alloy materials show promise as earth-abundant alternatives to  $\text{In}_x\text{Ga}_{1-x}\text{N}$  that resolve the Green Gap problem.

The Group II-IV-Nitrides is an emerging alloy series that is analogous to the well-characterized Group III-Nitrides series with the Group III elements (In or Ga)

replaced by a combination of a Group II element (Zn) and a Group IV element (Sn or Ge). Calculations performed using density functional theory (DFT) for the  $\text{ZnSn}_x\text{Ge}_{1-x}\text{N}_2$  alloys have predicted that the band gaps of the  $\text{ZnSn}_x\text{Ge}_{1-x}\text{N}_2$  alloy series from  $\text{ZnSnN}_2$  to  $\text{ZnGeN}_2$  will span the range of 1.4-3.1 eV, which includes the full visible spectrum, the Green Gap, and suggest utility as photovoltaic absorber materials, LEDs, or optical sensors [6]. Figure 1.1 displays the calculated band gaps versus  $a$  lattice parameters for the Zn-IV-Nitride alloys against the experimental parameters for the III-Nitrides [7]. The plot also shows less lattice mismatch between the calculated lattice parameters for  $\text{ZnSnN}_2$  and  $\text{ZnGeN}_2$  (estimated 5%) than the 10% mismatch between  $\text{InN}$  and  $\text{GaN}$ , exhibiting less potential for quaternary alloys to phase segregate.  $\text{ZnSn}_x\text{Ge}_{1-x}\text{N}_2$  alloys additionally have the benefit of being composed of more abundant elements than  $\text{In}_x\text{Ga}_{1-x}\text{N}$  or  $\text{Al}_x\text{Ga}_y\text{In}_{1-x-y}\text{P}$  alloys, which may become either too difficult or too expensive to produce as In consumption increases. Specifically, the least abundant element in  $\text{ZnSn}_x\text{Ge}_{1-x}\text{N}_2$  alloys is Ge ( $1.5 \text{ mg kg}^{-1}$ ), which is about six times more abundant in the Earth's crust than In ( $0.25 \text{ mg kg}^{-1}$ ) [8].

Experimental progress in fabricating and characterizing the materials has been underway.  $\text{ZnSnN}_2$  is an emerging earth-abundant semiconductor material, having its initial fabrication reported in 2012 [9, 10, 11]. Interest in  $\text{ZnSnN}_2$  had been generated from calculations of its electronic structure, estimating a direct band gap of  $\sim 1.4\text{-}2$  eV and a low electronic effective mass [12, 13], making it an attractive high-mobility electronic material.  $\text{ZnSnN}_2$  has been synthesized by methods such as vapor-liquid-solid (VLS) plasma-assisted growth [11], reactive radio-frequency (RF) sputtering, and molecular-beam epitaxy (MBE) [14, 15]. Monoclinic crystal structures have been observed for MBE thin-film growth on yttrium-doped zirconia substrates, but with droplets of metal residue on the film surfaces [15]. Orthorhombic crystal structures have been observed for VLS growths and sputtered material, although VLS growth yields discontinuous islands on top of Zn-Sn from melt whereas sputtering provides more homogeneous films. Both techniques create crystallites on the order of 100 nm or less.

Investigations of sputtered material by Coronel et al. on (001) oriented sapphire

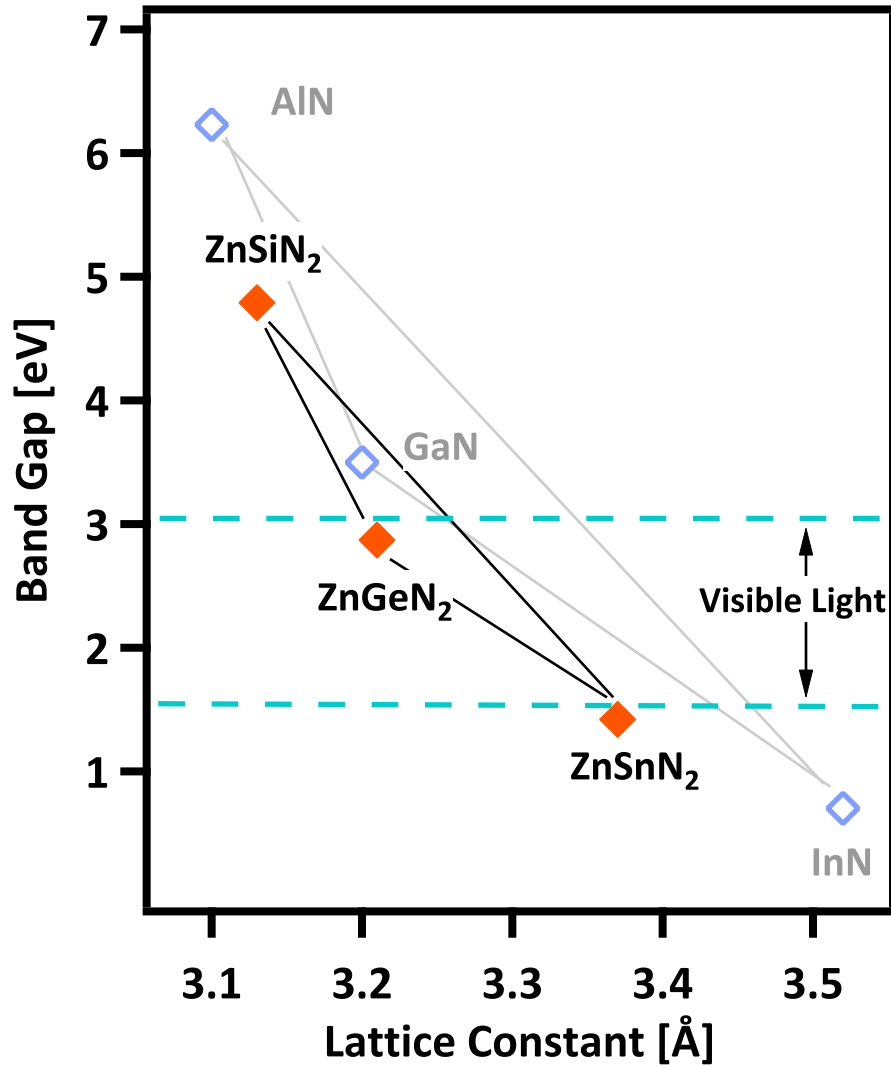


Figure 1.1: Zn-IV-Nitrides theoretical band gaps at 0K versus  $a$  lattice parameters plotted against the experimental data for III-Nitrides. Reference: Delaney, “First-Principles Assessment of Earth-Abundant Nitrides.”

and GaN templates on sapphire displayed primarily (002) oriented nanocrystalline films. Nanocrystallinity was hypothesized as an effect of deposition rather than the initial lattice mismatch of the ZnSnN<sub>2</sub> and the substrates (Table 1.1). Furthermore, films were removed from the substrates and converted to powder-form to obtain an XRD powder pattern, confirming the expected orthorhombic structure derived from a

wurtzite, hexagonal-based lattice. Yet the broad peaks obtained still concealed some of the finer peak splittings that would define the lattice having  $Pna2_1$  symmetry,  $Pmc2_1$  symmetry, or a mixed or random Zn and Sn cation positioning in the lattice. Figure 1.2 shows the differences between the structures.

All methods to date have reported stoichiometric  $ZnSnN_2$  samples that exhibit majority carrier concentrations of electrons at or above degenerate doping levels [16, 14]. Limitations in  $ZnSnN_2$  semiconductor device quality also lie in its reported low mobilities  $< 10 \text{ cm}^2\text{V}^{-1}\text{s}^{-1}$  [16]. Development of the  $ZnSnN_2$  growth may provide more insight into its potential in device applications.

	Theoretical Lattice Parameter [nm]			Measured Lattice Parameter [nm]		
	<i>a</i>	<i>b</i>	<i>c</i>	<i>a</i>	<i>b</i>	<i>c</i>
Sapphire	-	-	-	0.4758 [17]	-	1.2991 [17]
GaN	-	-	-	0.3189 [17]	-	0.5185 [17]
$ZnSnN_2$	0.6721 [9]	0.5842 [9]	0.5459 [9]	0.6766 [18]	0.5857 [18]	0.5485 [18]
$ZnGeN_2$	0.638 [13]	0.545 [13]	0.522 [13]	0.5454 [19]	0.6441 [19]	0.5124 [19]

Table 1.1: Theoretical and measured lattice parameters of substrates and orthorhombic-based Zn-IV-N<sub>2</sub>.  $ZnSnN_2$  results are taken from a sputter deposited film on a sapphire substrate.

Interest in  $ZnGeN_2$  has spanned back to the 1970s, attempting to fabricate  $ZnGeN_2$  as a GaN alternative [20, 21]. To synthesize  $ZnGeN_2$ , various techniques have been implemented including vapor phase reaction with  $NH_3$  [22], high-pressure alloying of  $Ge_3N_4$  with Zn [20] or  $Zn_3N_2$  [23], MOCVD [24], and sputter deposition [25]. These techniques have led to crystalline material in forms of high-pressure-formed pellets, micron-sized needles, and thin films. However, material properties vary with fabrication method. Electronic quality  $ZnGeN_2$  material for device incorporation is still in development.

Reactive RF sputtered quaternary  $ZnSn_xGe_{1-x}N_2$  alloys ( $0 < x < 1$ ) were first fabricated by Coronel et al. in 2011 [26] as uniform, crystalline thin-films on sapphire and GaN templates on sapphire. Structurally, in these quaternary alloys, as  $x$  is decreased from 1, Ge atoms would substitute into lattice positions on Sn sites. Throughout the alloy series, these sputtered  $ZnSn_xGe_{1-x}N_2$  alloys have experimentally

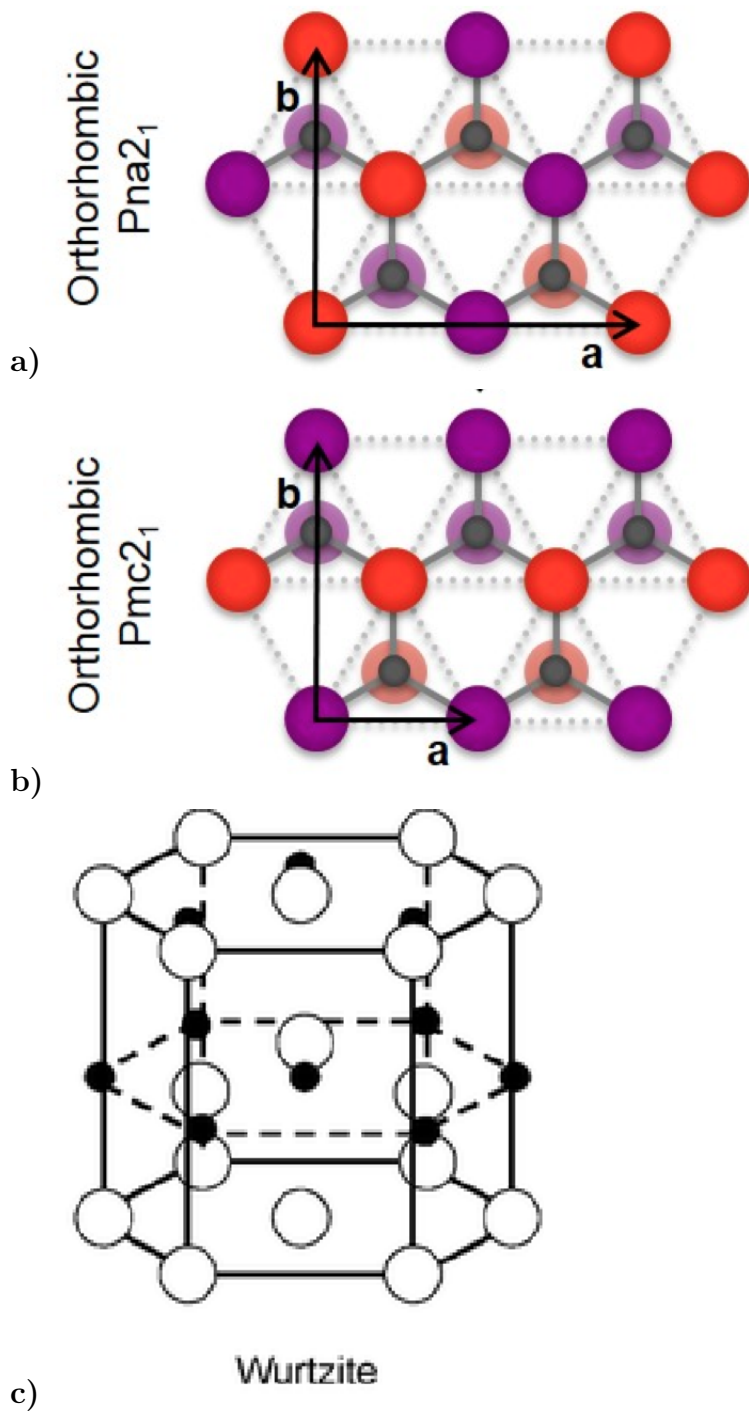


Figure 1.2: The  $ZnSnN_2$  wurtzite lattice with a)  $Pna2_1$  symmetry, b)  $Pmc2_1$  symmetry, and c) random Zn and Sn cation positioning. Larger atoms are cations, while smaller grey/black atoms represent nitrogen. Reference: Coronel, Thesis 2015.

demonstrated stability against phase segregation—a significant advantage relative to  $\text{In}_x\text{Ga}_{1-x}\text{N}$  alloys [26, 27]. Furthermore, sputtered  $\text{ZnSn}_x\text{Ge}_{1-x}\text{N}_2$  thin-films from  $0 \leq x \leq 1$  also display tunable band gaps, including the band gaps that cover the Green Gap region. This tunability characteristic is a prerequisite for colored LEDs and higher-efficiency multijunction solar cells. Additionally,  $\text{ZnSn}_x\text{Ge}_{1-x}\text{N}_2$  can achieve it with earth-abundant elements.

## 1.2 Scope of thesis

This thesis discusses further developments in fabrication of earth-abundant  $\text{ZnSn}_x\text{Ge}_{1-x}\text{N}_2$  alloys, the resulting structural and optoelectronic characterization of these thin-films, as well as devices attempted using the materials as active layers. Chapter 2 focuses on  $\text{ZnSnN}_2$  and variations with the reactive RF sputter deposition growth. Chapter 3 highlights reactive RF sputtered  $\text{ZnSn}_x\text{Ge}_{1-x}\text{N}_2$  films fabricated from three elemental Zn, Sn, and Ge targets. It reviews how three-target co-sputtered alloys follow the structural and optoelectronic trends of the initial alloy series. Three-target co-sputtering further enables synthesis of non-degenerately-doped semiconducting alloys having <10% atomic composition ( $x=0.4$ ) of tin. Chapter 4 extends the work of sputtered  $\text{ZnSn}_x\text{Ge}_{1-x}\text{N}_2$  characterization to photoelectron spectroscopy. Using x-ray photoelectron spectroscopy and ultraviolet photoelectron spectroscopy, the work function of  $\text{ZnSnN}_2$  is determined, defining where its Fermi Level sits in comparison to other semiconductors, metals, and redox couples.  $\text{ZnSn}_x\text{Ge}_{1-x}\text{N}_2$  work function values are similar in energy. Chapter 5 presents improved material quality and first quaternary alloys grown by molecular beam epitaxy (MBE). Structural and optoelectronic properties are explained, in addition to their comparison with sputtered materials. Finally, Chapter 6 explores the chemical and electrochemical stability of these  $\text{ZnSnN}_2$  thin films and photoelectrochemical device performance.

## Chapter 2

# Reactive RF sputtered ZnSnN<sub>2</sub>

This chapter reviews parameters considered for ZnSnN<sub>2</sub> thin-film growth by reactive RF sputtering, and the resulting structural and electronic characteristics. These varied parameters include substrate type, substrate temperature, sputter deposition time/thickness, and sputterer chamber base pressure. ZnSnN<sub>2</sub> carrier degeneracy and photoresponse are also reviewed. Suggestions for additional parameters to vary for improved films are presented at the end of this chapter.

### 2.1 Variations in ZnSnN<sub>2</sub> growth

Initial ZnSnN<sub>2</sub> growths performed with reactive RF sputtering used c-plane sapphire and GaN template substrates held at 175C [9]. Elemental Zn and Sn targets with 99.99+% purity were metal source materials, while an Ar/N plasma provided the activated nitrogen. Conditions listed in 2.1 show deposition parameters and average stoichiometric data. Stoichiometry ranged over samples due to varying sputterer chamber and metal target conditions.

Samples were analyzed with x-ray diffraction (XRD) using a Bruker D2 Phaser table top XRD and an X'pert PANalytical Hi-Res XRD, both employing Cu K alpha radiation ( $\lambda = 1.5418 \text{ \AA}$ ). X-ray diffraction probed the films' structure and performance through peak position and peak FWHM. In general, only substrate peaks and the reflection from the ZnSnN<sub>2</sub> (002) planes and their higher reflections appeared, indicating well oriented films. Using the (002) peak width in a Debye-Scherrer ap-

proximation, crystallite size can be estimated. The Debye-Scherrer approximation is derived for powder samples, rather than thin-films on substrates. However, calculations estimate nanocrystalline grains on the order of tens of nm, agreeing with average grain size from SEM images taken of the surface of the films, seen in Figure 2.1.

Grain boundaries in semiconducting materials often result in low electron and hole mobilities and high recombination rates, as carriers do not have ordered lattices to travel through. Efforts to improve crystallinity and achieve larger grain sizes, and thus higher mobilities and longer minority carrier lifetimes, were attempted by growing with higher substrate temperatures. Substrate temperature affects the ad-atom residence time and mobility. Increased ad-atom mobility allows atoms to travel across the substrate and find their energetic minima, potentially producing larger grain sizes as nucleation sites will have formed more thermodynamically favored clusters. Table 2.1 shows deposition parameters for higher temperatures and compared to those for 175C. Figure 2.1 shows that the high temperature growth increased the surface grain morphology compared to ZnSnN<sub>2</sub> deposited at 175C. Surface features increased by 3-4 times size for 375C samples. Although improvements in surface morphology were noted with a higher temperature, FWHM of the (002) peak did not reduce noticeably, inferring the persistence of nanocrystalline grain sizes. Mobilities did not increase noticeably either. GaN thin-films grown by MOCVD can achieve FWHM value lower than 200 arcsec, and ZnSnN<sub>2</sub> peaks only attained FWHM of  $\sim 0.3$  deg (180 arcmin or 1080 arcsec), leaving much room for improvement. Studies in high temperature growth were limited. Challenges in higher temperature growth lie in thermal expansion mismatch of the film and substrate and stability of film during wide temperature variations. ZnSnN<sub>2</sub> was observed to delaminate from sapphire and GaN substrates for deposition and annealing temperatures above 400C.

It was also observed that at constant 175C deposition temperatures, but different growth times, surface features became more in rough as deposition time increased. Figure 2.2 displays atomic force micrographs of ZnSnN<sub>2</sub> surfaces from samples fabricated over various times. The root mean squared (RMS) roughness values show

	Substrate T	Pressure	Ar/N <sub>2</sub>	Power		Stoichiometry		
				Zn	Sn	%Zn	%Sn	%N
Standard Growth	175 C	3mT	1/3	44 W	74 W	27	27	46
High Temperature Growth	375C	3mT	1/3	94 W	74 W	28	32	41

Table 2.1: Parameters for ZnSnN<sub>2</sub> sputter deposition and resulting stoichiometry.

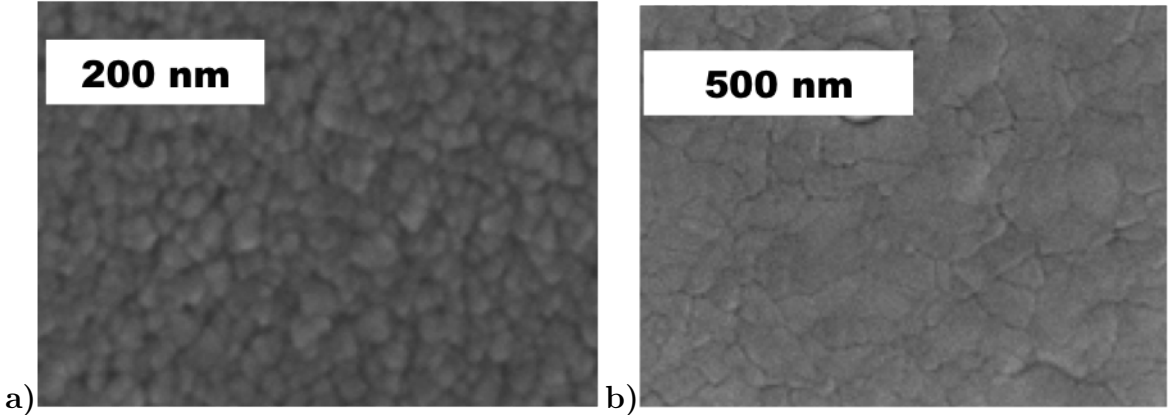


Figure 2.1: a) Scanning electron micrograph of sputtered ZnSnN<sub>2</sub> surface. Surface features are < 100nm in width. b) High temperature growth comparison. Larger surface grain sizes are apparent.

the surfaces are smoother at shorter deposition times. The advent of a rough surface promotes shadowing of regions, resulting in inhomogeneous nucleation and growth. Unshadowed regions grow faster than shadowed areas, causing topological differences and increasing RMS roughness as deposition time is increased. This is important because rough surfaces can not only act as recombination centers with greater area than smooth surfaces, but also, as interfacial/growth surfaces, rough surfaces can enhance defects in films subsequently grown on top.

In addition to sputtering temperature and time, substrates were also varied. Reactive RF sputtered thin-film studies began on c-plane sapphire and GaN template substrates, which were chosen due to their use in epitaxial nitride growth. Although ZnSnN<sub>2</sub> films, deposited within the explored parameters, were oriented with (002) ZnSnN<sub>2</sub> on (006) sapphire and (001) GaN substrates, they did not deposit epitaxially, as confirmed by TEM [18]. The thin-films did not indicate any continuous epitaxial dependence to the sapphire and GaN substrate lattices; therefore, other substrates were attempted to determine if the ZnSnN<sub>2</sub> exhibited the same mosaicity. Figure

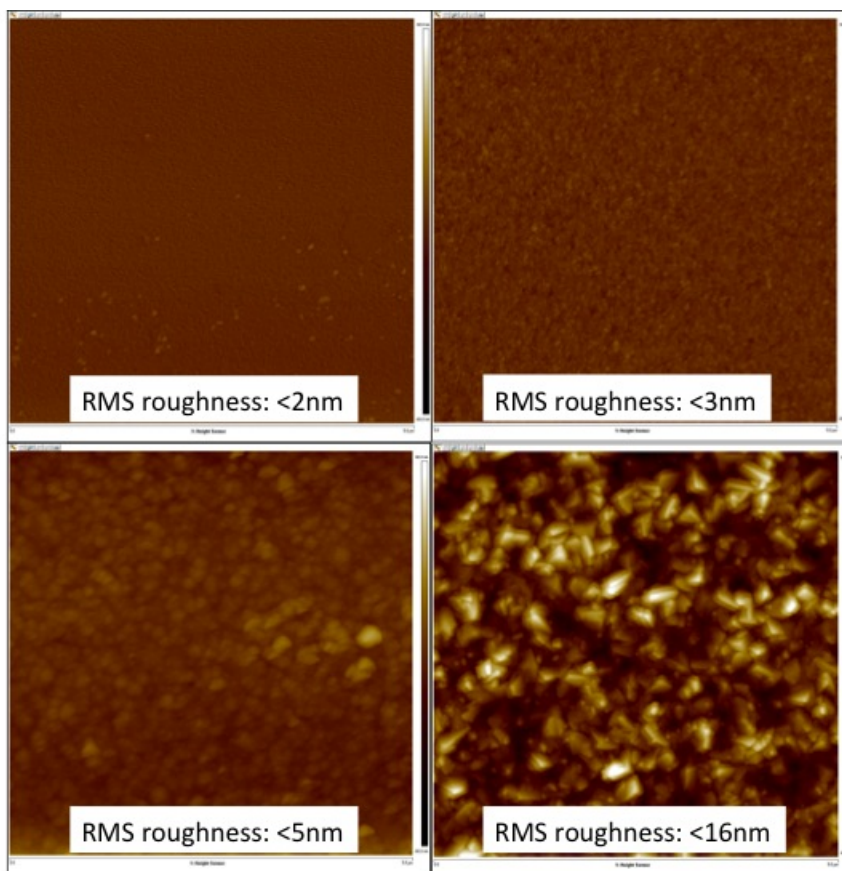


Figure 2.2: Atomic force micrographs of  $\text{ZnSnN}_2$  surfaces a) 45 min b) 5 hours c) 16 hours d) 24 hours and their RMS roughness. Each square is  $5 \times 5$  micron area, with the vertical scale from  $-60\text{nm}$  to  $60\text{nm}$ . Longer growth times resulted in rougher surface morphologies.

2.3 shows the XRD pattern of the  $\text{ZnSnN}_2$  sputter-deposited on various substrates. All substrates showed  $\text{ZnSnN}_2$  (002) oriented, despite the initial surface. Si surfaces were polished and epi-ready like the sapphire and GaN substrates, but rough fluorine-doped tin oxide and Ti foil substrates still allowed the same  $\text{ZnSnN}_2$  film mosaicity. Even flexible substrates, Ti foil and graphene on Cu foil, which did not always sit flat during deposition, did not inhibit the preferential orientation. It is possible that the energetic sputter bombardment destroyed the graphene monolayer, and investigations by Raman spectroscopy may be used to observe the resulting graphene quality. However, publications of device quality  $\text{In}_x\text{Ga}_{1-x}\text{N}$  sputtered films on graphene [1] demonstrate the feasibility of sputter deposition on graphene.

The ability to deposit nanocrystalline, (002) oriented  $\text{ZnSnN}_2$  on an array of sub-

strates, including dielectric, semiconducting, and metal surfaces, would prove useful for any future device fabrication. Heterostructures for  $\text{ZnSnN}_2$  and  $\text{ZnSn}_x\text{Ge}_{1-x}\text{N}_2$  have been proposed for photovoltaic devices [7] and  $\text{ZnSnN}_2$  deposited on  $\text{ZnSn}_x\text{Ge}_{1-x}\text{N}_2$  has been demonstrated to be physically feasible.

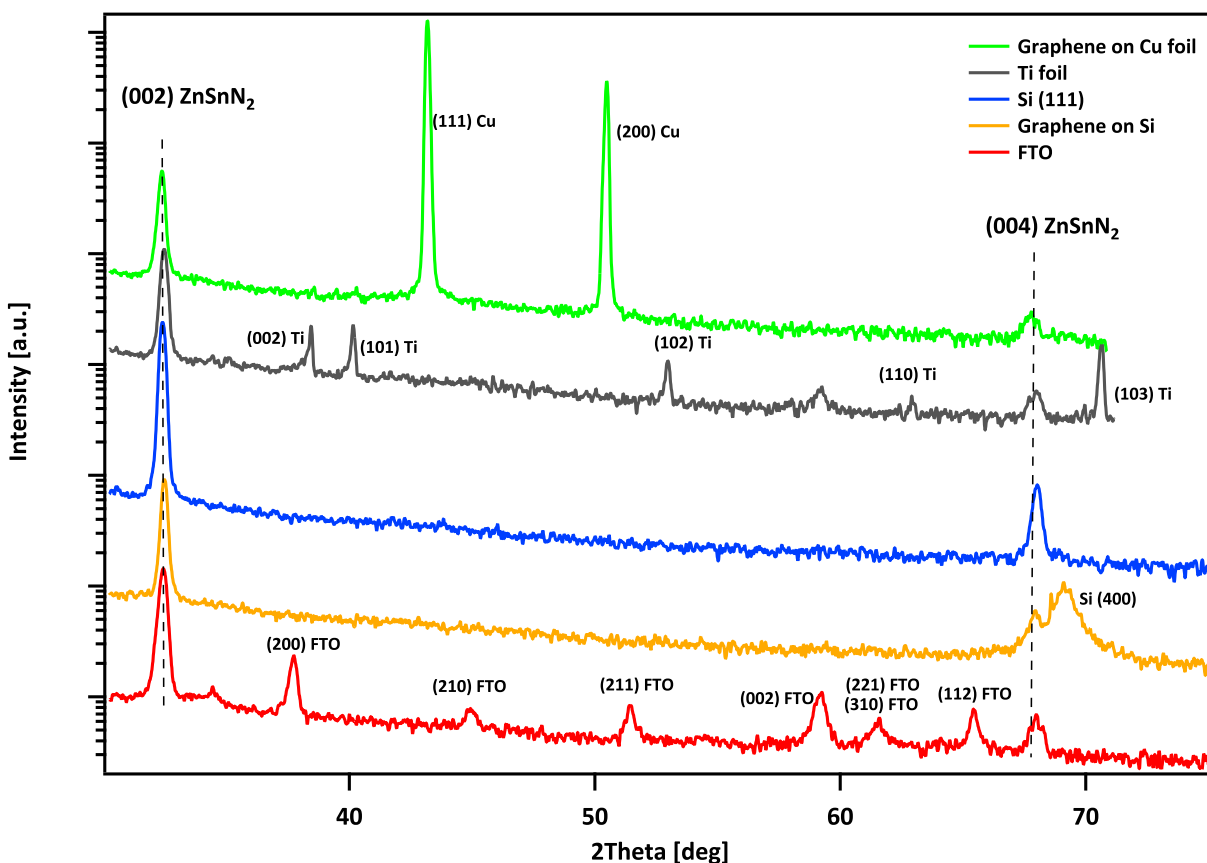


Figure 2.3: XRD of  $\text{ZnSnN}_2$  sputtered on various substrates: graphene, Ti foil, FTO, and Si. Diffractograms indicate the nanocrystalline films orient in the  $\text{ZnSnN}_2$  [001] direction on all tested substrates.

Finally, (002) oriented  $\text{ZnSnN}_2$  did not result from every growth. Figure 2.4 shows diffractograms of  $\text{ZnSnN}_2$  on sapphire with multiple preferred orientations. Samples were deposited with the same conditions, except for the base pressure of the sputter chamber. Higher base pressure sputtering yielded less preferential orientation with (002) planes, having reflections likely from the (211), (021), (041), and (421) planes present in the diffraction pattern.  $\text{ZnSnN}_2$  sputtering performed by other groups [28] at base pressures  $>10^{-6}$  torr similarly obtained polycrystalline films with a variety of

orientations.

Generally, higher base pressures entail more residual gas molecules that interfere with fabrication. Residual water or oxygen can collide with the sputtered atoms or adsorb onto the growing film, disrupting growth, which can enable less orientation. Higher base pressures also incorporate more impurities such as oxygen in films.

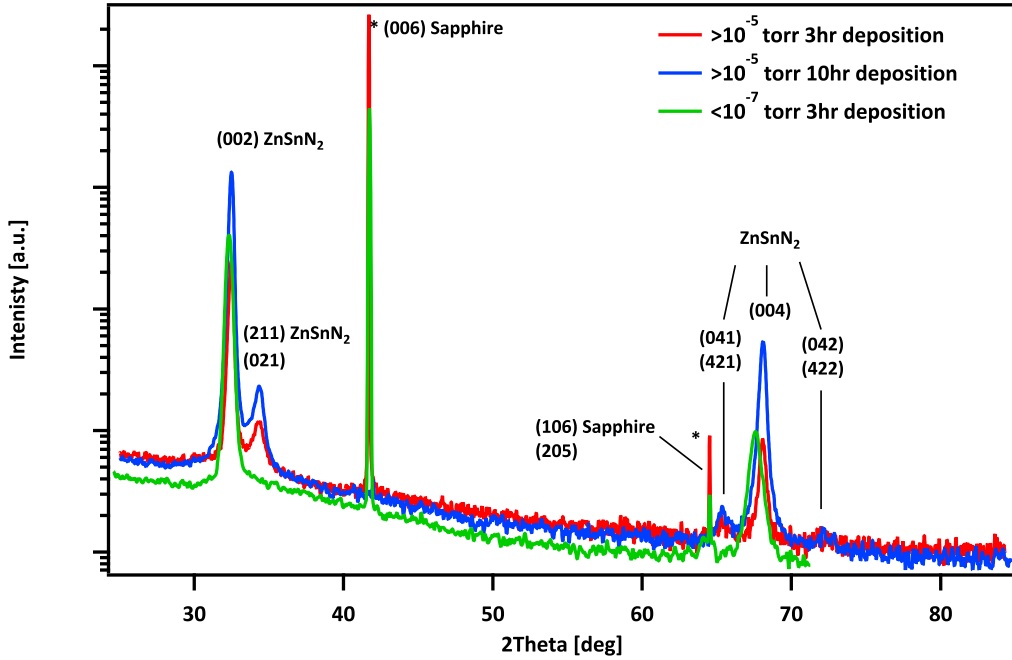


Figure 2.4: Comparison of growths with sputter chamber base pressure  $>10^{-5}$  torr and  $<10^{-7}$  torr. Growths with higher base pressure result in less preferential (002) orientation.

## 2.2 Degenerate semiconducting properties

Despite attempts to improve the crystalline quality and electronic properties, reactive RF sputtered ZnSnN<sub>2</sub> films all exhibited mobilities  $< 10 \text{ cm}^2\text{V}^{-1}\text{sec}^{-1}$ . Poor electron transport is attributed to the nanocrystalline nature of the sputtered films. Scattering from ionized atom cores also decreases mobility, as high ionization is expected from degeneracy. Degenerate values of carrier concentrations, above  $10^{18-19} \text{ cm}^{-3}$ , were measured for ZnSnN<sub>2</sub> films, potentially due to excess carriers from defects, impurities, or intrinsic properties.

For ZnSnN<sub>2</sub>, degenerate carrier concentrations led to ohmic behavior for all metal and liquid contacts attempted. This prevented common measurements such as capacitance-voltage tests or deep-level transient spectroscopy (DLTS) to probe for defect concentrations and energy levels.

To see if carriers would freeze out their donor energy levels, resistivity experiments were performed at lower temperatures. An MMR Hall System, where samples were placed in Van der Pauw configuration, was used to obtain resistivity vs. temperature data. Lower temperatures were achieved with an MMR vacuum refrigerator to prevent water vapor condensation. Figure 2.5 displays a measurement of resistivity vs temperature for ZnSnN<sub>2</sub> from room temperature down to 180K. Results show an increasing trend in resistivity with decrease in temperature, which infers less carriers thermalized into the conduction band at lower temperatures, decreasing the conductivity. This trend is characteristic of semiconductors, which in conjunction with ellipsometry measurements that indicate an existing band gap, provides evidence that ZnSnN<sub>2</sub> is a degenerate semiconductor rather than a metal.

However, the resistivity does not change an order of magnitude across the temperature range measured. Assuming the sputtered, nanocrystalline films have low mobility  $\mu$ , milliohm-cm resistivities for ZnSnN<sub>2</sub> are likely due to high carrier concentrations. Looking at the general resistivity equation (Equation 2.1), for mobility with tens of cm<sup>2</sup>V<sup>-1</sup>s<sup>-1</sup>, the exponential of a degenerate carrier concentration (10<sup>20</sup> cm<sup>-3</sup>) should omit the exponential of the charge term  $q$ , and resistivities are found in the milliohm-cm regime. Thus, going down to 180K, carrier concentration does not decrease an order of magnitude either.

$$\rho = \frac{1}{\sigma} = \frac{1}{(q(n\mu_n + p\mu_p))} \quad \text{Equation 2.1}$$

## 2.3 Photoconductivity

Hypothesized as potential solar materials, ZnSnN<sub>2</sub> films were tested for their photoactivity. Solid state devices were made with soldered indium contacts and probed with a Keithley 2602A System Source Meter. Devices were placed on a water cooling

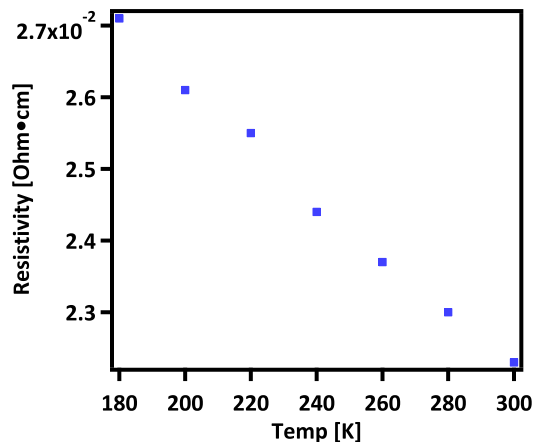


Figure 2.5: Resistivity vs temperature measurement for  $\text{ZnSnN}_2$ . Assuming the mobility of the nanocrystalline sputtered films throughout the temperature analysis constant, the resistivity is proportional to the carrier concentration. This indicates that the carrier concentration does not decrease an order of magnitude.

stage that maintained set temperatures. LEDs of various wavelengths were used for illumination. Figure 2.6 shows two-point probe data that revealed a slow transient photoresponse, identified as persistent photoconductivity, which occurs in  $\text{ZnSn}_x\text{Ge}_{1-x}\text{N}_2$  alloys with  $0 < x \leq 1$ . The slow photoresponse can be attributed to free carriers interacting with molecular desorption of oxygen molecules, as in  $\text{ZnO}$  [29, 30], and as illustrated in Scheme 1 (2.6). According to this mechanism, in the dark, an electron from the conduction band interacts with an oxygen molecule that adsorbs onto the surface. When the material is illuminated, an electron-hole pair is created and the hole recombines with the adsorbed-oxygen electron, leaving a remaining electron that increases the surface conductivity. When the optical excitation is terminated, molecular adsorption reoccurs, slowly capturing the free surface electrons.

Persistent photoconductivity can also be attributed to a combination of shallow and deep traps, as in  $\text{SrTiO}_3$ ,  $\text{GaN}$ , and  $\text{BiFeO}_3$  [31, 32, 33]. In this mechanism, a shallow trap constantly exchanges electrons with the conduction band, interfering with the generation and recombination of charge carriers at a deep trap. When illuminated, carriers generated from the deep trap will enter the conduction band states but begin to cycle into the shallow trap, causing a tailing onset for conductivity. When the optical excitation is terminated, electrons will begin to recombine. However, the

shallow trap competes for electrons in the conduction band, making it more difficult for electrons to reach the initial deep-trap state, resulting in persistent conductivity when in the dark. When in the conduction band, adsorbed oxygen may also play a role in addition to the shallow traps. Further analysis of persistent photoconductivity in the  $\text{ZnSn}_x\text{Ge}_{1-x}\text{N}_2$  alloys, including investigations of defect-state densities, trap states, and molecular adsorption performed in a vacuum environment or with controlled gases, could indicate the potential contributions of these two persistent photoconductivity mechanisms.

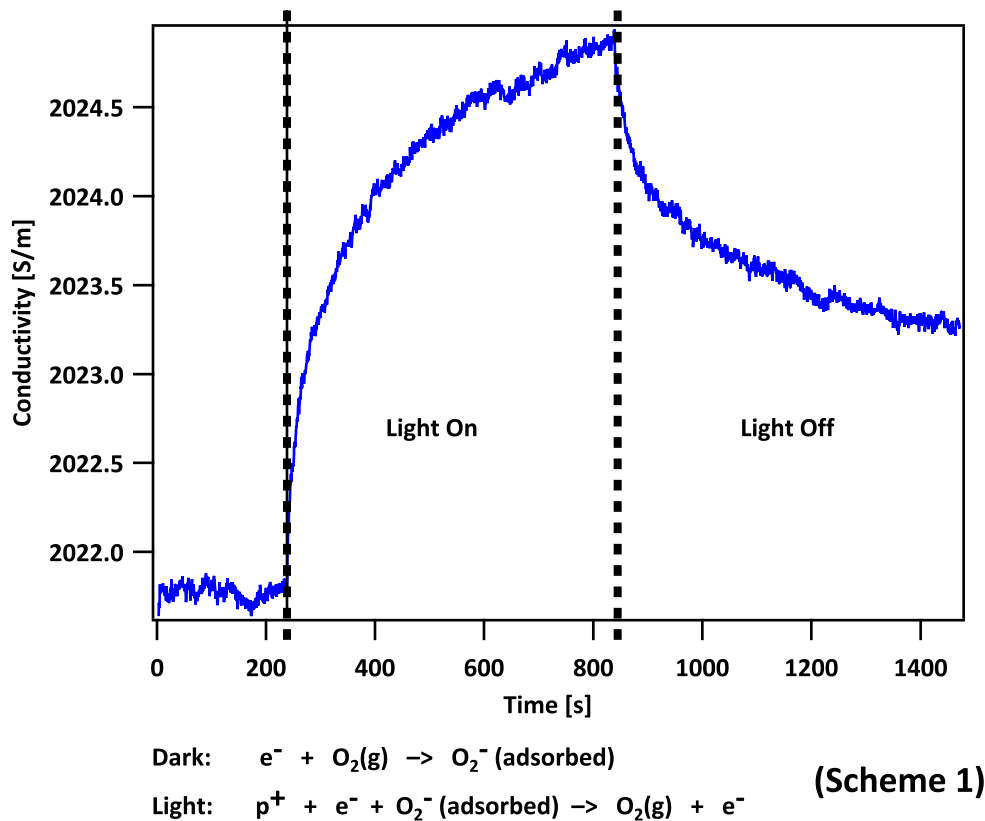


Figure 2.6: Photoconductivity response of a solid-state  $\text{ZnSnN}_2$  device at 5V bias using white LED light. A long response time is observed when the light is turned on and persistent photoconductivity is observed after turning the light off.

## 2.4 Improvements in reactive RF sputtered ZnSnN<sub>2</sub> films

Although several parameters were investigated to improve the reactive RF sputtered ZnSnN<sub>2</sub> crystallinity and mobility, many other variables could be explored. Substrate biases would enable more controls on deposition rate, and improve surface equilibration of ad-atoms. DC pulsed sputtering techniques may minimize arcing on targets that often create defects in films [34]. Buffer layers on substrates could decrease the severity of lattice mismatch and thermal expansion effects, and allow a greater range of substrate temperatures to be used. Appropriately matched buffer layers may also improve experiments regarding post-deposition annealing. The following chapters describe alternative steps taken to overcome material degeneracy and obtain higher crystallinity.

## Chapter 3

# Non-degenerate semiconducting $\text{ZnSn}_x\text{Ge}_{1-x}\text{N}_2$ alloys

As noted in Chapter 2, one of the challenges with  $\text{ZnSnN}_2$  has been the degenerate carrier concentration.  $\text{ZnSn}_x\text{Ge}_{1-x}\text{N}_2$  alloys fabricated by initial reactive RF two-target  $\text{Zn}_{0.75}\text{Sn}_{0.25}$  and Ge co-sputtering, although showed higher resistivities, their resistivities did not exceed 500 milliohm cm- still reflective of degenerate carrier concentrations. This chapter describes how three-target reactive RF sputtering shows equivalency to two-target sputtering, yet further achieves a range of low-tin (less than 10% atomic concentration Sn,  $x < 0.4$ ) alloys that exhibit non-degenerate semiconducting properties.

Three-target samples were deposited from separate Zn, Sn, and Ge targets of 99.99+% purity held at varying RF powers. Epitaxial-ready c-plane sapphire and GaN template substrates were prepared with an isopropanol rinse, then dried with a stream of nitrogen gas. Substrates were pumped in an AJA Sputterer chamber with base pressure  $< 2\text{E-}7$  Torr and heated to 175C before deposition. Sputtering plasma in the chamber was maintained with 1:3 argon:nitrogen gas flow ratio at 3 mTorr pressure. Samples were analyzed with x-ray diffraction using a Bruker D2 Phaser table top XRD and an X'pert PANalytical HRXRD, both employing Cu K alpha radiation ( $\lambda = 1.5418 \text{ \AA}$ ). The stoichiometry of the samples was measured using a scanning-electron microscope (SEM) equipped with an energy-dispersive spectrometer (EDS). Resistivities were measured using a four-point probe with tungsten tips. Resistivities

at varied temperatures were measured in a vacuum-sealed refrigerator with samples setup in the Van der Pauw configuration. Carrier type was determined by the hot-probe technique, where samples were electrically contacted to a multimeter while a heated ( $\sim 150\text{C}$ ) probe touched the sample surface near one of the electrodes. The sign of the voltage output indicated the carrier type. The dielectric functions were determined by spectroscopic ellipsometry, with the data modeled using a wavelength-by-wavelength layer on top of an alumina substrate layer.

### 3.1 Comparison across the series

Figure 3.1 shows the position of the  $\text{ZnSn}_x\text{Ge}_{1-x}\text{N}_2$  diffraction peak in the region of  $33^\circ < 2\theta < 34.5^\circ$ , indicating a linear shift in peak position with the Sn content of the films. Previous computational and experimental results support the assignments of an (002) orthorhombic  $\text{ZnSnN}_2$  peak at  $2\theta \approx 33^\circ$  and of an (002) orthorhombic  $\text{ZnGeN}_2$  peak at  $2\theta \approx 34.5^\circ$  [9, 26]. Vegard's law indicates that the corresponding peak for  $\text{ZnSn}_x\text{Ge}_{1-x}\text{N}_2$  alloys should lie between these two values. The (002) peak shifts linearly as the Sn content is varied for various  $\text{ZnSn}_x\text{Ge}_{1-x}\text{N}_2$  alloys having Sn atomic concentrations greater than 10% [26], indicating that no phase segregation occurred for alloys with Sn concentrations greater than 10%. The linear shift with Sn content shown in 3.1 indicates that phase segregation also does not occur for alloys with Sn atomic concentrations as low as 2%, thus extending the trend for the  $\text{ZnSn}_x\text{Ge}_{1-x}\text{N}_2$  alloy series. By using the full-width-half-max of the (002) peak in a Debye-Scherrer approximation, the film was inferred to consist of nanocrystalline grains that were tens of nm in size, which is consistent with the average grain size observed in SEM images of the surface of the films (Fig. 2.1).

The optical band gaps of the  $\text{ZnSn}_x\text{Ge}_{1-x}\text{N}_2$  alloys with  $< 15\%$  at. Sn were evaluated using spectroscopic ellipsometry. The optical constants  $n$  and  $k$  were obtained by fitting the polarization amplitude and shift. The absorption coefficients were calculated to be  $> 10^5 \text{ cm}^{-1}$ , indicating that the materials are well suited for use as thin-film light absorbers. Linear extrapolations from Tauc plots of the absorption co-

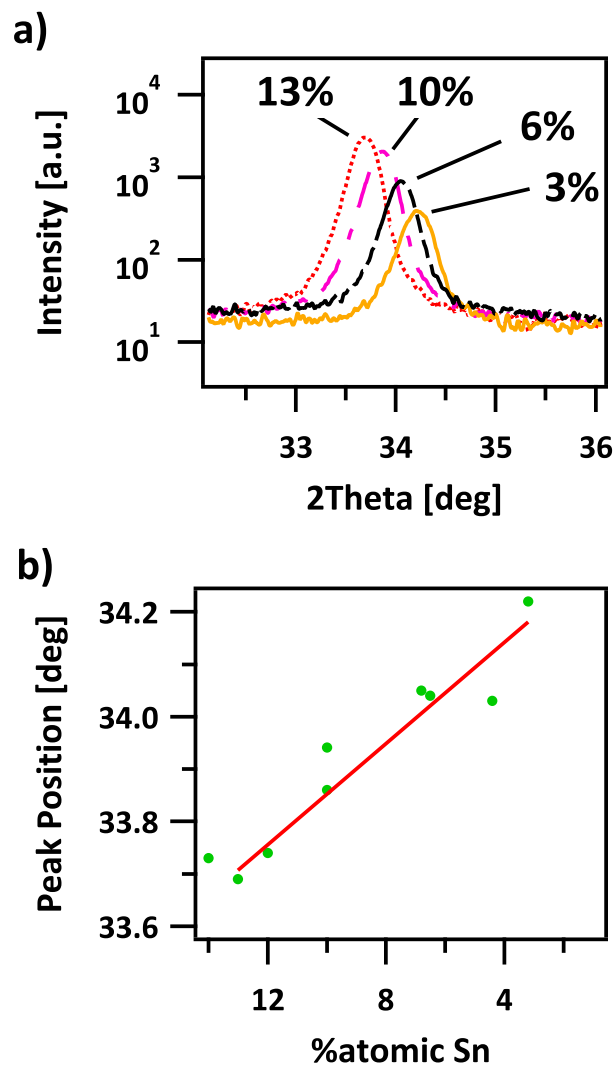


Figure 3.1: a) X-ray diffraction of shifting (002)  $\text{ZnSn}_x\text{Ge}_{1-x}\text{N}_2$  peak with varying Sn concentration. b) Position of the 2Theta peak versus Sn concentration. A linear relationship is apparent.

efficient squared versus energy showed that the low-Sn content alloys had direct band gaps ranging from  $\sim 2.2$  eV to 2.7 eV. Figure 3.2 plots the measured optical band gaps versus %at. Sn. Samples with  $\leq 7\%$  at. Sn exhibited higher band gaps than samples having  $\geq 10\%$  at. Sn, consistent with previous observations [26]. The increase in band gap with decreasing Sn content has been attributed to tighter binding in which substitution of smaller germanium atoms opens the band gap. The calculated partial density of states and band diagrams support this expectation for  $\text{ZnSnN}_2$  and

ZnGeN<sub>2</sub> [7], in which the density of states in the conduction band contributed by Sn extends further into the band gap than do the states contributed by Ge. Variations in the measured band gaps for a given composition may be attributed to the spread of samples, variations in strain, or to variations in substrates.

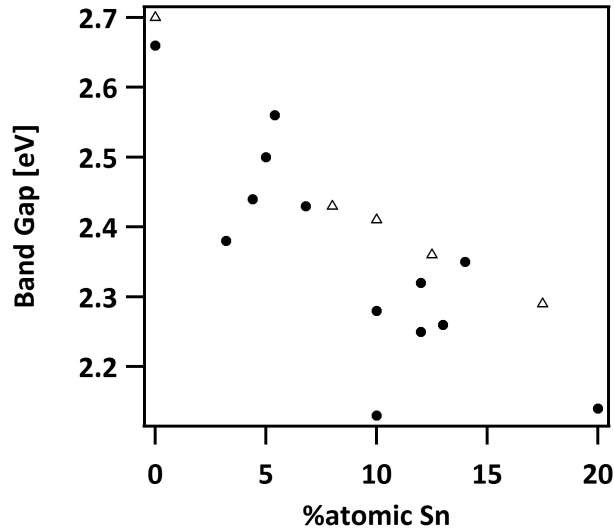


Figure 3.2: Optical band gap versus percent atomic concentration of Sn. Measurements for samples prepared for this work are indicated by (●) while measurements reported in (Reference: Coronel et al., IEEE PVSC 2012) for samples measured and modeled using the same methods employed herein are indicated by (Δ).

### 3.2 Non-degenerate low-tin alloys

Electrical measurements performed highlight interesting trends of the alloy series. In particular, resistivity measurements of low-tin samples reflect the carrier concentration effects and energetics. Four point probe measurements of samples produce resistivities ranging from milliohm-cm for ZnSnN<sub>2</sub> films, to MΩ-cm for low-tin ZnSn<sub>x</sub>Ge<sub>1-x</sub>N<sub>2</sub> alloys. Higher %at Sn samples are more conductive than samples with less Sn and more Ge content. Previous literature has also stated the high carrier concentration of the ZnSnN<sub>2</sub> films and their low mobilities, as well as the insulating nature of sputtered ZnGeN<sub>2</sub> films [21, 24].

Figure 3.3 shows the dependence of the resistivity measured at room temperature using a four-point probe as a function of the Sn content the samples.  $\text{ZnSnN}_2$  films exhibited resistivities of  $\sim 1$  milliohm-cm. The resistivity increased exponentially with decreasing Sn concentration to  $\sim 10^5 \Omega\text{-cm}$  for  $\text{ZnSn}_x\text{Ge}_{1-x}\text{N}_2$  alloys with  $<5\%$  at. Sn. Thus, decreases in the Sn content produced increases in the resistivity of the  $\text{ZnSn}_x\text{Ge}_{1-x}\text{N}_2$  alloys. This behavior is consistent with previous work in which high carrier concentrations and low mobilities have been observed in  $\text{ZnSnN}_2$  films, and is consistent with the insulating character previously reported for sputtered  $\text{ZnGeN}_2$  films [24]. The exponential increase in resistivity with reduced Sn concentration can be attributed to an increase in the band gap and to a reduction in the number of thermally activated carriers in the conduction band of the alloys. Furthermore, substituting Ge for Sn may reduce the number of electrons available for conduction because Ge is more electronegative than Sn, and hence Ge is a poorer electron donor than Sn. The exponential increase in resistivity with reduced Sn concentration may also reflect the location of the Fermi level ( $E_F$ ) with respect to the conduction-band energy ( $E_{cb}$ ) and with respect to excited carrier energies. If  $E_F$  were to remain the same while  $E_{cb}$  increases, then the resistivity would be expected to increase as additional Ge atoms are substituted for Sn.

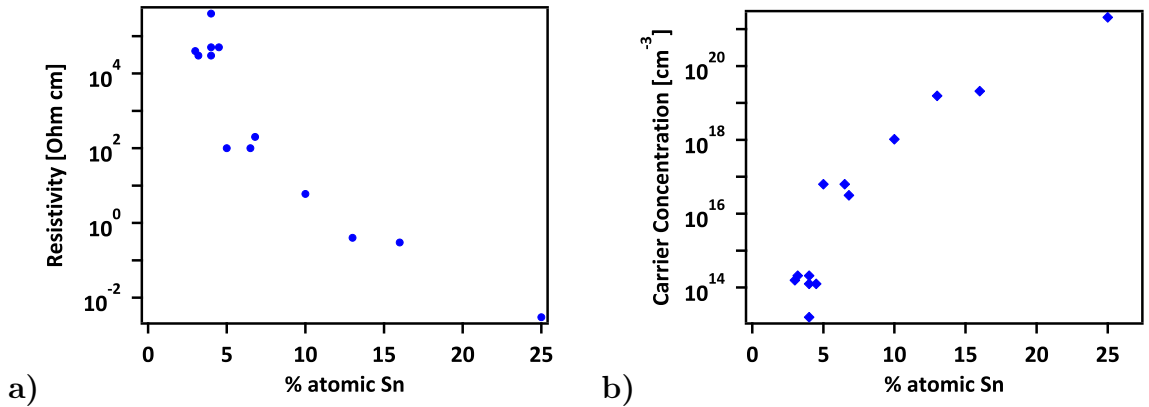


Figure 3.3: a) Resistivity of  $\text{ZnSn}_x\text{Ge}_{1-x}\text{N}_2$  thin films with varying Sn concentration. The resistivity increases exponentially with decreasing Sn content. b) Respective carrier concentration, calculated assuming n-type carriers with  $1 \text{ cm}^2\text{V}^{-1}\text{s}^{-1}$  mobility.

Figure 3.4 shows the dependence of the resistivity on temperature, for a sample

with 5% at. Sn and for a sample with 16% at. Sn. Samples that had a low Sn concentration exhibited exponential increases in resistivity as the temperature decreased (Figure 3.4a), while samples having a higher Sn concentration exhibited a linear increase in resistivity as the temperature decreased (Figure 3.4b). Furthermore, the resistivity of the sample with low Sn concentration varied by two orders of magnitude over the 160-300 K temperature range, while the resistivity of the sample with the higher Sn concentration only varied by 100 milliohm-centimeters over the same temperature range. These results are characteristic of semiconductors, for which the resistivity increases with decreasing temperature, as opposed to metals, for which the resistivity decreases as the temperature decreases. Furthermore, the exponential resistivity-temperature trend observed for the low-Sn sample indicates that low-Sn samples act non-degenerately, differing from the remainder of the  $\text{ZnSn}_x\text{Ge}_{1-x}\text{N}_2$  alloys that have a higher Sn content. Thus the electronic trends seen for the low-Sn quaternary alloys are distinctive within the  $\text{ZnSn}_x\text{Ge}_{1-x}\text{N}_2$  alloy series. Although the charge-carrier mobility affects the resistivity, and although mobilities typically increase with decreased temperature due to reduced phonon scattering, the presence of grain boundaries and defects in a nanocrystalline material such as these sputtered  $\text{ZnSn}_x\text{Ge}_{1-x}\text{N}_2$  alloys likely dominate the mobility term and diminish the change in mobility with temperature. Thus the resistivity of these samples mainly reflects the carrier concentrations in the films.

Figure 3.4c depicts an Arrhenius plot for the 5% at. Sn and 16% at. Sn samples. The slopes of the linearly fitted data yielded activation energies of 70 meV and 10 meV for the carriers in 5% at. Sn and 16% at. Sn samples, respectively. The decrease in activation energy as the Sn content increases agrees with the trends shown in Figures 3.3 and in Figure 3.4 a,b, in which a higher conductivity is observed for the samples having higher Sn concentration, consistent with a reduced activation energy required for thermal excitation of carriers into the conduction band. Hall measurements were not able to identify the carrier type in the films due to low mobilities ( $< 10 \text{ cm}^2 \text{ V}^{-1} \text{ s}^{-1}$ ). However, the hot probe technique performed on samples indicated n-type majority carriers.

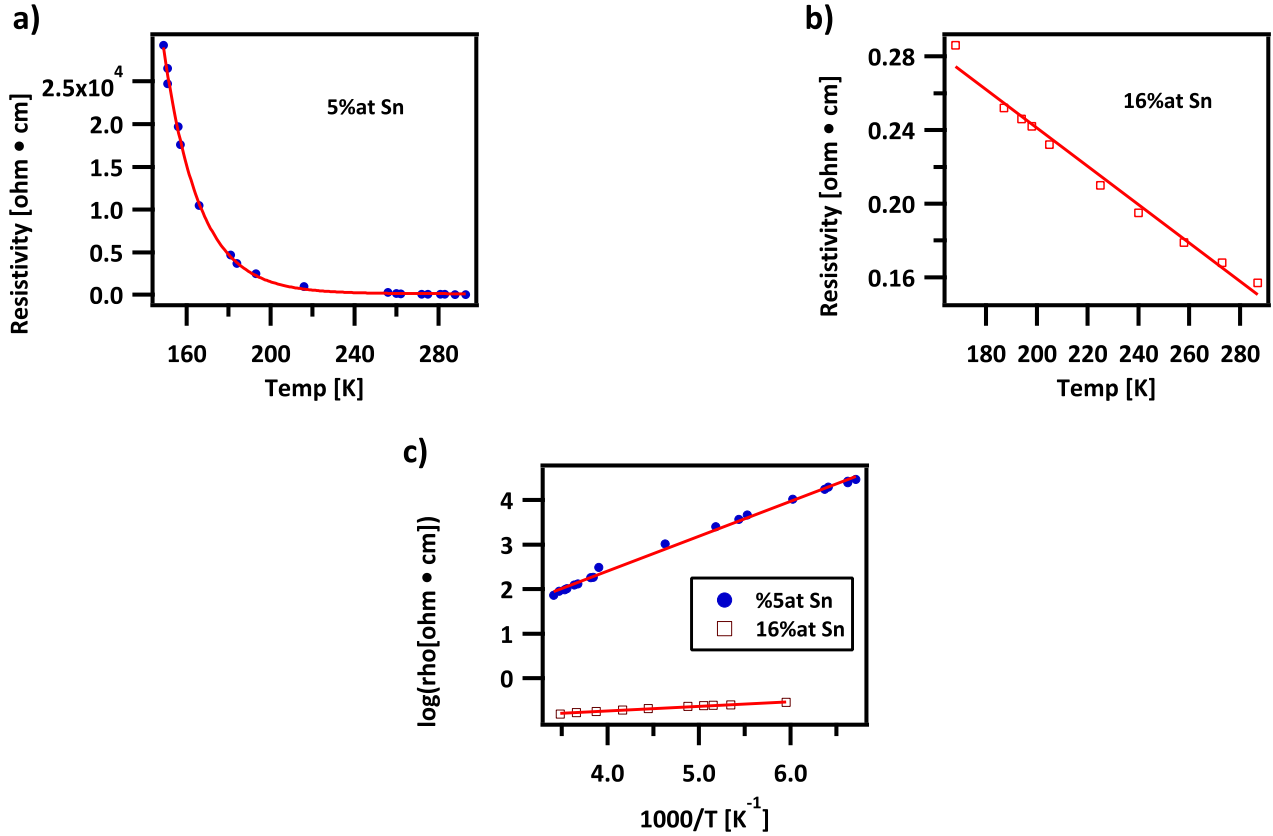


Figure 3.4: Resistivity vs. temperature for samples with a) 5% atomic concentration of Sn and b) 16% atomic concentration of Sn. The samples exhibit behavior characteristic of semiconductors, with increasing resistivity over decreasing temperature. The change in resistivity over decreasing temperature indicate 16%atSn samples acting degenerately and 5%at Sn samples acting non-degenerately. c) Arrhenius plot (log of resistivity versus inverse temperature) for 5%at and 16%at samples. The greater slope of the 5%at Sn trend line indicates a greater activation energy for thermalized carriers.

### 3.3 Raman shifts for ZnSn<sub>x</sub>Ge<sub>1-x</sub>N<sub>2</sub> alloys

Raman spectroscopy was performed with a Renishaw inVia Raman microprobe equipped with a Leica DM 2500M microscope, a Leica N Plan 50× objective, a 1800 lines/mm grating, and a CCD detector configured in a 180° backscatter geometry. A 532 nm diode-pumped solid-state laser (Renishaw model RL532C50) was used as the excitation source and delivered a < 50  $\mu$ W radiant flux at the surface of the sample. Light was circularly polarized before exposed to the substrate, and the collected signal was

not polarized.

Figure 3.5 plots the Raman shifts for  $\text{ZnSnN}_2$  and low-tin  $\text{ZnSn}_x\text{Ge}_{1-x}\text{N}_2$ . Spectra for  $\text{ZnSnN}_2$  were distinguishable from the quaternary  $\text{ZnSn}_x\text{Ge}_{1-x}\text{N}_2$  spectra in peak shape and positioning.  $\text{ZnSnN}_2$  shifts had five main features that with Peak 1 approximately at  $677\text{ cm}^{-1}$ , Peak 2 at  $576\text{ cm}^{-1}$ , Peak 3 at  $450\text{ cm}^{-1}$ , Peak 4 at  $235\text{ cm}^{-1}$ , and Peak 5 at  $120\text{ cm}^{-1}$ .

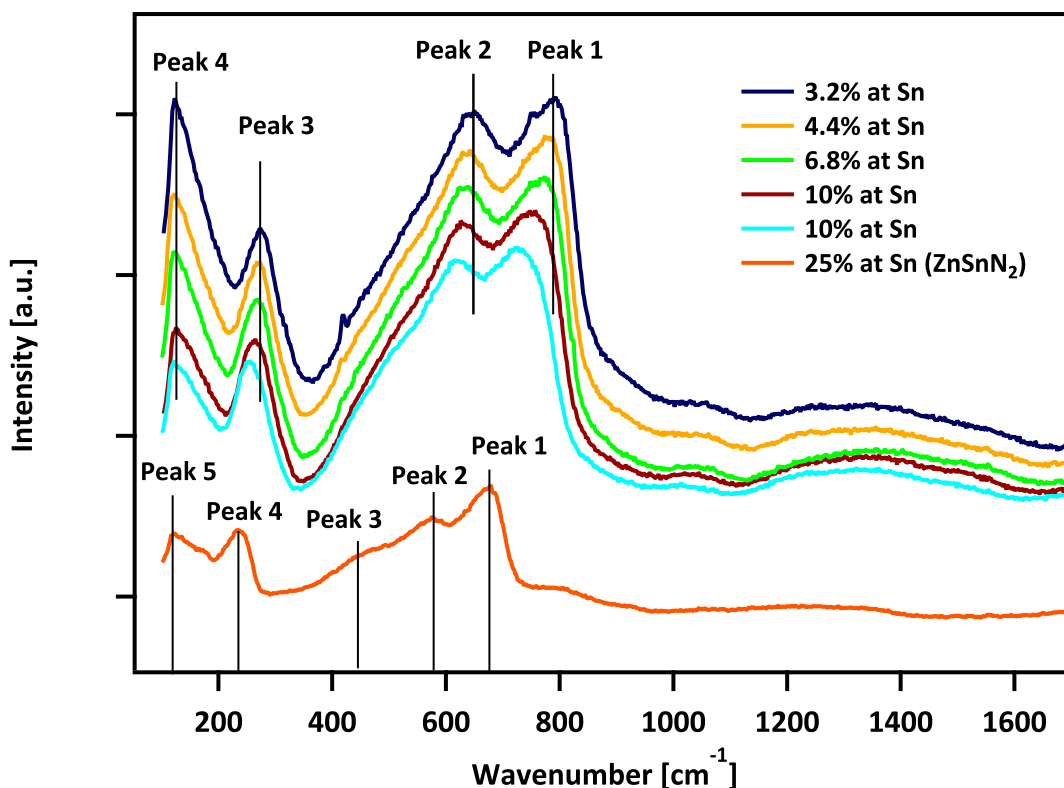


Figure 3.5: Raman spectra for  $\text{ZnSnN}_2$  and several low-tin  $\text{ZnSn}_x\text{Ge}_{1-x}\text{N}_2$  alloys. Peak 5 from  $\text{ZnSnN}_2$  and Peak 4 from the  $\text{ZnSn}_x\text{Ge}_{1-x}\text{N}_2$  alloys may be artifacts from the detector limits. Existence of broad peaks represent disorder from either random cation positioning or random stacking of pseudospin layers.

Raman shifts for the quaternary alloys consisted of four major peaks spanning broadly from the minimum detectable wavenumber to  $1000\text{ cm}^{-1}$ . Peak 1 appears at a range around  $750\text{--}800\text{ cm}^{-1}$ , Peak 2 at  $620\text{--}650\text{ cm}^{-1}$  with a slight shoulder analogous to  $\text{ZnSnN}_2$ 's Peak 3, Peak 3 at  $250\text{--}275\text{ cm}^{-1}$ , and Peak 4 at  $120\text{ cm}^{-1}$ . No high intensity peaks were observed above  $1000\text{ cm}^{-1}$ , although some features in the background may

be relevant. Plotting peak position to Sn content (Figure 3.6), Peak 1 and Peak 2 look to change directly with Sn content, while Peak 3 and Peak 4 do not appear to correlate as linearly. Peak 4 may be convoluted with the detector range and may be an artifact.

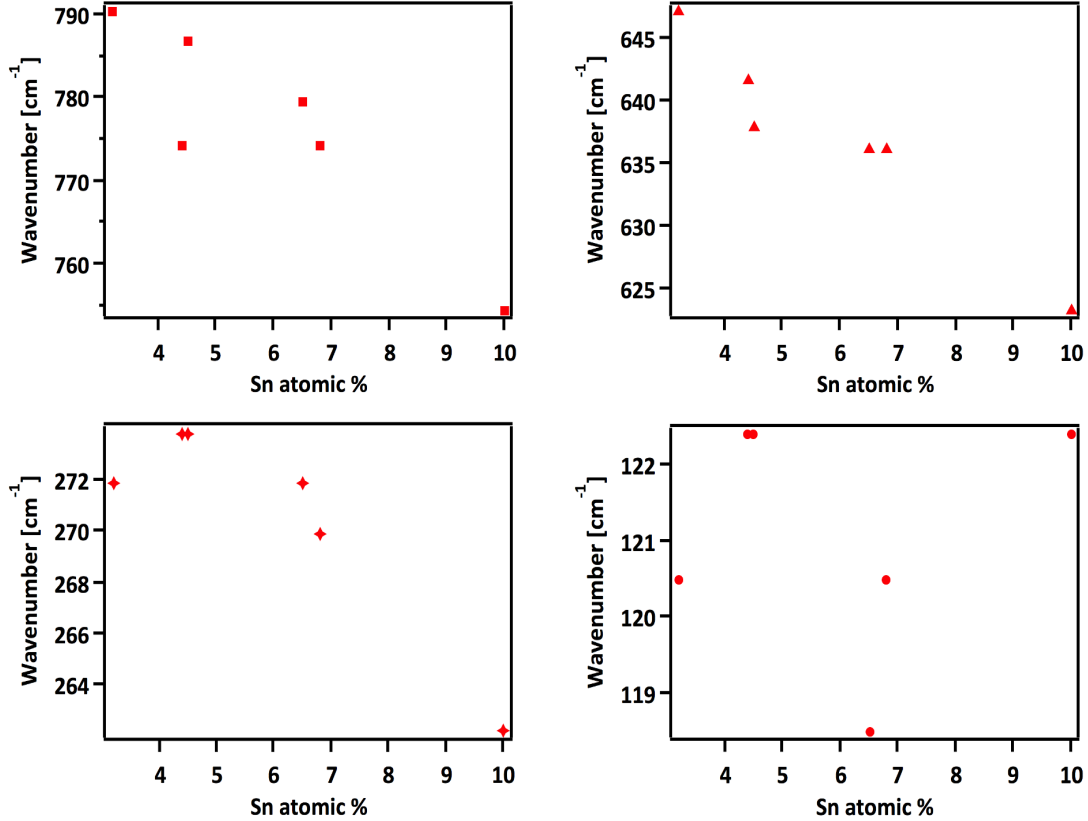


Figure 3.6: Raman shift vs Sn content for quaternary  $\text{ZnSn}_x\text{Ge}_{1-x}\text{N}_2$  alloys. Peak 1 and Peak 2 show correlation with % atomic Sn, while the relationship is less clear for Peak 3 and Peak 4.

Calculations and experimental results for Raman shifts and phonon density of states have been performed [35, 36, 37] for the ternary alloys  $\text{ZnSnN}_2$  and  $\text{ZnGeN}_2$ . These give insight to both ternary  $\text{ZnSnN}_2$  and quaternary  $\text{ZnSn}_x\text{Ge}_{1-x}\text{N}_2$  spectra collected. The collected spectra of the sputtered  $\text{ZnSnN}_2$  films match those in the literature [35], having the same general peak positions and broad shapes. These have been identified to represent the average density of states than specific modes at select crystal orientations. The broadness of peaks is due to either disorder in the

lattice from polycrystalline defects, random stacking fault defects, or random cation position anti-site defects [36]. Exact transitions cannot be identified in terms of their symmetry because transitions are calculated specifically to a crystal k-wavevector. Thus, for the defective sputtered materials, k-wavevectors are not well defined and Raman spectra observed for  $\text{ZnSnN}_2$  have been shown to reflect the calculated average phonon density of states over all k-wavevectors.

The Raman spectra for the  $\text{ZnSn}_x\text{Ge}_{1-x}\text{N}_2$  quaternary alloys also consist of broad peaks, which shift with Sn content. Previous Raman studies have only been performed on  $\text{ZnSnN}_2$  and  $\text{ZnGeN}_2$ , but provide boundaries for the quaternary alloy Raman shifts. The low-tin  $\text{ZnSn}_x\text{Ge}_{1-x}\text{N}_2$  alloys appear at lower wavenumbers than the peaks listed for  $\text{ZnGeN}_2$  by Viennois et al. [37], but at higher wavenumbers than the  $\text{ZnSnN}_2$  peaks. The broad peaks additionally have similar shape to those presented in Ref. [37] and for  $\text{ZnSnN}_2$ . Although the vibrations still cannot be discerned in the polycrystalline quaternary alloys, Peak 2 may incorporate the wurtzite- $E_2$  and  $A_1$  analogues for the II-IV-V system, where nitrogen atoms primarily vibrate and cations are relatively stationary [36].

Ultimately, the peak shifts in the Raman spectra are important because they display that in these Zn-IV-Nitride systems, the decrease in Sn content and increase in Ge content gradually translates the lattice phonon behavior. When Ge replaces Sn, tighter bonds are formed with the smaller Ge cation to N anions, leading to larger spring constants and more energetic vibrations. Therefore, Raman shifts increase in wavenumber. These Raman studies will also be important in comparing the films grown by sputter deposition and the films grown by Molecular Beam Epitaxy, described in Chapter 5.

### 3.4 $\text{ZnSn}_x\text{Ge}_{1-x}\text{N}_2$ solid-state devices

Metal/Semiconductor devices from quaternary alloys with  $> 10\%$  Sn displayed ohmic characteristics for a variety of work function metals including gold, platinum, nickel, indium, zinc, tin, silver, aluminum, and magnesium. Although contacts were not

capped, thus metal oxides likely formed, deposited metal layers were several hundred nanometers thick such that the junction may still be a metal-semiconductor interface. Ohmicity was potentially a result of the combination of the degeneracy of the  $>10\%$  Sn-composed  $\text{ZnSn}_x\text{Ge}_{1-x}\text{N}_2$  active material and surface states.

In contrast, low-tin Schottky devices with gold, platinum, and tungsten investigated have led to IV characteristics different from previous ohmic devices, shown in Figure 3.7 by an asymmetric IV curve. The asymmetry results from some carrier transport blocking, possibly due to rectification and band bending within the low-tin alloy. However, results do not show full rectification as expected for an ideal diode. Surface states may be interfering with any depletion width formation at the metal-semiconductor interface, reducing band bending and diminishing diode behavior. Chemical HF and HCl etch treatments attempted to passivate surface states before metal deposition did not improve device characteristics.

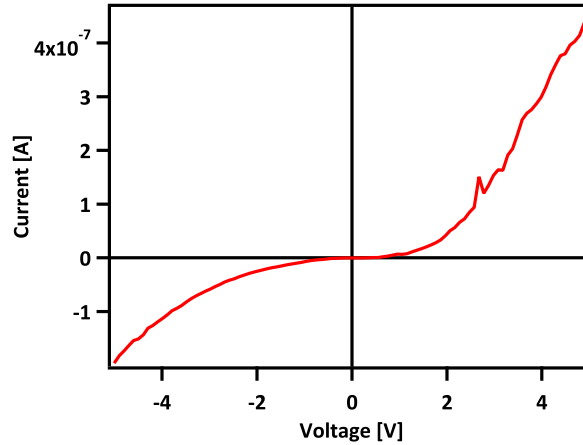


Figure 3.7: An asymmetric IV curve from a tungsten/low-tin alloy Schottky device resulting from some carrier transport blocking.

Further investigations in low-tin devices were tried, but met with problematic low-tin  $\text{ZnSn}_x\text{Ge}_{1-x}\text{N}_2$  synthesis. Charging seen in SEM analysis and XPS analysis indicated the films were more insulating compared to previous films of similar compositions. In probing these insulating low-tin films, the main outlying element lay in the x-ray diffraction, which showed the films were amorphous instead of crystalline and (002) oriented as before.

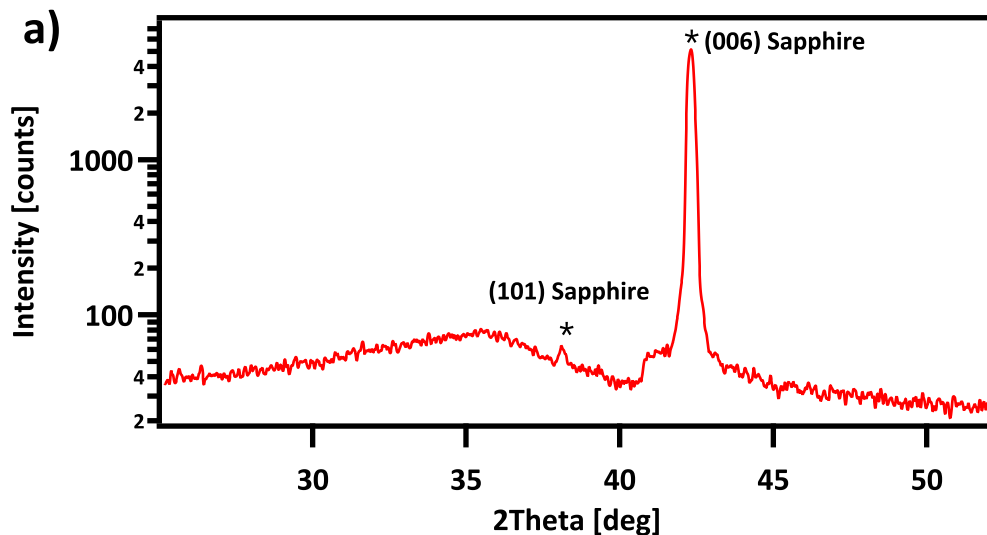


Figure 3.8: Amorphous growth of a low-tin  $\text{ZnSn}_x\text{Ge}_{1-x}\text{N}_2$

Control over crystallinity and solving the cause of this amorphous growth would allow better studies for low-tin alloy sputtered devices. The crystalline  $\text{ZnSn}_x\text{Ge}_{1-x}\text{N}_2$  ( $x < 1$ ) films, similar to  $\text{ZnSnN}_2$ , also grow oriented on various substrates (Fig. 2.3). Additionally, films deposited on conductive metal and degenerate silicon substrates had less tendency to charge from electron emission than films on insulating substrates. The sputtered columnar grain structures could play a role in improved carrier transport from the substrate, and experiments for thru-film conduction for the low-tin alloys would verify if the grain structure influences anisotropic carrier mobility.

Understanding the carrier conduction in amorphous films compared to oriented crystalline films would offer insight on crystal structure and band energetics and filling. Density functional theory simulations may aid in explaining the coupling of these phenomena. Finally, after achieving better handle on deposition, future avenues to study that may enable fully rectifying devices would include Metal-Insulator-Semiconductor (MIS) structures and/or other wet or dry surface treatments to passivate surface states. Semiconductor electrochemistry may also be a technique that can circumvent some surface state effects. Evidence of surface states in the electronic structure of  $\text{ZnSnN}_2$  and  $\text{ZnSn}_x\text{Ge}_{1-x}\text{N}_2$  alloys is elaborated in the next chapter.

## Chapter 4

# Electronic properties by photoelectron spectroscopy

This chapter reviews method and results for determining the work functions of  $\text{ZnSnN}_2$  and  $\text{ZnSn}_x\text{Ge}_{1-x}\text{N}_2$  alloys by photoelectron spectroscopy. Photoelectron spectroscopy probes the electronic structure and bonding of a material's surface. The technique uses the principles of the photoelectric effect to examine the filled electron states in a solid. A specimen is irradiated with  $h\nu$  and if the electrons in the solid are excited above the minimum required energy, the electrons are ejected from the material's surface. Since each electron in its atomic orbital has a specific quantized energy due to its orbital and atom type, characteristics like elemental composition and chemical oxidation state can be extracted from photoelectron spectra. X-ray photoelectron spectroscopy (XPS), employing monochromatic Al  $K\alpha$  x-rays at 1486 eV, can penetrate approximately the first  $\sim 10$  nanometers of a material's surface [38]. Ultra-violet photoelectron (UPS) spectroscopy, using a He I excitation energy at 21.21 eV, can penetrate  $\sim 1$ -2nm of a surface [39]. Additionally, both XPS and UPS can be used to determine the surface work function.

The work function is a critical property for designing and incorporating a material into optoelectronic devices. The work function of a material's surface allows one to view the relative energetic alignment of its Fermi level and electronic bands compared to the electrochemical potentials of other materials or redox couples. Furthermore, the work function assists in predicting the electronic behavior—electrochemical potential

equilibration and band bending—at a material’s interface by the Anderson technique for semiconductor-semiconductor interfaces or the Schottky-Mott technique for metal-semiconductor interfaces, and redox couple-semiconductor interfaces [40, 41]. Work function values provide information for appropriate band alignment to construct homojunctions, heterojunctions, or water splitting electrochemical potential positioning for the hydrogen evolution reaction or the oxygen evolution reaction [41, 42, 43]. These alignments, combined with band gaps, carrier densities, and other material descriptors, are used to theorize if materials will form Type I, Type II, or Type III junctions and estimate junction carrier dynamics. Fermi level and band gap alignments may also indicate electron and hole transfer possibilities with redox couples in solution and if materials are appropriate for semiconductor photoelectrochemistry [43, 44, 45].

Work function can be measured by using photoelectron spectroscopy (PES) or Kelvin Probe Force Microscopy (KPFM). Through PES, the work function of a material can be determined from the photoelectric effect. An x-ray or UV source excites electrons in the material, and the spectrometer detects the electrons ejected from the material. The work function is determined from the threshold energy, where electrons are barely emitted from the material, and the initial excitation energy [46]. Conversely, Kelvin Probe Force Microscopy (KPFM) measures a contact potential difference (CPD) between the probe tip and the material surface. The material work function may be calculated relative to the work function of the probe tip. Both techniques require a clean surface to accurately determine the material’s work function, as any contamination, oxidation, or adsorbed molecules will affect the surface electrochemical potential [47, 48, 49]. Thus, experiments performed in UHV are preferred, in addition to sample preparation that minimizes surface contamination. In-situ cleaning, such as sputter ablation or annealing, can remove contaminants. Crystal cleavage in UHV or material fabrication in a cluster tool attached to the analysis instrument are also options for creating clean surfaces, although cluster tools are costly and scarce, and thus analyzing thin-film samples is challenging. Furthermore, work function changes with crystal orientation, and thus values for inhomogeneous,

polycrystalline, or defective surfaces may vary [50].

In Section 4.1, the work function and electronic structure of thin-film  $\text{ZnSnN}_2$  by PES in UHV is determined using both UV and x-ray excitation energies. Vacuum-transferred samples are compared to samples after changes in surface contamination from air-exposure, in-situ plasma-treatment, and argon ion sputtering. From combining the work function, the valence band maximum (VBM), and the band gap, a band diagram for  $\text{ZnSnN}_2$  and its interface to vacuum is created. In Section 4.2, work function and electronic trends for the  $\text{ZnSn}_x\text{Ge}_{1-x}\text{N}_2$  alloys are discussed.

Thin-film samples were fabricated by reactive RF sputtering from separate Zn, Sn, and Ge targets. Each target was 99.99+% pure, and the targets were held at discrete RF powers during sputtering. Before deposition, epitaxial-ready c-plane sapphire and GaN template substrates were prepared with an isopropanol rinse, then dried with a stream of nitrogen gas, and heated to 175 °C in the vacuum sputter chamber at a base pressure of 5E-8 Torr. Polished degenerate (111) n-Si substrates were etched with HF to remove surface oxide, dried with a stream of nitrogen gas, and heated to 175 °C before deposition. During sputtering, the plasma in the chamber was maintained by a 1:3 argon:nitrogen gas-flow ratio at 3 mTorr pressure. All samples were sputtered to thicknesses between 300-900 nm. Samples were transferred from the sputtering chamber to a Kratos Axis Ultra spectrometer using a vacuum suitcase ( $< 3\text{E-}7$  Torr). Nitrogen plasma treatment, argon-ion sputter etch, and vacuum annealing were also performed in the Kratos spectrometer. Photoelectron spectroscopy was performed with an analysis chamber base pressure  $< 3\text{E-}9$  Torr and Al  $K\alpha$  x-rays ( $h\nu = 1486.7$  eV). UPS was performed with He I excitation from a UV lamp mounted on the analysis chamber and directed at the sample. A strong peach-color light was attained for He I energy ( $h\nu = 21.21$  eV). Spectra of the valence band region to secondary electron cut-off region were acquired at 25 meV step-size and 5eV pass energy. XPS secondary electron cut-off regions were acquired at 25 meV step-size and 5 eV pass energy with the x-ray gun held at 0mA and 15keV to not overload the analyzer. Work functions (WF) were calculated by taking the secondary electron cut-off energies (SEC) and subtracting them from the excitation energies ( $h\nu$ ) (Equation 4.1). SECs

shift accordingly with applied external bias, indicating SECs were of the sample and not artifacts.

$$\text{WF} = h\nu - \text{SEC} \text{ (Equation 4.1)}$$

XPS survey scans were taken with a 1eV step-size, 100 ms collection time, 40 eV pass energy, and ‘slot’ aperture. High resolution scans of the valence band region and carbon, oxygen, zinc, tin, and nitrogen peaks were acquired at 25meV step-size, 10eV pass energy, and ‘slot’ aperture. Peaks were analyzed with Casa XPS software using Gaussian-Lorentzian shapes and Shirley baselines. Stoichiometries were calculated with Zn 2p, Sn 3d, N 2s, C 1s, and O 2s peaks. After PES analysis, samples were removed from vacuum and measured with x-ray diffraction (XRD). Patterns from the samples were collected and analyzed using a high-resolution X-ray diffractometer employing Cu K $\alpha$  radiation ( $\lambda = 1.5418 \text{ \AA}$ ). The stoichiometry of the samples was measured using a scanning-electron microscope (SEM) equipped with an energy-dispersive spectrometer (EDS). The dielectric functions were determined by spectroscopic ellipsometry, with the data modeled using a wavelength-by-wavelength layer on top of a substrate layer. Hall measurements were performed to obtain carrier concentrations.

## 4.1 ZnSnN<sub>2</sub> work function measurements

Figure 4.1 displays the UPS work function values (left axis) of vacuum-transferred ZnSnN<sub>2</sub> samples. Each sample was measured at several locations on the sample surface, displaying consistent values within 2 meV standard deviation, shown by the red error bars. Across samples, work function values are also consistent, ranging within 0.3 eV and averaging at  $4.04 \pm 0.09 \text{ eV}$ . Sample 9 had the lowest measurement at 3.85 eV, and was the only sample without preferential crystalline orientation toward the (002) ZnSnN<sub>2</sub> direction, which may be cause to its low result. The right axis displays % C and O surface concentrations obtained from high resolution XPS scans of the C 1s and O 1s regions performed after UPS. Average surface contamination is 3% C and 4% O. Adventitious carbon and oxygen may affect UPS measurements, as it is a

surface sensitive technique. However, the work functions of these nearly clean vacuum-transferred samples do not correlate with the % C or % O, indicating the C and O on the surface are minor, predicted less than a monolayer, and the majority of exposed surface is  $\text{ZnSnN}_2$ , with 50% N, 23% Zn, 20% Sn atomic concentration determined by XPS. Furthermore, work functions from x-ray excitation, which penetrate the surface deeper than UV excitation, were also determined and confirmed the UV excitation derived values (Figure 4.2, Table 4.1).

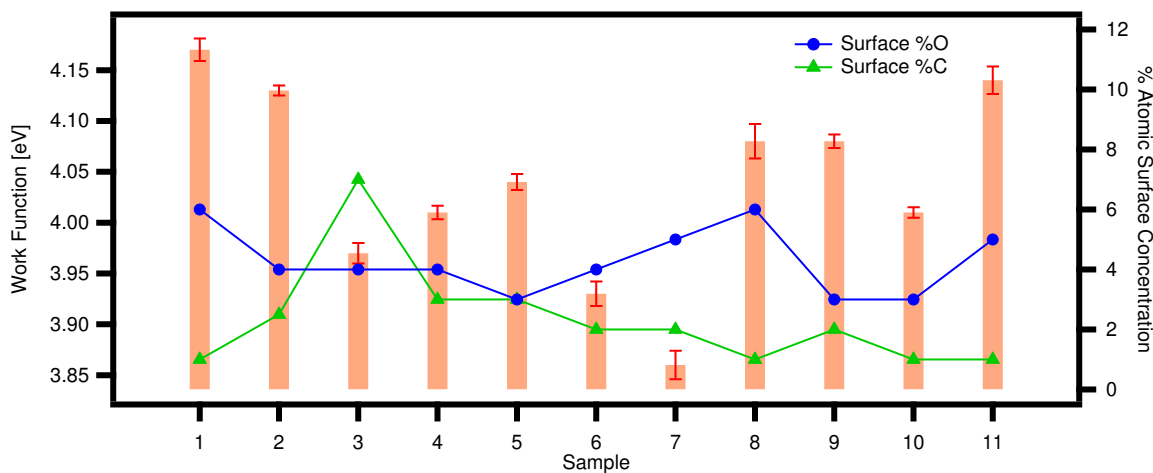


Figure 4.1: UPS work function (bars) of vacuum-transferred  $\text{ZnSnN}_2$  samples with standard deviations (red). Overlaid are the surface concentrations of C (green triangle) and O (blue dot).

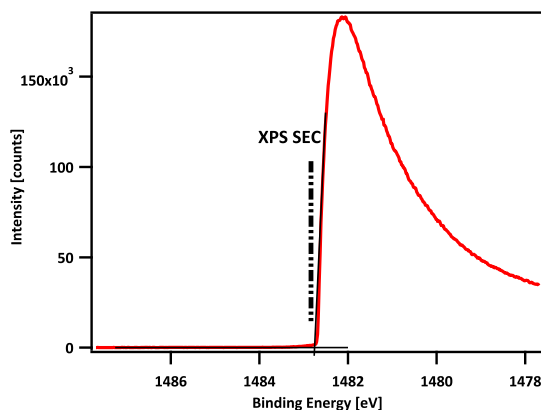


Figure 4.2: XPS SECs used to determine work function and verify UPS values.

Further investigation to clarify the influence of surface contamination on work function value was performed, ensuring that a  $\text{ZnSnN}_2$ -oxide was not the primary

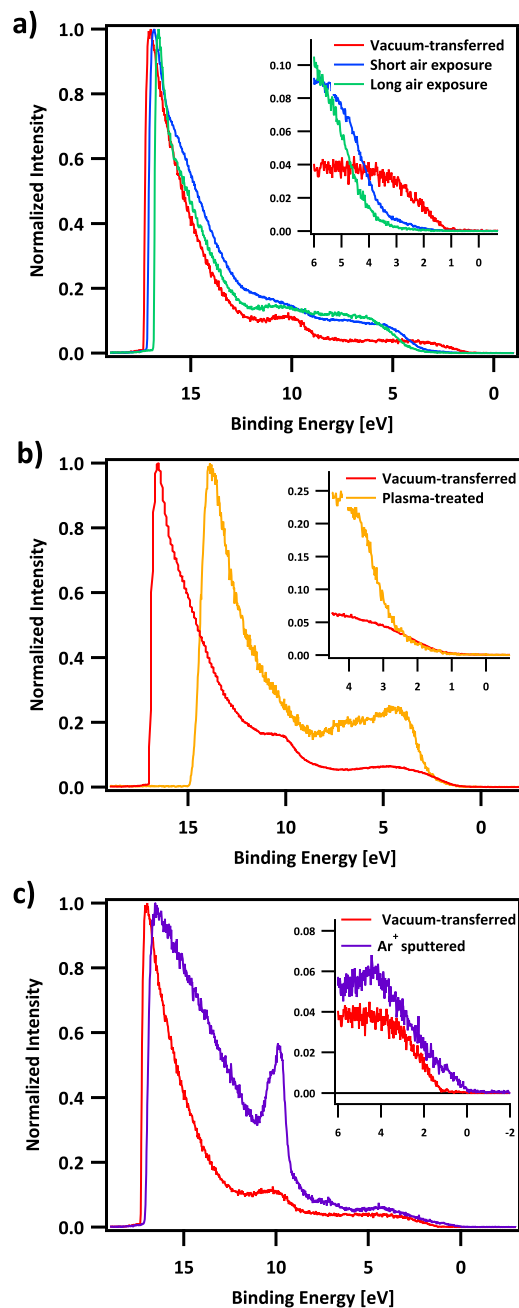


Figure 4.3: Comparison of UPS spectra for vacuum-transferred  $\text{ZnSnN}_2$  samples with spectra obtained for  $\text{ZnSnN}_2$  samples after a) air exposure, b) nitrogen plasma treatment, and c) argon-ion sputter treatment. Short air exposure was for  $< 10$  seconds in atmosphere, and long air exposure was for  $< 1$  minute. The spectra were obtained using a He I source ( $h\nu = 21.21$  eV).

examined material. Work function measurements were taken after a period in vacuum, air exposure, and in-situ cleaning techniques to determine affects of surface carbon

and oxygen. Figure 4.3 shows the comparison of UPS spectra to vacuum-transferred samples. The sharp intensity at  $\sim 17$  eV binding energy is the secondary electron cutoff (SEC), the fine structure at 10.1 eV represents the Zn 3d states [51], and the increase in counts at  $\sim 1.2 - 3$  eV is the valence band onset. For the vacuum-transferred spectrum, the prominence of the Zn 3d feature in the UPS signifies the cleanliness of the surface. The reduced fine structure in the air exposed spectra (Fig. 4.3a) indicate the presence of contamination overlayers, while the shift in the SEC and VB onset represent a change in work function and valence band position. Figure 4.3a displays the valence band maxima (VBM) increase in binding energy after repeated air exposure. This agrees with surface oxidation of the nitride, since the N 2p contribution to the valence band states penetrates more into the band gap than O 2s contribution [52, 53]. Figure 4.3a shows the greater oxidation moving the valence band onset to higher binding energy, indicative of more O 2s character at the film's top  $\sim 1$  nm surface. The shift of the SEC to lower binding energy after air exposure represents an increasing work function. Figure 4.4 shows the work function progression and C and O coverage of a sample with successive air exposures. This increasing trend correlates with the surface oxygen concentration, and agrees with greater percentages of Zn-O and Sn-O present. ZnO has a work function range of 4.3 - 5 eV [54, 55] and SnO<sub>2</sub> has a work function range of 4.7 - 5.7 eV [56, 57], depending on surface preparation. Thus, the average work function after each air exposure is higher from more metal oxide incorporation in the measured area. This agreement is shown over several samples in Figure 4.4, where work functions of freshly vacuum-transferred samples are compared to their values after air exposure. The coverage of % O and % C increase  $> 20\%$ , and work functions rise to a new average of  $4.3 \pm 0.2$  eV. Therefore, the lower work function values of freshly vacuum-transferred samples best represent that of the ZnSnN<sub>2</sub> surface.

Attempts to eliminate surface contamination with in-situ cleaning techniques of nitrogen plasma cleaning and argon ion sputter cleaning were also performed. Instead they caused evident chemical changes to the surface, seen in UPS and XPS spectra (Figure 4.3b and 4.3c, Figure 4.6), and signify that the work functions of freshly

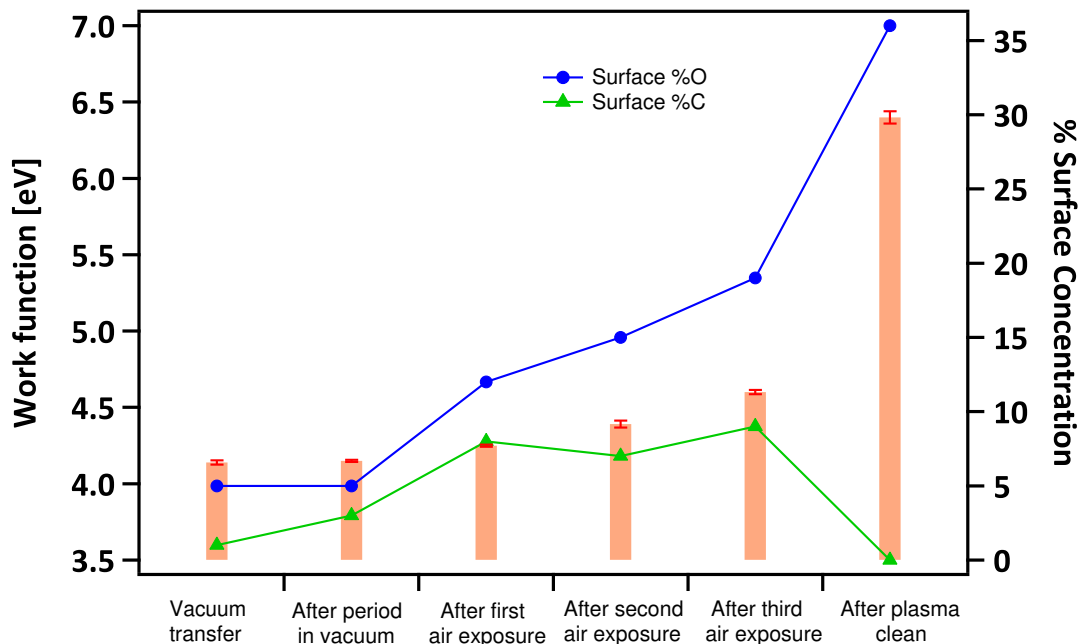


Figure 4.4:  $\text{ZnSnN}_2$  work function measurements of one sample after progressive air exposures and accumulated adventitious carbon and oxygen. Work functions increase with the oxygen surface concentration. For the plasma-treated film, chemical bonding with oxygen

vacuum-transferred samples represent the most appropriate  $\text{ZnSnN}_2$  work function values. The in-situ plasma treated samples were cleaned in the photoelectron spectrometer's load-lock chamber. Due to residual oxygen in the load-lock, oxygen could not be eliminated from the  $\text{ZnSnN}_2$  surface. The stoichiometry of the plasma-treated surface comprised of 36% O. Figure 4.3b displays the UPS spectra of the treated surface compared to its vacuum-transferred surface. The SEC shifts to lower binding energy as with oxidized surfaces from air exposure, but unlike air-exposed samples, plasma treatment raises the work function above 6 eV. The Zn 3d fine structure also vanishes, and valence band onset slightly increases.

The XPS spectra (Figure 4.6) display chemical changes from oxidation, where the N 2s region obtains a peak at 402.2 eV, and the Zn 2p and Sn 3d peaks shift in binding energies. Surfaces after air exposure do not acquire a peak at 402.2 eV, characteristic of nitrogen donating electrons to oxygen [58]. The formation of this N-O peak is

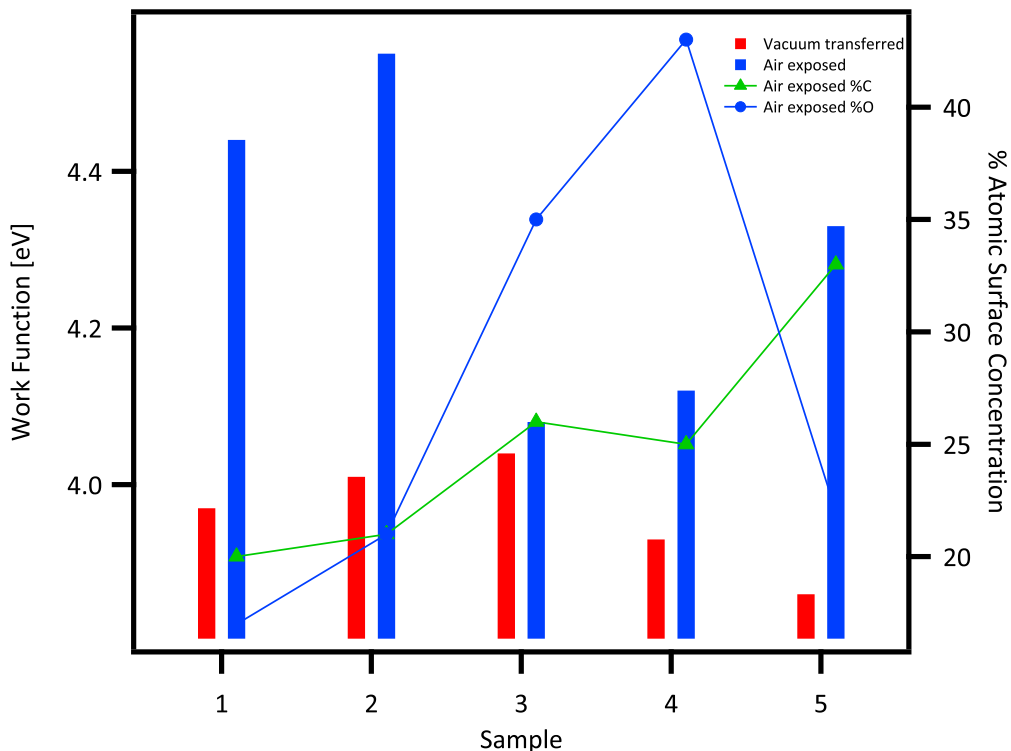


Figure 4.5: Work function of various  $\text{ZnSnN}_2$  samples before and after air exposure. Across several sample, air exposed work functions have greater values than vacuum transferred values.

likely caused by the high-energy plasma. Argon-ion sputter treatment was employed at the instrument's lowest energy (500 eV). However, this procedure also reacted the nitrogen with the surface oxygen, seen in Figure 4.6, where a peak appears at 404.5 eV, indicative of N=O bonding [59]. Additionally, sputtering effects result in reduced nitrogen peak integration from nitrogen loss. The argon ions preferentially ejected the lighter nitrogen atoms from the surface, lowering the %N, leaving the surface with a more metallic characteristic. Figure 4.6 displays the XPS N 1s peak, the Sn 3d peaks, Zn 2p peaks, and the valence band onset after longer than 1 minute sputter. Nitrogen loss is apparent in the Sn 3d doublet, where each peak decomposes into multiple oxidation states, with increasing preference toward neutral tin, indicating the change in bonding occurring between the tin cations and nitrogen anions. Slight shifts are also seen in the Zn 2p peaks toward higher binding energies, potentially from greater oxide formation. Finally, the valence band onset at 0 eV after a 1 minute

sputter shows that the sample has become more metallic in nature (Fig. 4.3c), with a continuous electron population to the Fermi level at 0 eV.

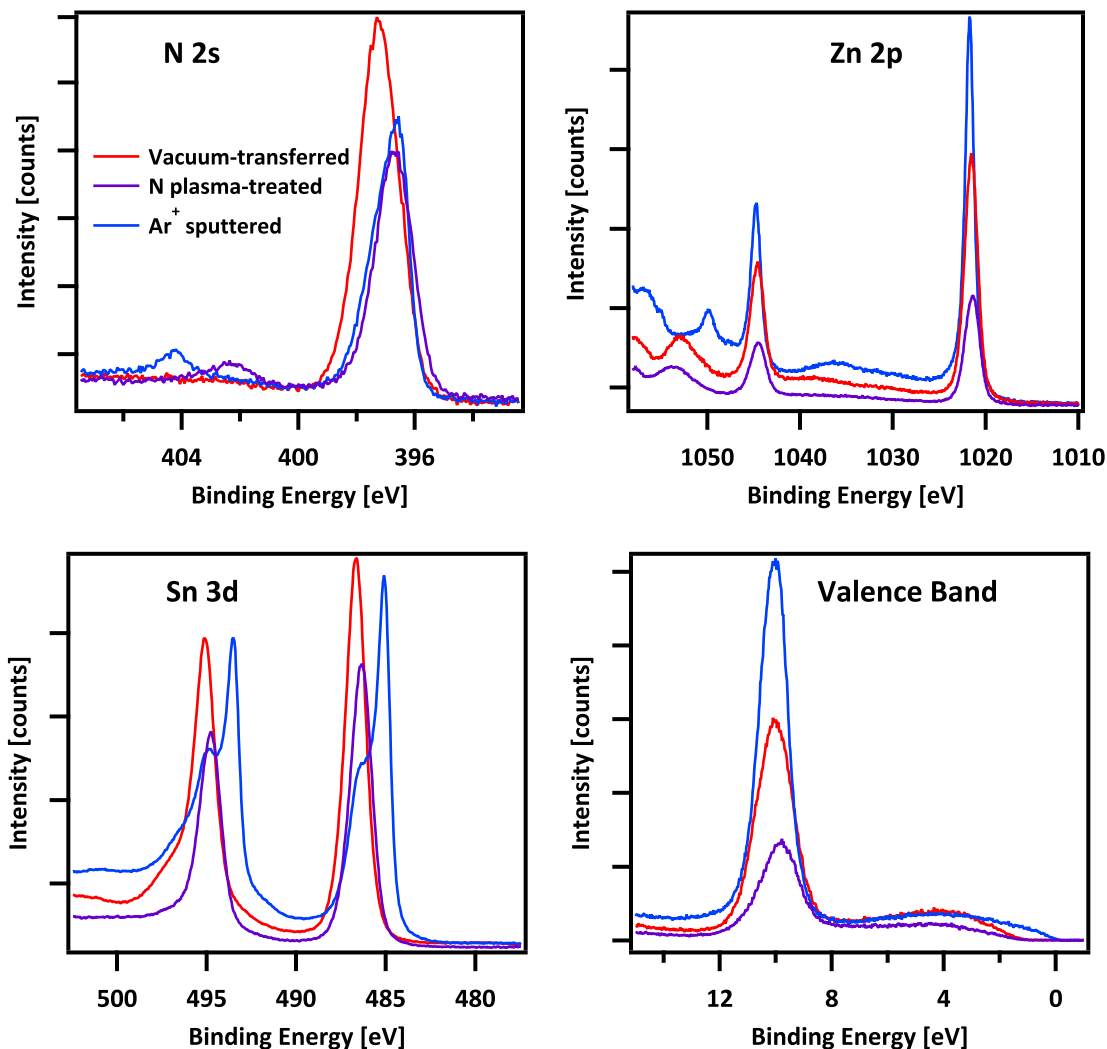


Figure 4.6: High resolution XPS regions of N 1s, Zn 2p, Sn 3d, and valence band regions for freshly vacuum-transferred samples and  $\text{Ar}^+$  sputter-treated samples.

Argon ion sputter cleaning performed for shorter times ( $< 10$  sec) have mitigated effects; however, changes in surface stoichiometry are still apparent and the surface is no longer of the fabricated  $\text{ZnSnN}_2$  quality. Work functions of argon ion sputtered surfaces vary over samples and sputtering time, but do not represent the  $\text{ZnSnN}_2$  work function.

For freshly vacuum-transferred samples, the valence band maximum is at  $\sim 1.2$  eV

from the Fermi energy at 0 eV binding energy. Combining this value with the measured band gap of  $\sim 1.8 - 2$  eV, this places the Fermi level in the gap approximately 70% from the valence band to the conduction band, indicating the majority carriers as electrons. This result agrees with the carrier type from Hall and hot probe measurements. However, Hall measurements show carrier densities on the order of  $10^{20}$   $\text{cm}^{-3}$ , implying the Fermi energy in the degenerate regime, closer to the conduction band if carriers were all n-type.

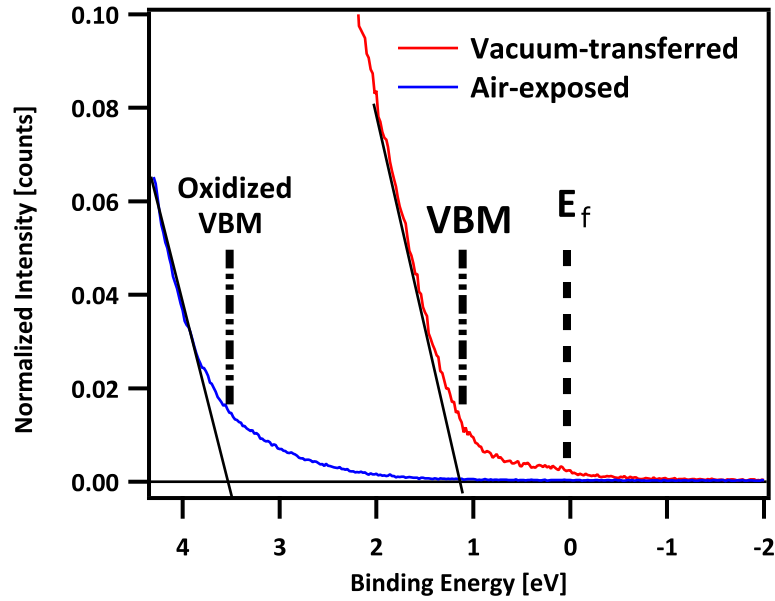


Figure 4.7: UPS spectrum of the  $\text{ZnSnN}_2$  valence-band region. Significant electron emission is seen between the VBM and the Fermi level, indicating occupied surface states in the gap region for vacuum-transferred samples. Air-exposed surfaces do not have such high electron counts, showing that oxygen passivates these gap states.

The discrepancy between the Fermi level position and the observed degeneracy is due to delocalized, mid-gap surface states. Looking at the UPS spectra of the valence band onset in Figure 4.7, electron counts exist from the valence band onset and past 0 eV binding energy. Metals show this trait in their valence band spectra at higher intensities, as their valence electron states are filled to the Fermi level [60]. However, the counts seen in this region for  $\text{ZnSnN}_2$  are from electrons in the band gap, signifying the existence of mid-gap states [61, 62, 63]. Figure 4.8 illustrates a band diagram of the Fermi level from a degenerate position that shifts toward mid-gap

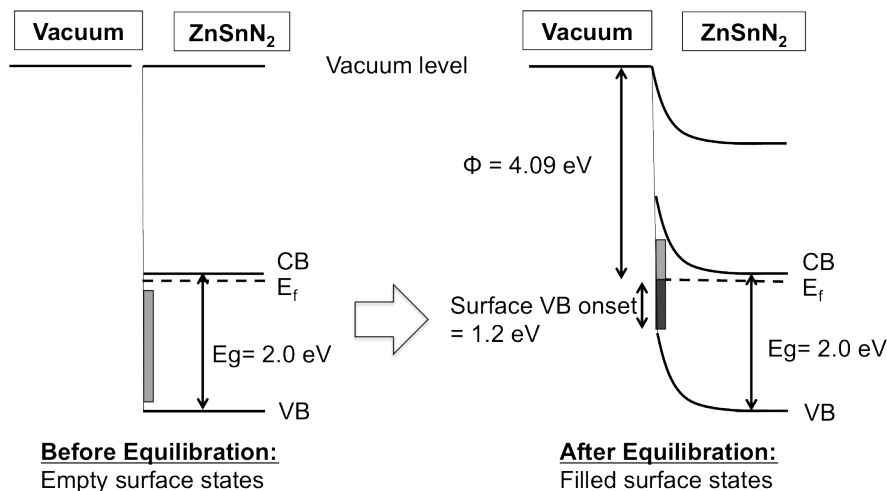


Figure 4.8: Energy-band diagram for the vacuum/ $\text{ZnSnN}_2$  interface prior to equilibration with mid-gap surface states (left) and after equilibration (right). Electrons from the bulk fill the empty surface states, causing the bands to bend upward, reducing the valence band onset at the surface from a degenerate position to 1.2 eV.

due to equilibration with surface states. The bulk material stays degenerate, with its Fermi level close to the conduction band, but equilibration with surface states causes the bands to bend such that the equilibrated Fermi position at the surface is closer to the center of the gap [50, 64, 65, 66]. Furthermore, oxygen passivates these surface states, as the electron count intensity reduces in the gap region after air exposure (Figure 4.7) [64, 65]. Figure 4.7 illustrates the effect of oxygen passivation and reduced band bending from less surface state interaction, where the distance between the Fermi level and the valence band onset widens. The density of surface states and band bending could be determined with the bulk density of states and carrier density because the thin-film  $\text{ZnSnN}_2$  bulk DOS has not been found. A rough approximation may be formed from the calculated theoretical DOS for single crystals [12, 13].

Although the density of surface states, their energies, and amount of  $\text{ZnSnN}_2$  band bending is unknown, Figure 4.9 displays the current  $\text{ZnSnN}_2$  work function measurement on the vacuum energy scale and Normal Hydrogen Electrode scale and against other common semiconductors and redox couples. The  $\text{ZnSnN}_2$  valence band at the surface would be 1.2 eV below the Fermi level; however, from band bending,

the bulk  $\text{ZnSnN}_2$  valence band is expected to be further below the Fermi energy. If the bulk Fermi level of the n-type  $\text{ZnSnN}_2$  is within the  $\text{ZnSnN}_2$  band gap, then Figure 4.9 depicts that  $\text{ZnSnN}_2$  might energetically work as a photocatalyst for the oxygen evolution reaction, whose redox energy is  $\sim 5.7$  eV below vacuum.

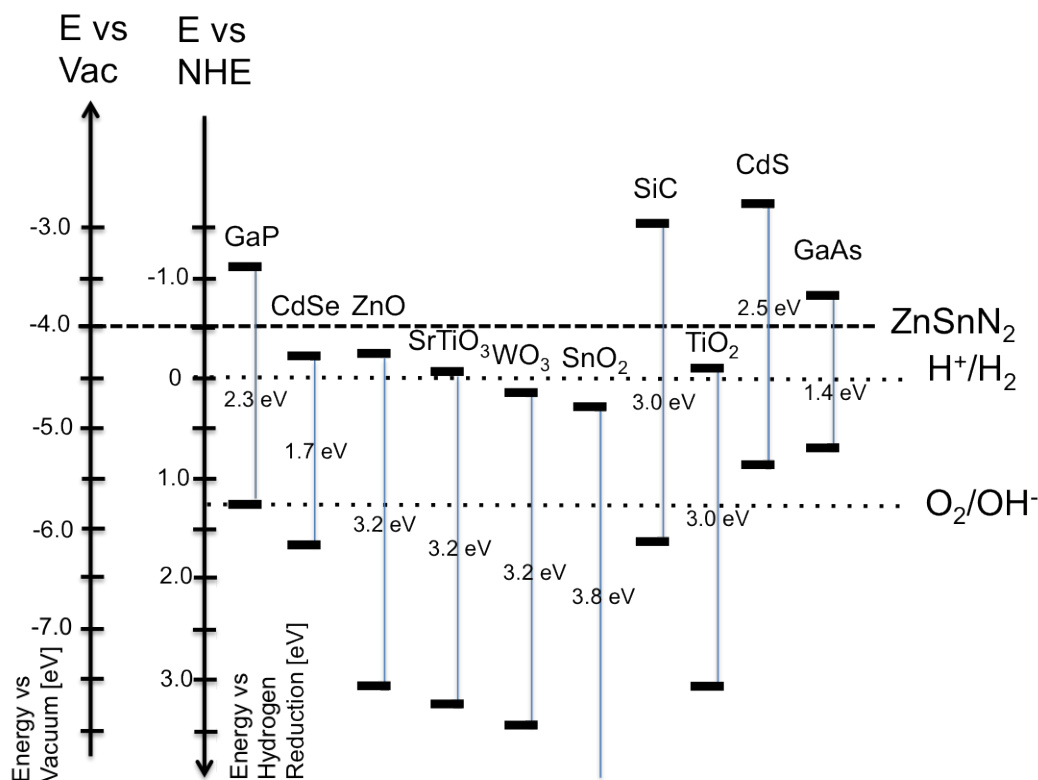


Figure 4.9:  $\text{ZnSnN}_2$  Fermi level alignment with various common semiconductors and redox couples on the vacuum energy scale and Normal Hydrogen Electrode scale. In vacuum, the  $\text{ZnSnN}_2$  valence band at the surface would be 1.2 eV below the Fermi level; however, the bulk  $\text{ZnSnN}_2$  valence band is expected to be further below the Fermi energy. Reference: Al-Hilli, 2009.

In summary, the UPS work function of reactive RF sputtered  $\text{ZnSnN}_2$  thin films has been measured to be  $4.04 \pm 0.09$  eV versus vacuum, with a VBM at  $1.22 \pm 0.09$  eV below the Fermi level, which agree with XPS derived measurements. Although minor surface contamination exists ( $< 4\%$  O, C), the freshly vacuum-transferred values most accurately represent the  $\text{ZnSnN}_2$  surface work function. More surface contamination yields higher work functions and increases the valence band onset with respect to the Fermi energy, characteristic of greater percentages of  $\text{SnO}_2$  and ZnO. In-situ cleaning

techniques create chemically altered surfaces, seen in XPS spectra by either loss of nitrogen or nitrogen-oxygen bonding, and shift UPS spectra SECs and valence band onsets. The work function and valence band onset, combined with band gap measurements, show the band positions for the ZnSnN<sub>2</sub> surface versus vacuum. Surface states cause band bending and put the ZnSnN<sub>2</sub> Fermi level towards mid-gap, instead of at its bulk degenerate position, typical of n-type semiconductor surfaces. This relative band alignment of ZnSnN<sub>2</sub> versus vacuum is valuable as it allows predictions for ZnSnN<sub>2</sub> interactions with electrochemical potentials of other semiconductors, metals, and redox couples. The ZnSnN<sub>2</sub> PES data additionally provides guidance for future surface preparation studies to create quality interfaces for devices.

	Work Function UPS [eV]	Work Function XPS [eV]	%O	%C	XPS VB onset* [eV]	UPS VB onset [eV]
Vacuum Transferred	4.04 ± 0.09	4.03 ± 0.09	4 ± 1	2 ± 1	1.20 ± 0.14	1.22 ± 0.09
Air Exposure	4.3 ± 0.2	4.0 ± 0.16	25 ± 10	27 ± 5	1.37 ± 0.09	3.44 ± 0.39
Plasma Cleaned	6.4 ± 0.04	-	36 ± 3	0	1.23 ± 0.08	2.43 ± 0.02**

Table 4.1: Average values for work function, valence band onset, and adventitious carbon and oxygen surface coverage. The error listed represents one standard deviation. \* Listed are VBMs determined by both XPS and UPS. XPS penetrates deeper into the material bulk and has less convolution with surface states and satellite peaks, so it is a more representative VBM value than that of UPS [A]. We reported the UPS value to demonstrate the surface affects from the different treatments, which are not as apparent in the XPS derived VB onset because the XPS signal averages photoelectrons from deeper into the bulk of the film. \*\*Although the linear extrapolation of the main body leads to this result, a significant tail of states into band gap exist.

	%N	%Zn	%Sn	%O	%C	UPS work function [eV]	UPS VB onset [eV]
Vacuum Transferred	51	22	20	3	2	4.08	1.22 ± 0.09
< 10 sec	46	25	22	4	3	4.15	0.58
~ 1 min	40	21	30	5	1	4.26	0

Figure 4.10: Composition, work function, and valence band onset values for argon-ion sputter-cleaned surfaces. Due to the decrease in nitrogen, other elements show increased contribution in the composition.

Average properties of the ZnSnN<sub>2</sub> samples are listed in Table 4.1. However, plotting the band gap, carrier concentration, and valence band onset against the work function for each sample shows there may be some dependence present (Figure 4.11).

Property	Average across samples
Band gap	$1.9 \pm 0.2$ eV
Carrier concentration	$3.6 \pm 3.2 \text{ E } 20 \text{ cm}^{-3}$
Mobility	$2.4 \pm 1.2 \text{ cm}^2\text{V}^{-1}\text{s}^{-1}$

Table 4.2: Average sample properties

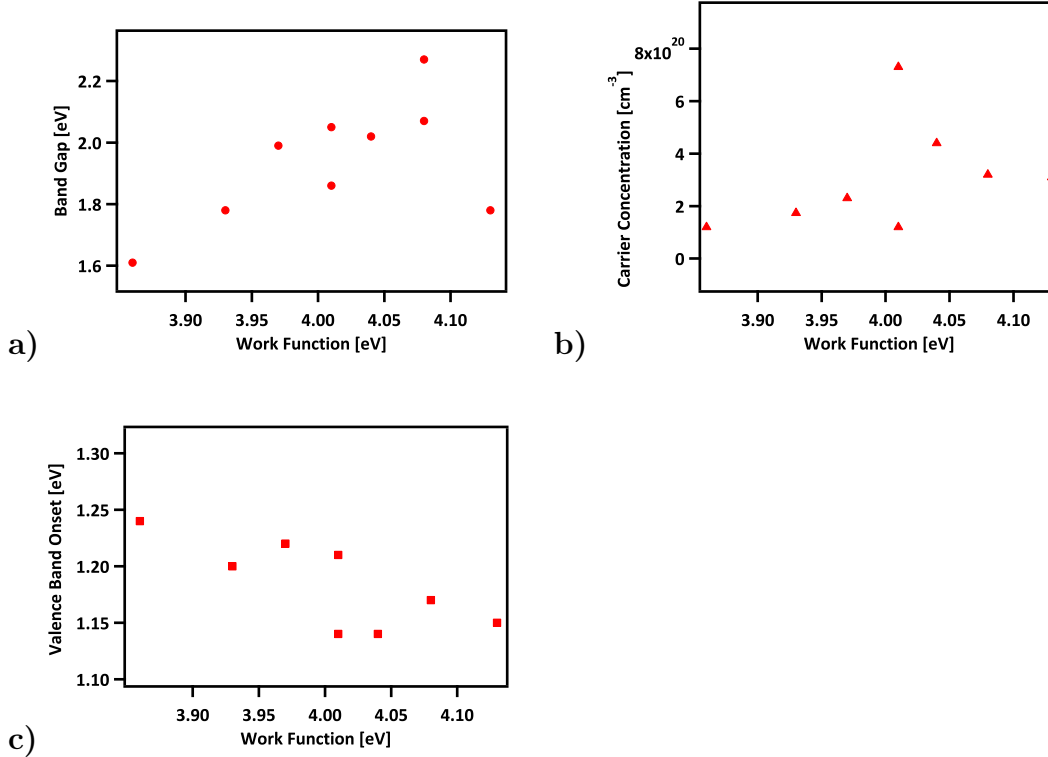


Figure 4.11: a) Band gap, b) carrier concentration, and c) valence band onset versus work function for individual samples.

## 4.2 $\text{ZnSn}_x\text{Ge}_{1-x}\text{N}_2$ work function measurements

Brief investigations were performed regarding the work functions of  $\text{ZnSn}_x\text{Ge}_{1-x}\text{N}_2$  surfaces by vacuum transfer. The three samples at approximately 7%-10% Sn concentration were tested. The work function values were close to  $\text{ZnSnN}_2$ , in the range of 4-4.2 eV, and valence band onsets similarly remained in a range between 1.2-1.5 eV. Surface states were also observed above the valence band onset in the UPS spectra. Although the data for the alloy series is limited, the similar values produced suggest Fermi level pinning of the alloy series. The concentration and energy of the surface states may be elucidated from a combination of high-resolution x-ray photoelectron

spectroscopy, Hall measurements, and optical absorption spectroscopy [67].

### 4.3 XPS band alignment measurements

As seen in previous sections, UPS is a technique that will give the work functions for pristine surfaces with respect to vacuum. However, band energetics may not follow the ideal Anderson model for interfaces because of impurities between the materials, atomic level imperfections in bonds, surface states, and more. Thus direct measurement of band alignment between materials may be preferred over calculated approximations from carrier equilibration. Kraut et al. developed a method for calculating the valence band offsets in heterostructures from XPS measurements of the valence and core level regions. Using this methodology, ZnSnN<sub>2</sub> band alignments to Au, Pt, and Mg were attempted.

ZnSnN<sub>2</sub> was prepared by sputter deposition with standard growth conditions. After cooling in situ, a thin metal overlayer was deposited on the ZnSnN<sub>2</sub> film. The sample was then transferred to the photoelectron spectrometer and scanned. This procedure was repeated with several different thicknesses of metal overlayers. The resulting slight peak shifts that were observed did not agree to give plausible band alignments to each metal. This may be due to oxidation of surfaces in the sputterer chamber or during transfer, or from degenerate material properties. Peak shifts would be expected from depletion width formation and band bending change within the semiconductor. The counts collected and averaged throughout XPS penetration depth determine the amount of band bending detected. The degenerate ZnSnN<sub>2</sub> may have too narrow of a depletion width compared to the overall penetration depth to cause any average band bending observations in the XPS data.

## Chapter 5

# Growth by molecular beam epitaxy

### 5.1 Motivation for MBE

Fabrication of reactive RF sputtered  $\text{ZnSn}_x\text{Ge}_{1-x}\text{N}_2$  ( $0 \leq x \leq 1$ ) films produced mostly nanocrystalline films with degenerate electronic properties, both which can contribute to low mobilities. Chapters 2 and 3 described experiments to increase mobilities and reduce degeneracy. Though annealing and higher temperature sputtering were performed with hopes to increase grain size, x-ray diffraction patterns indicated that grains still did not exceed 200nm through the Debye-Scherrer estimate. Photoluminescence also was never observed with the sputtered films. Poor electron transport and lack of radiative output may primarily be caused by the nanocrystalline nature of the sputtered films. Low electronic mobilities, trap states from defects, and degeneracy prevent the measurement of certain material properties and construction of sufficiently photoactive devices.

Degenerate electronic materials do not work well as most active materials in devices such as LEDs and solar cells. Due to their higher carrier concentrations, degenerate materials have difficulty forming large depletion widths to influence excited carriers around junctions. In addition, degenerate materials have a higher density of scattering centers from donor ions that reduce mobilities and increase recombination rates of excited carriers, diminishing diffusion lengths.

Carrier diffusion is inversely proportional to carrier lifetime, where lifetime is the average time an excited carrier exists before recombining. There are several main

types of recombination: Shockley-Reed-Hall recombination, Auger recombination, and band-to-band radiative recombination. Shockley-Reed-Hall recombination occurs due to trap states, formed from impurities or defects, where an excited carrier drops into a mid-gap trap state and then recombines. Alternatively, Auger recombination is a band-to-band recombination, but the energy of the excited carrier goes to promoting an electron in the conduction band to higher energy, which then loses its energy through thermalization. Auger recombination often occurs in materials with high carrier concentrations to supply the third carrier. Band-to-band radiative recombination, where the excited carrier's energy is lost to light emission, would generally otherwise occur instead of Auger.

Thus, recombination rates are related to electronic, photoemission, and photoreponse properties and tied to crystallinity, defects, impurities, and dopant densities. To overcome these issues in the sputtered films and achieve higher mobilities, fewer defects and impurities, and radiative recombination,  $\text{ZnSn}_x\text{Ge}_{1-x}\text{N}_2$  growth by molecular beam epitaxy (MBE) was approached. MBE is a technique that is widely known to produce high-quality single-crystal thin films [68, 69]. Using a nitrogen atom plasma source and metal evaporation sources, plasma-assisted MBE provides a gentler synthesis route compared to sputtering, where in sputtering the reactants are composed of bombarded atoms. Furthermore, as the flux from the metal sources is separate from the flux from the nitrogen plasma source, MBE can decouple the plasma with the metal beams, allowing greater control over reactants. Finally, the MBE chamber used is not a shared instrument and as a result, has fewer contaminants. Through plasma-assisted MBE, we hope to achieve large-grain to single-crystal  $\text{ZnSn}_x\text{Ge}_{1-x}\text{N}_2$  and compare our results to the sputtered films.

Figure 5.1 shows the schematic of the MBE chamber used to grow and analyze epitaxial  $\text{ZnSn}_x\text{Ge}_{1-x}\text{N}_2$  ( $0 \leq x \leq 1$ ) films. A sample load-lock connects to the main chamber to maintain a high vacuum to ultra-high vacuum environment. Individual elemental Zn, Sn, and Ge Knudsen cells are directed at the substrate and hold discrete temperatures to provide the metal/semi-metal precursors. An RF atom source supplied with nitrogen gas provides activated nitrogen to the deposition. The walls of

the main chamber are water cooled to prevent contamination from the sidewalls, so that metals or residual gases do not re-evaporate and that precursors solely originate from the controlled sources. The chamber is equipped with in-vacuo Reflection High Energy Electron Diffraction (RHEED) system to analyze the surface structure of the substrates and films.

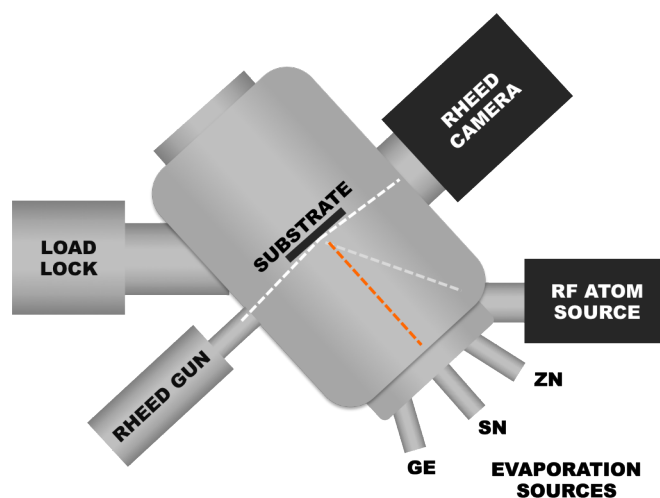


Figure 5.1: Schematic of nitride molecular beam epitaxy instrument. An RF atom source supplied with nitrogen gas provides activated nitrogen to the deposition, while elemental metals and semi-metals are emitted from the evaporation sources. The chamber is equipped with in-vacuo RHEED to analyze the surface structure of the substrates and films.

Figure 5.2 displays the RHEED patterns for c-plane sapphire substrates and c-plane GaN template on sapphire substrates. The substrate RHEED displays both  $[11-20]$  and  $[10-10]$  azimuthal directions. RHEED patterns of the substrates show the quality of the epitaxial-ready surfaces and assist in standardizing the lattice parameter spacing and orientation of MBE films. The presence of Kikuchi lines represents high crystal quality at the surface.

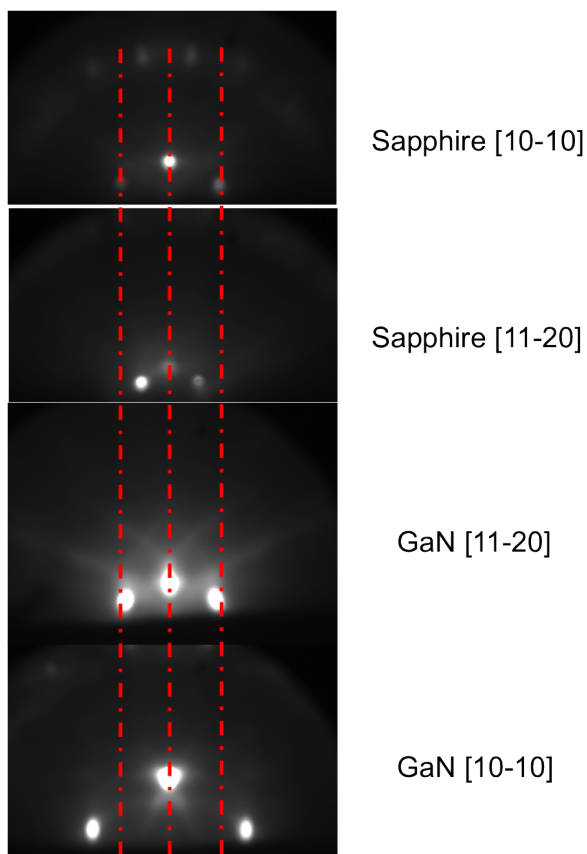


Figure 5.2: RHEED patterns for (001) Sapphire and GaN templates for both [11-20] and [10-10] azimuthal directions.

## 5.2 Growth of epitaxial hexagonal $\text{ZnSn}_x\text{Ge}_{1-x}\text{N}_2$ by MBE

As mentioned in Chapter 1, MBE growth of  $\text{ZnSnN}_2$  had been published by Feldberg et al. [10] on cubic yttrium-doped zirconia substrates. Their analysis reported growth of monoclinic  $\text{ZnSnN}_2$ . Their substrate temperatures were held at 400C and films often had metal islands on the surface after growth. Although RHEED and XRD patterns indicated smooth, crystalline film growth, no transmission electron micrographs were shown to exhibit the epitaxial nature.

In this work, a range of  $\text{ZnSn}_x\text{Ge}_{1-x}\text{N}_2$  alloys have been grown on hexagonal-based substrates: sapphire and GaN templates on sapphire. Substrate temperatures were mainly 250C. Initial growths of  $\text{ZnSnN}_2$  had slow deposition rates and were limited

by the nitrogen flux to the substrate. Films grown for nine hours on sapphire did not exceed 150nm thickness. They also exhibited multiple orientations, indicating lack of epitaxy and oriented texture to the c-plane sapphire substrate (Fig. 5.3).

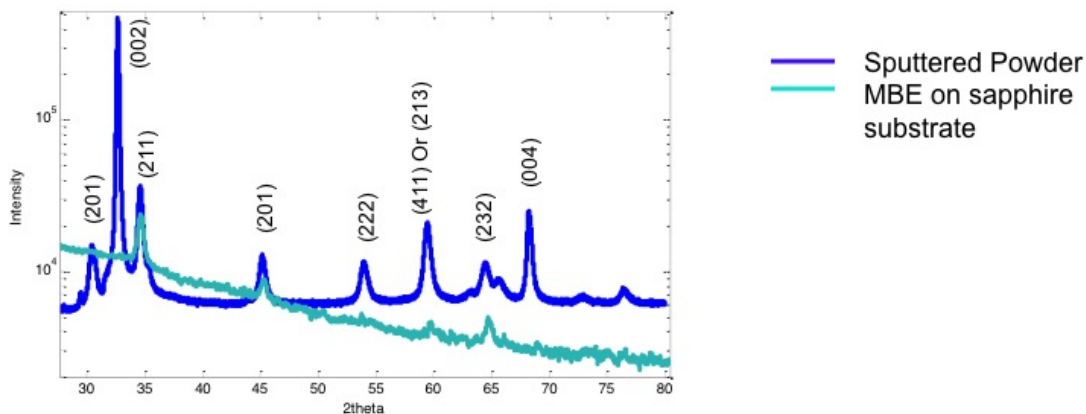


Figure 5.3: Grazing XRD of initial, nitrogen-flux limited  $\text{ZnSnN}_2$  MBE growth on sapphire compared to  $\text{ZnSnN}_2$  powder pattern.

To improve growth rates, nitrogen flux was increased by permitting more flux from the RF source and moving the beam closer to the substrate. On the RF source, the  $\sim 30$ -hole aperture plate was exchanged with a 488-hole aperture plate, and the whole source was translated 10" closer to the substrate. Improved growth rates, crystallinity, and orientation of  $\text{ZnSnN}_2$  films were achieved with the nitrogen RF source modifications. Introducing the 488-hole aperture plate improved the crystallinity, as RHEED patterns transformed from amorphous washes to patterns of diffraction spots, indicating 3D diffraction from the surface. Higher growth rates were achieved with translating the plasma source closer to the substrate, as XRD peaks with greater intensity were produced. Table 5.1 lists the parameters for subsequent improved growths and their resulting stoichiometries by XPS. Error in XPS stoichiometry determination is generally  $\pm$  atomic 10%, and only probes the first  $\sim 10$ nm of the film. Films grown for approximately 3 hours had thicknesses of about 30nm on GaN, as seen in the transmission electron microscopy (TEM) cross section images (5.13) and modeled from the thickness fringes of the XRD (002) peak (5.10).

Sample	Tsubs. [C]	N2 [torr]	RF power [W]	TZn [C]	TSn [C]	TGe [C]	%N	%Zn	%Sn	%Ge
MBE45	250	6.5E-5	300	275	900	-	52	28	20	-
MBE61	250	6.5E-5	300	275	900	-	59*	13*	28*	-
MBE46G	250	6.5E-5	300	275	900	-	56	21	23	-
MBE47	250	6.5E-5	300	275	900	775	52	26	20	2
MBE53	250	6.5E-5	300	275	860	1175	49	30	13	8
MBE54	250	6.5E-5	300	275	860	1200	52	26	12	9
MBE55	250	6.5E-5	300	275	830	1225	51	25	7	18
MBE56	250	6.5E-5	300	275	810	1250	50	22	3	25
MBE57G	250	6.5E-5	300	275	830	1225	50	22	8	20
MBE63	250	6.5E-5	300	275	845	1215	51	18	10	21
MBE64G	250	6.5E-5	300	275	845	1215	53	22	11	14
MBE62	250	6.5E-5	300	275	845	1215	52	17	12	19

Table 5.1: Growth conditions and resulting stoichiometries by XPS for improved crystalline MBE samples. Samples labeled MBE###G used GaN substrates, while the remaining are on sapphire. \* denotes surface stoichiometry different from bulk.

After chamber modifications, crystalline  $\text{ZnSnN}_2$  films were first observed through their in-situ RHEED patterns. Figure 5.4 displays the electron diffraction for  $\text{ZnSnN}_2$  grown on sapphire and GaN substrates for the [11-20] and [10-10] azimuthal directions. RHEED patterns for  $\text{ZnSnN}_2$  films on sapphire are spotted due to islanded 3D growth and those on GaN are streaked as they form cohesive 2D films. This difference in growth mechanism is due to the lattice mismatch with the substrate, clearly seen when comparing the sapphire planar spacing with the  $\text{ZnSnN}_2$  film on GaN.

Although the crystalline pattern for the 3D growth may look blurred and towards a polycrystalline sample, the e-beam energy when taking the pattern was 7 keV, which is lower than the usual 9 keV energy used for the other patterns, broadening the diffraction spots. Furthermore, x-ray diffraction performed revealed that the films only had one orientation. Simulations of electron transmission diffraction of wurtzite GaN showed RHEED patterns were similar to spots from the  $\text{ZnSn}_x\text{Ge}_{1-x}\text{N}_2$  films grown on sapphire (Figure 5.5) .

Continued RHEED analysis for  $\text{ZnSn}_x\text{Ge}_{1-x}\text{N}_2$  grown on GaN and sapphire are represented in Figures 5.6 and 5.7. Comparisons of the diffraction pattern spacing indicate a slight decrease in real planar distances going from  $\text{ZnSnN}_2$  to  $\text{ZnSn}_x\text{Ge}_{1-x}\text{N}_2$  in the [10-10] direction, as expected when the smaller Ge atom is inserted. An

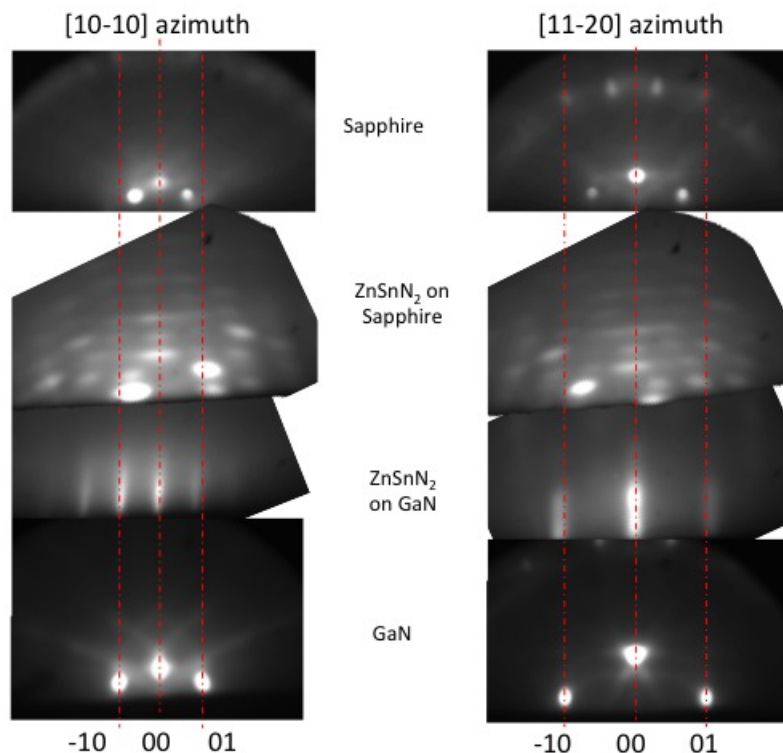


Figure 5.4:  $\text{ZnSnN}_2$  RHEED in  $[11-20]$  and  $[10-10]$  azimuthal directions for sapphire and GaN. For  $\text{ZnSnN}_2$  on sapphire, spots instead of streaks are present due to 3D film growth, likely from the lattice mismatch between  $\text{ZnSnN}_2$  and sapphire.

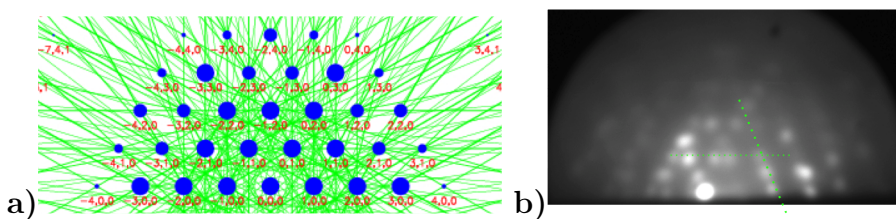


Figure 5.5: a) Simulated EMAPS (Reference: Zuo and Mabon, *Micosc. Microanal.* 2004) of selected area transmission diffraction pattern for a wurtzite GaN lattice compared to b)  $\text{ZnSn}_x\text{Ge}_{1-x}\text{N}_2$  RHEED transmission diffraction. The  $\text{ZnSn}_x\text{Ge}_{1-x}\text{N}_2$  RHEED reflections have similar symmetry as the simulated hexagonal GaN pattern for transmission diffraction, as expected for the  $\text{ZnSn}_x\text{Ge}_{1-x}\text{N}_2$  crystal structure.

increase for real interplanar spacings in the  $[11-20]$  direction from  $\text{ZnSnN}_2$  to  $\text{ZnSn}_x\text{Ge}_{1-x}\text{N}_2$  is less expected, but the compressed  $\text{ZnSnN}_2$  planar spacing may have resulted from distortions due to strain in the larger  $\text{ZnSnN}_2$  lattice from the epitaxy. Also

unexpected was the transition from 3D growth to a 2D film surface for  $\text{ZnSn}_x\text{Ge}_{1-x}\text{N}_2$  on sapphire, seen in Figure 5.7. This may have occurred through coalescence of 3D islands to form a 2D film at the surface. Overall, these RHEED measurements probe only the first several monolayers of the film, so may not represent the entire film properties.

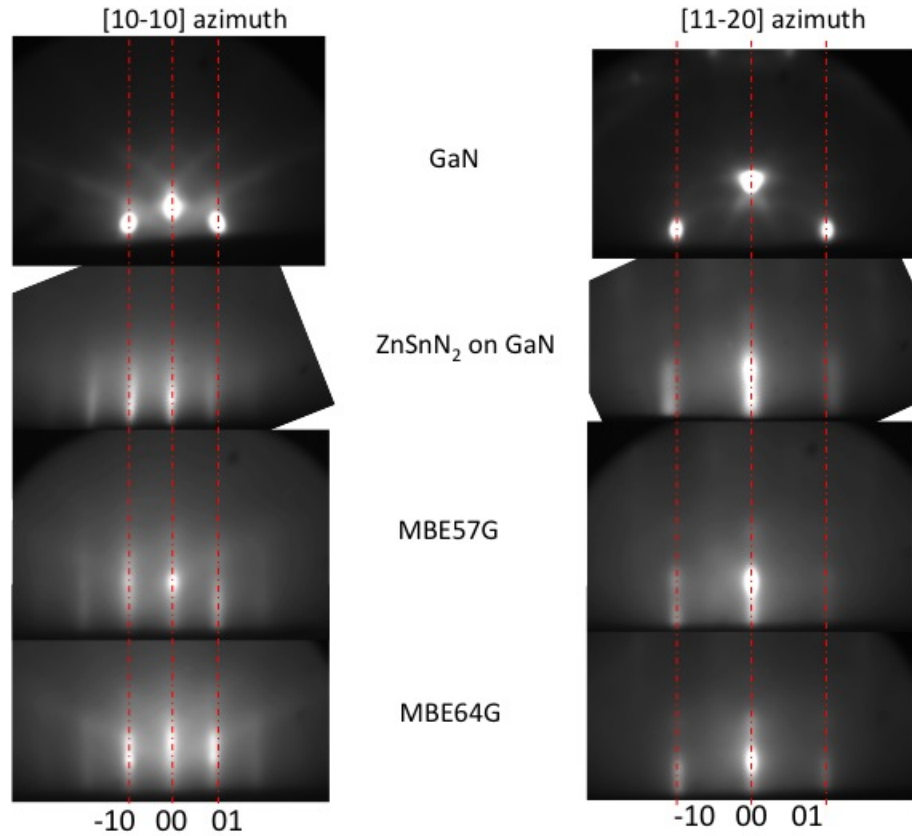


Figure 5.6: RHEED of  $\text{ZnSn}_x\text{Ge}_{1-x}\text{N}_2$  on GaN in the  $[11\bar{2}0]$  and  $[10\bar{1}0]$  azimuthal directions. All conditions grew smooth 2D films. Lattice parameter differences for  $\text{ZnSnN}_2$  can be seen in the RHEED streak misalignment, where the  $\text{ZnSnN}_2$  on  $[11\bar{2}0]$

After removing samples from the MBE chamber, other structural measurements were performed to verify the RHEED surface findings. Figure 5.8 shows x-ray diffractograms of  $\text{ZnSnN}_2$  and several compositions of  $\text{ZnSn}_x\text{Ge}_{1-x}\text{N}_2$  on hexagonal-based  $c$ -plane sapphire substrates. The sole presence of the  $(002)$   $\text{ZnSn}_x\text{Ge}_{1-x}\text{N}_2$  peak and only its higher reflections indicate that films are oriented. The presence of periodic Pendellosung oscillations on the  $(002)$  peak indicate sharp interfaces between the film

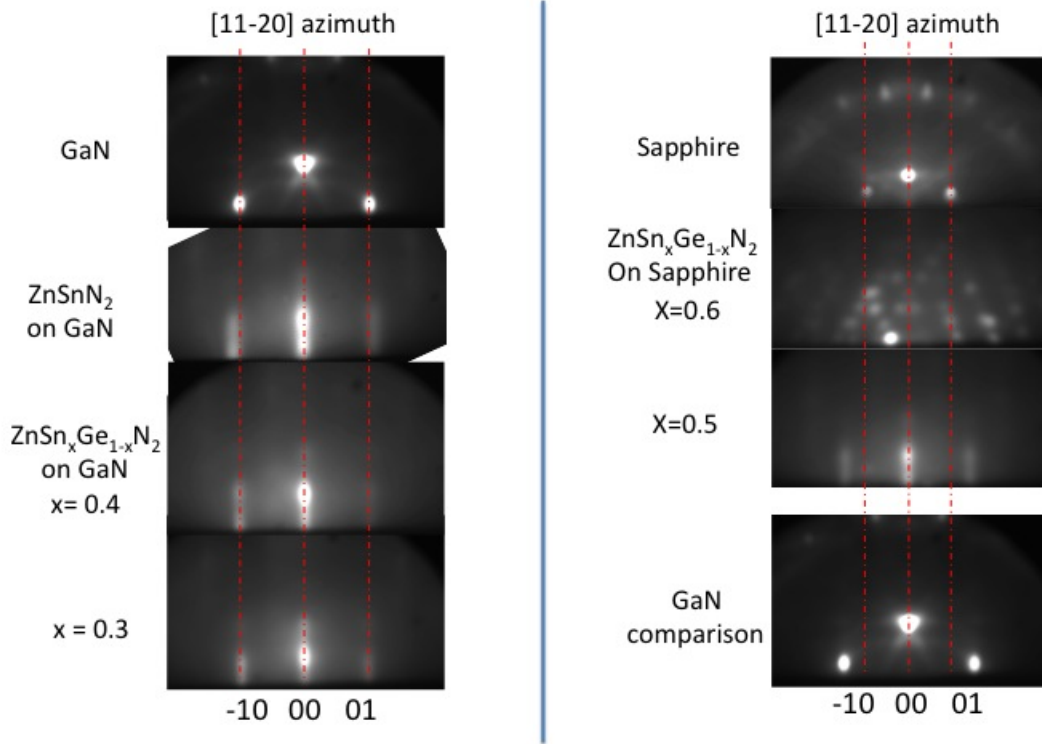


Figure 5.7: RHEED [11-20] azimuthal directions for Zn grown on GaN and sapphire. Better lattice matching is seen for  $\text{ZnSn}_x\text{Ge}_{1-x}\text{N}_2$  on sapphire, at higher tin concentrations, 3D growth ensued. Going to lower tin concentrations and higher germanium concentrations, diffraction resulted from 2D film surfaces. Potential causes may be from relaxation from strained islands to coalescing into a smooth surface.

and substrate, and pseudomorphic growth which is representative of heteroepitaxy. Growth of  $\text{ZnSnN}_2$  on sapphire did not exhibit such fringes, implying a less continuously epitaxial interface, potentially from the lattice mismatch of  $\sim 20\%$  between sapphire and  $\text{ZnSnN}_2$ .

Similarly, Figure 5.9 displays diffractograms  $\text{ZnSn}_x\text{Ge}_{1-x}\text{N}_2$  MBE films grown on hexagonal-based GaN substrates, with strong Pendellosung oscillations, even with  $\text{ZnSnN}_2$  films. GaN and  $\text{ZnSnN}_2$  have  $< 5\%$  lattice mismatch, allowing better heteroepitaxy to proceed. Figures 5.13a) and b) show the high-resolution transmission electron microscopy [HRTEM] of the GaN to  $\text{ZnSnN}_2$  and  $\text{ZnSn}_x\text{Ge}_{1-x}\text{N}_2$  interfaces.

Figure 5.10 compares the oriented, sputter-deposited films and improved MBE

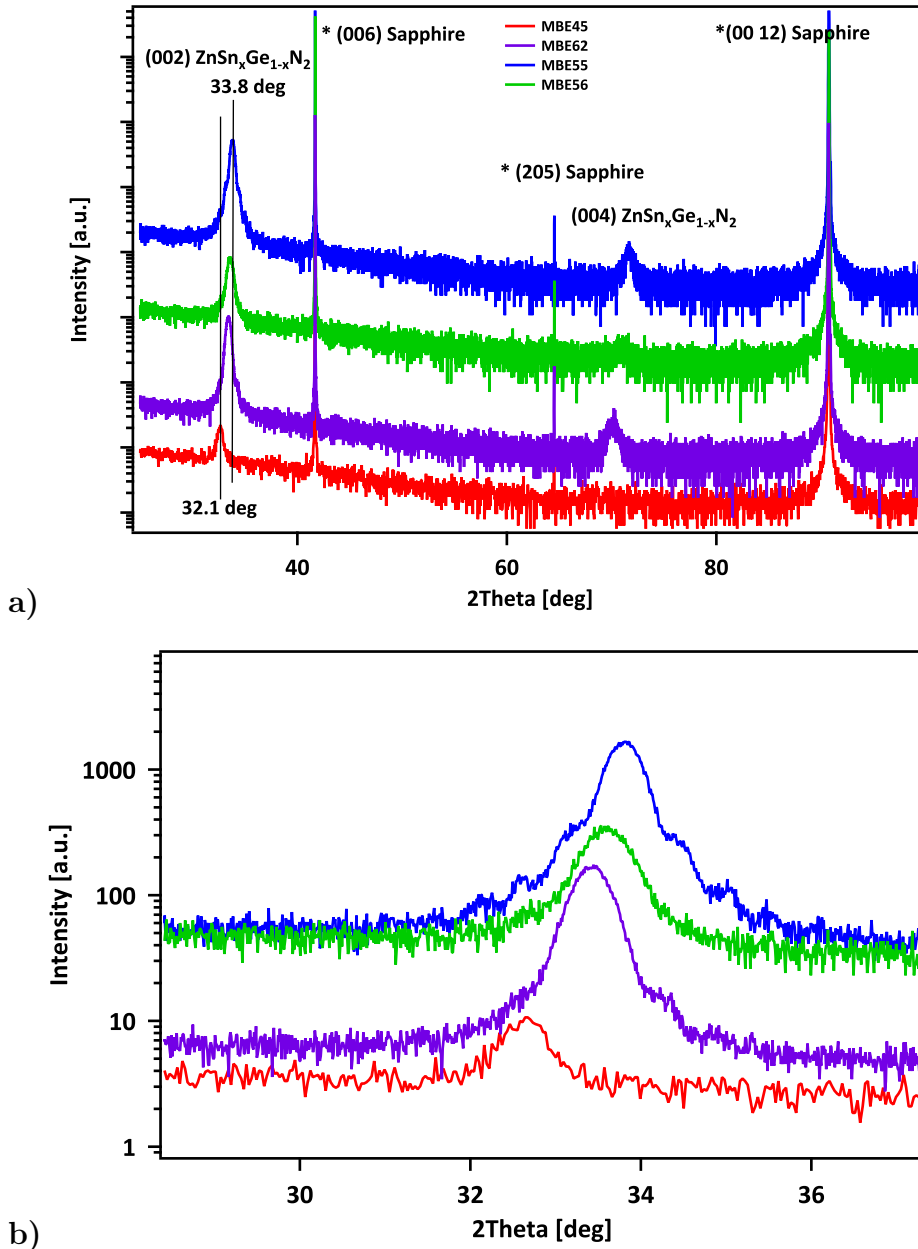


Figure 5.8: a) XRD patterns of MBE grown  $\text{ZnSn}_x\text{Ge}_{1-x}\text{N}_2$  on (001) c-sapphire. Sole presence of (002) peak indicates films are oriented. b) The presence of periodic Pendellosung oscillations on the (002) peak indicate sharp interfaces between the film and substrate and pseudomorphic growth representative of heteroepitaxy.

films showing the same preferential orientation. (002)  $\text{ZnSnN}_2$  peak positions do not align exactly between all films, potentially attributed to shifts from differing strain and epitaxy. Figure 5.11 lists the peak positions for MBE films compared to sputtered films across the series. Similar to the  $\text{ZnSnN}_2$  case, peak positions do not match for the

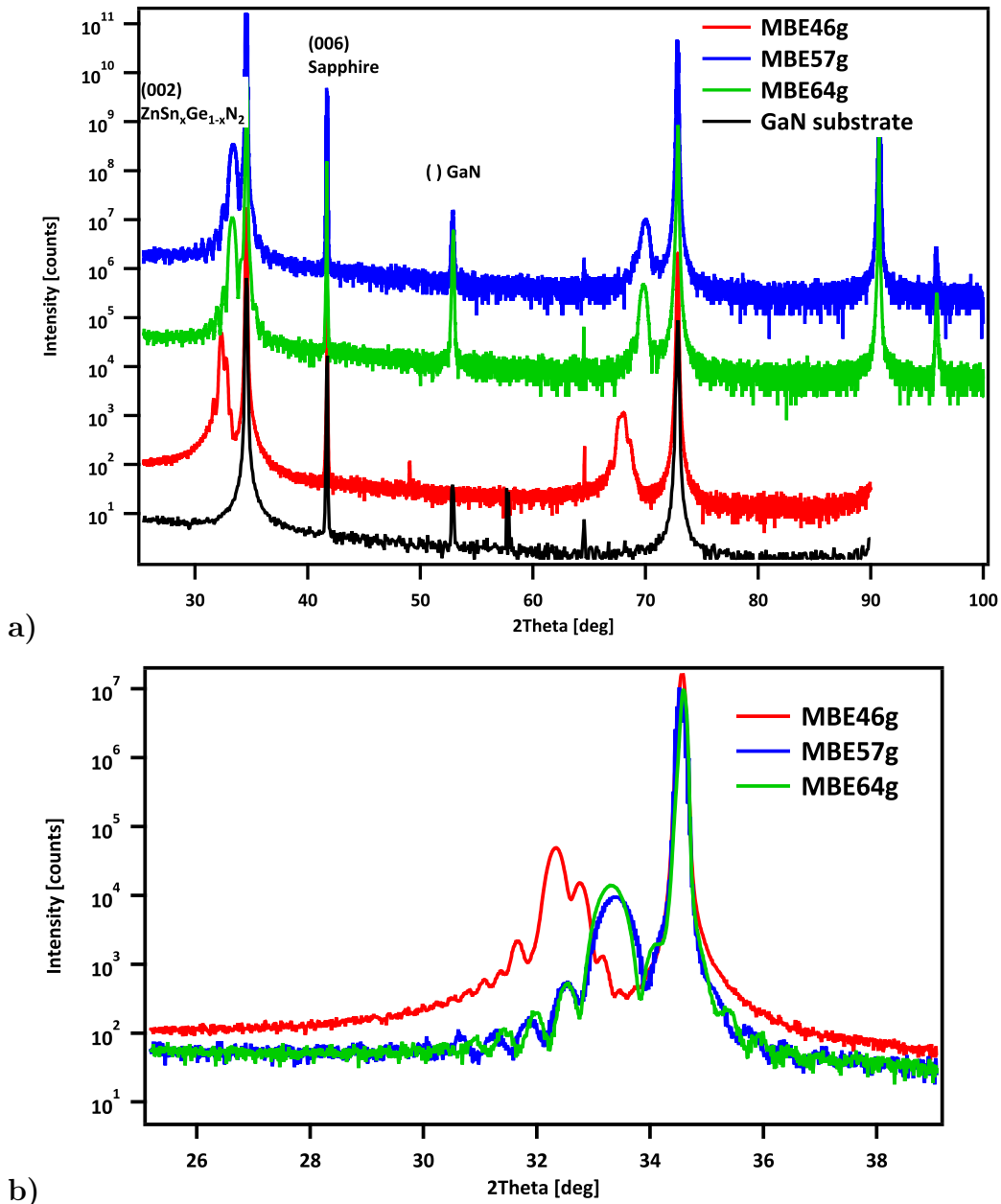


Figure 5.9: a) XRD patterns of MBE grown  $\text{ZnSn}_x\text{Ge}_{1-x}\text{N}_2$  on wurtzite (001) GaN. b) Pendellosung oscillations are present on both  $\text{ZnSnN}_2$  and  $\text{ZnSn}_x\text{Ge}_{1-x}\text{N}_2$  alloys indicating pseudomorphic growth. The  $\text{ZnSnN}_2$   $a$  parameter has less lattice mismatch with GaN than sapphire, allowing epitaxial growth to occur, and 2D, smooth films.

sputtered films and MBE films at the various  $\text{ZnSn}_x\text{Ge}_{1-x}\text{N}_2$  stoichiometries. Although there may be a linear trend for the MBE films to correlate with Vegard's Law, there is a wider spread in peak position measured than for the sputtered films. Therefore,

it is difficult to determine how the strain or relaxation influences the c-plane spacing across the series. More samples and data points should be deposited to obtain a better trend.

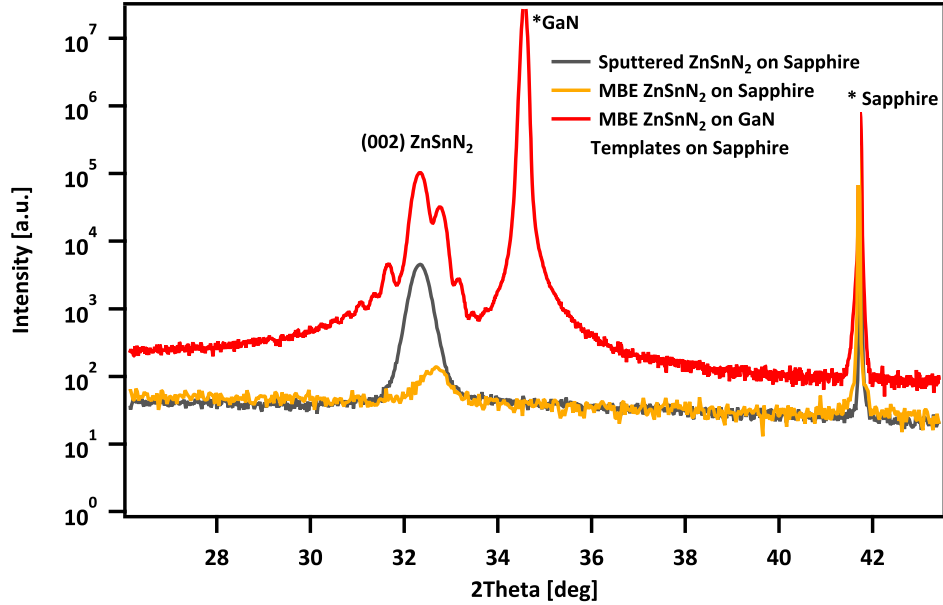


Figure 5.10: XRD of sputtered ZnSnN<sub>2</sub> compared to improved MBE growths on sapphire and GaN. Sputtered peak positions do not match with MBE films potentially due to strain.

In plane diffraction was performed to verify the symmetry of the films. Phi scans were performed by tilting the [001] axis  $\sim 60$  degrees in psi, orienting the n or r planes to satisfy the Bragg condition, then rotating 360 degrees about the the [001] axis. Six major peaks were observed, confirming hexagonal symmetry. Alignment of the substrate peak positions with the film peak positions define the orientation of the film on substrate as hexagon-on-hexagon, rather than an off-set position from the major lattice hexagon to a site translated  $a$  distance in  $\langle 100 \rangle$  or  $\langle 010 \rangle$  or any rotation of the film orientation. These phi scans further support the film heteroepitaxy.

Finally, transmission electron micrographs (TEM) of ZnSnN<sub>2</sub> on GaN and ZnSn<sub>x</sub>Ge<sub>1-x</sub>N<sub>2</sub> on GaN in Figure 5.13 and 5.14 display the clean heteroepitaxy. Cross-sections appear with little to no noticeable defects at the interface or throughout the films. Films show specular quality, with no grain boundaries visible from the surface, producing single-crystalline thin films grown at low temperatures of 250C. Observation

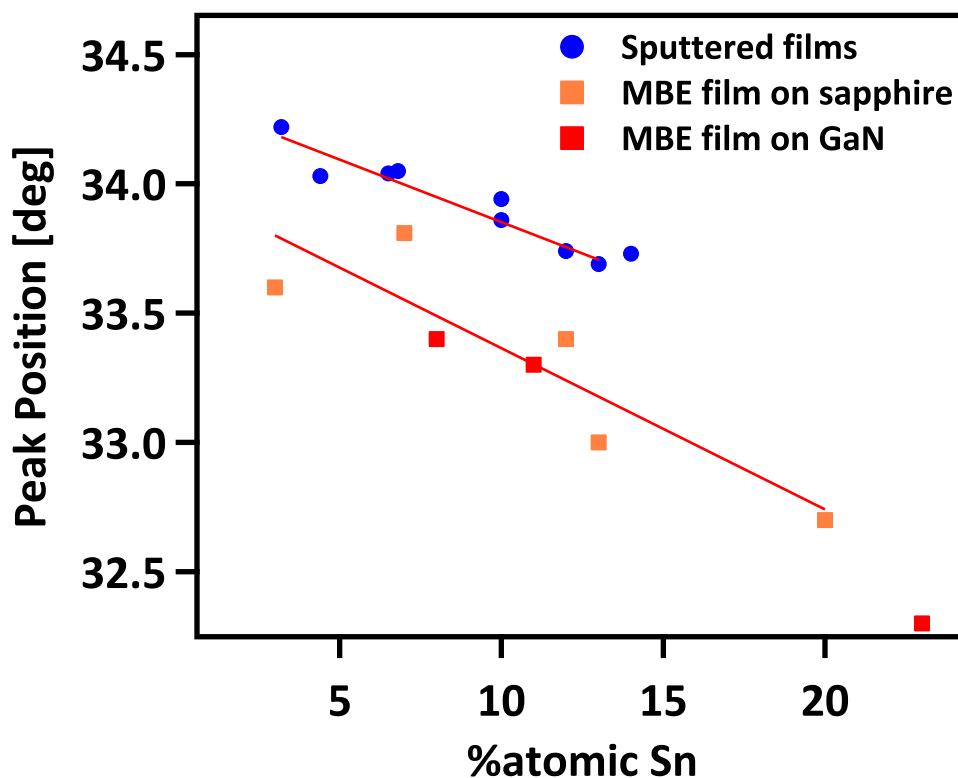


Figure 5.11: Plot of  $\text{ZnSn}_x\text{Ge}_{1-x}\text{N}_2$  peak positions vs tin concentration show sputtered films have a different shift compared to MBE films potentially due to strain.

of contrast in the TEM images agrees with peak position shifts that strain is present in the films. Film quality may change with thickness or annealing where the strain can relax.

Lattice parameters can be calculated from selected area diffraction performed in the transmission electron microscope. Using an electron beam energy of 300keV, the camera length as 250mm, and the substrate lattice parameters and plane spacings, the film lattice parameters and plane spacings can be calculated by the distances on the images taken. A polycrystalline gold standard at the exact same energy and camera length were used for calibrating the distances. For a hexagonal lattice, the general relation is listed in Equation 5.2.  $h, k, l$  are the plane indices and  $a$  and  $c$  are the lattice parameters.  $d$  is the spacing between  $(h k l)$  planes. However, arrangement of the Zn-IV-Nitride lattices are orthorhombic, thus geometric calculations are performed to obtain the orthorhombic  $a$  and  $c$ . The  $b$  lattice parameters cannot be

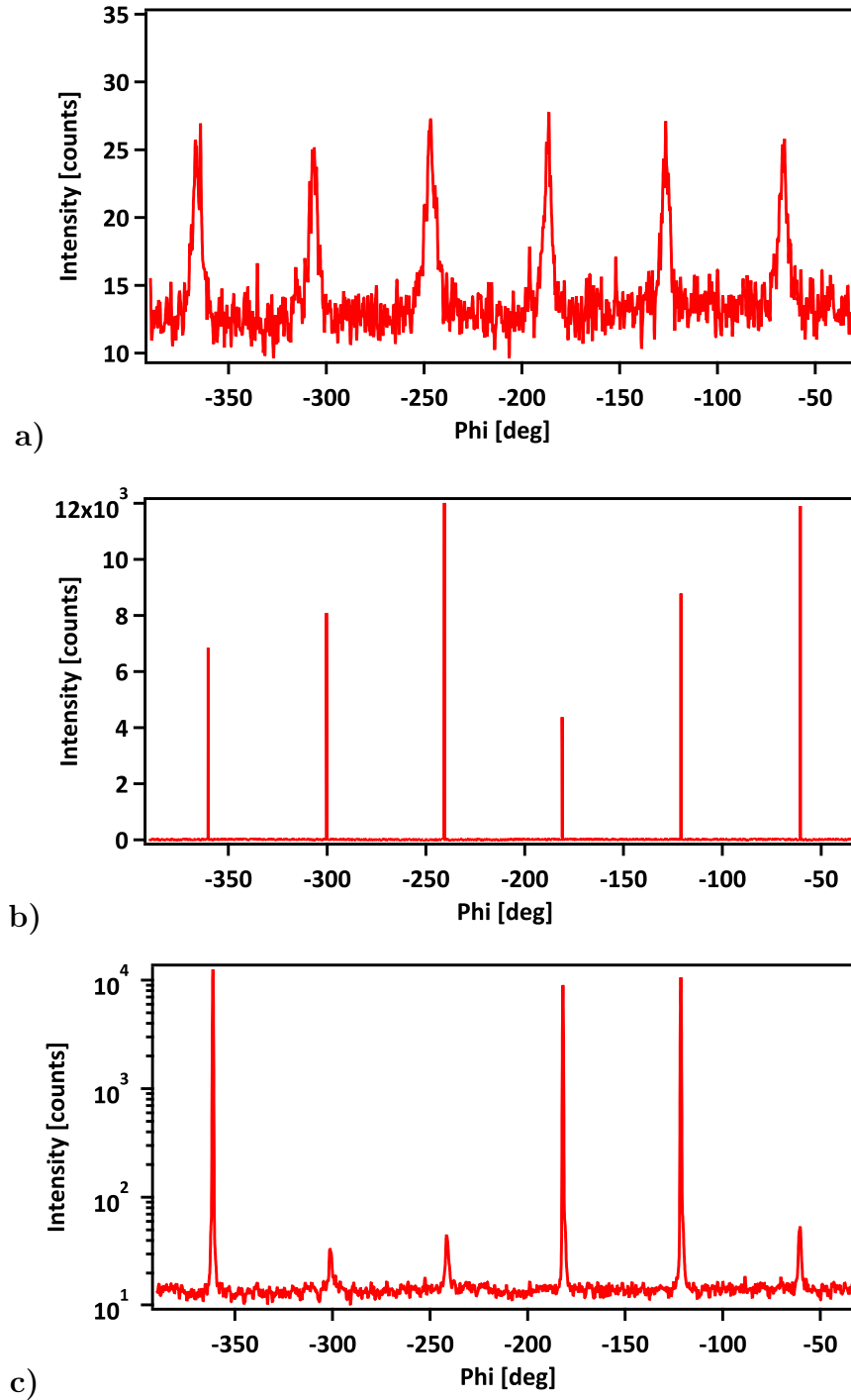


Figure 5.12: Phi scan of MBE55 on sapphire with psi angle 60 degrees. Six major peaks appear, representing hexagonal symmetry. b) The sapphire phi scan. Alignment of peaks indicate a hexagon-on-hexagon growth. c) Phi scan of MBE64G on GaN. The intersecting substrate and film peaks also reflect hexagon-on-hexagon growth.

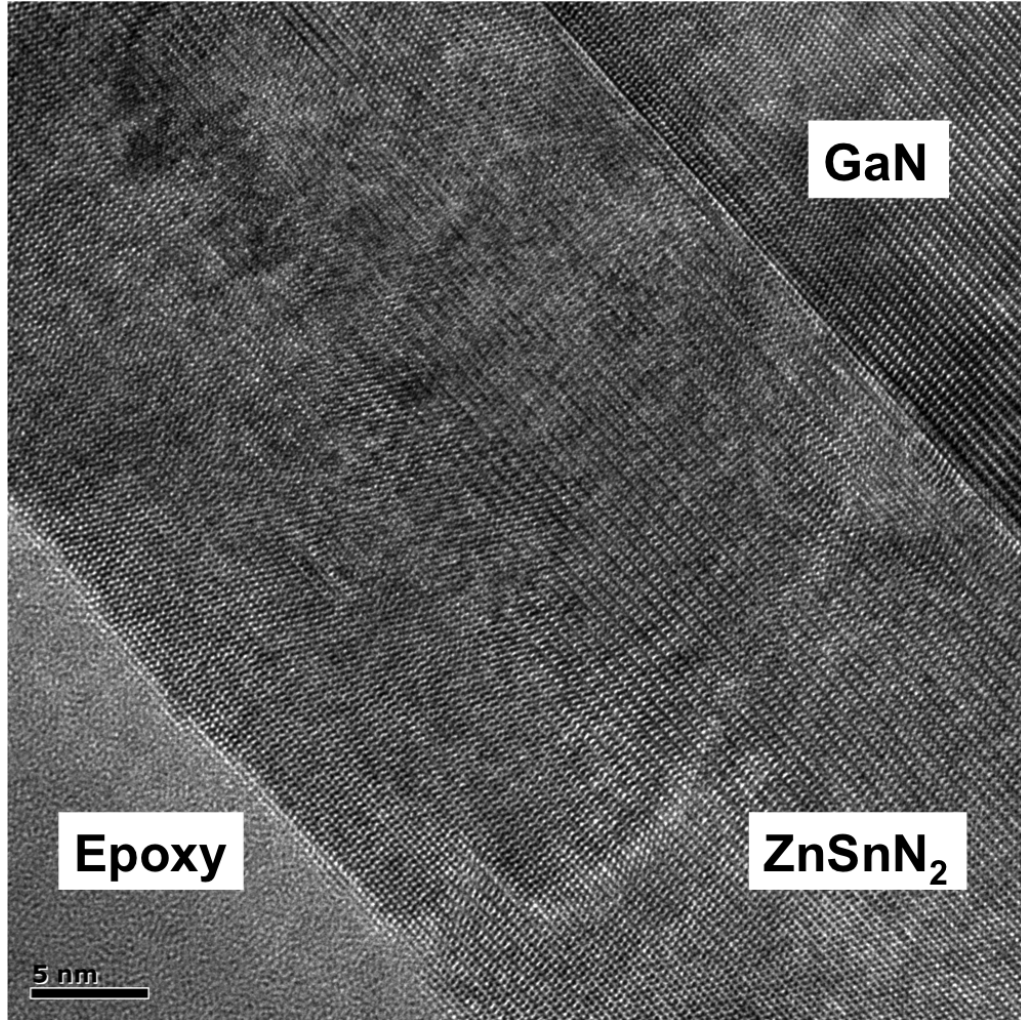


Figure 5.13: HRTEM of film-GaN substrate interface exhibiting epitaxy for ZnSnN<sub>2</sub> MBE46G. The image shows the film at  $\sim 30$ nm thick with clean heteroepitaxy to the substrate, and single-crystal quality. Contrast in the film exhibits the strain present. TEM courtesy of Carol M Garland.

obtained because films are oriented.

$$\frac{1}{d^2} = \frac{h^2+k^2}{a^2} + \frac{l^2}{c^2} \text{ Equation 5.2}$$

Electronic properties of MBE films were measured and compared to the sputtered films. The resistivities of MBE films display a similar trend to the sputtered films, still leaving the ZnSnN<sub>2</sub> in the degenerate regime and featuring increased resistivities toward low-tin ZnSn<sub>x</sub>Ge<sub>1-x</sub>N<sub>2</sub> samples. Hall measurements for the ZnSnN<sub>2</sub> films exhibit increased mobilities from  $\sim 1 \text{ cm}^2\text{V}^{-1}\text{s}^{-1}$  to  $\sim 20 \text{ cm}^2\text{V}^{-1}\text{s}^{-1}$ . Some ZnSn<sub>x</sub>Ge<sub>1-x</sub>N<sub>2</sub> films have had trouble ohmically contacting, which provides some outlook that ZnSn<sub>x</sub>Ge<sub>1-</sub>

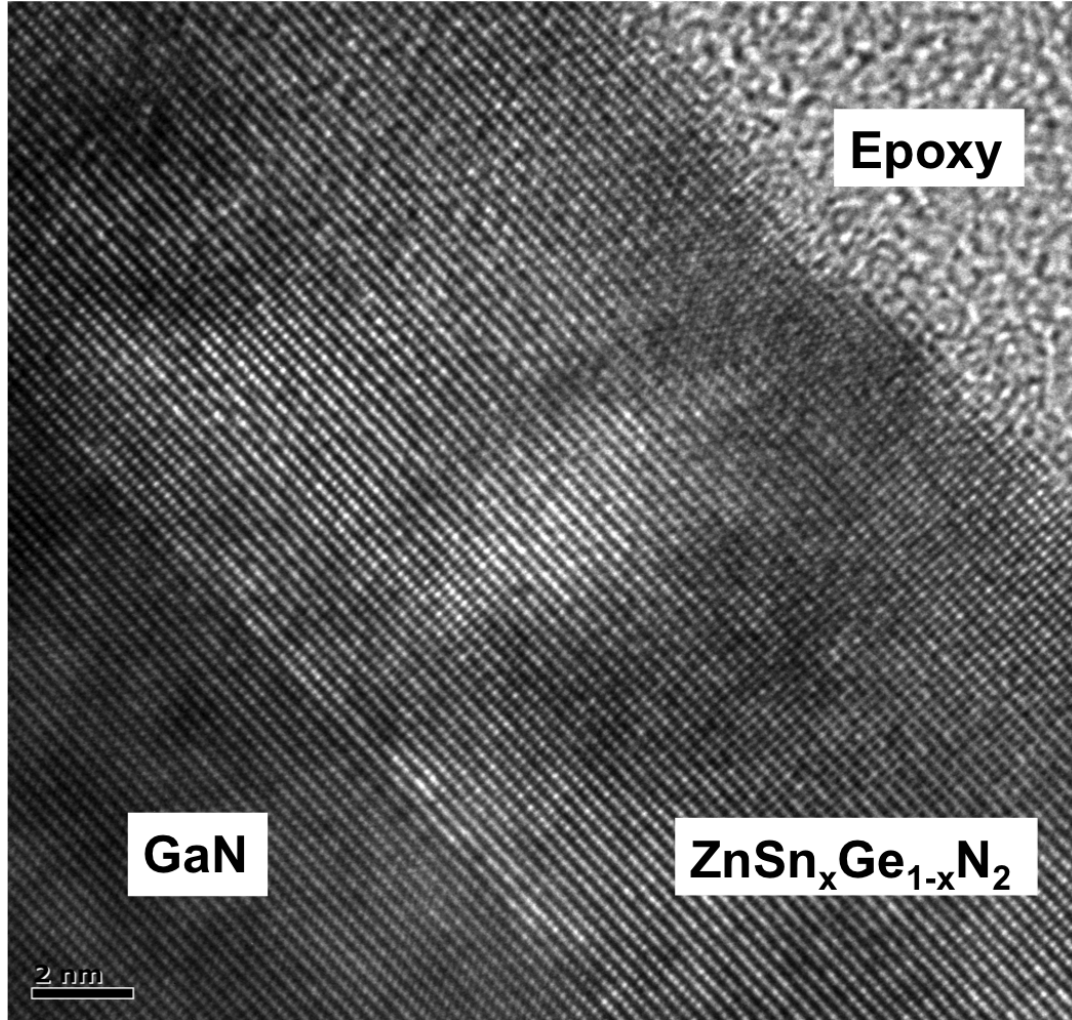


Figure 5.14: HRTEM of  $\text{ZnSn}_x\text{Ge}_{1-x}\text{N}_2$  MBE57G on GaN substrate. It contains qualities similar to the HRTEM of  $\text{ZnSnN}_2$  film on GaN.

	Measured Lattice Parameter [nm]		
	$a$	$b$	$c$
MBE 46G $\text{ZnSnN}_2$	1.122	-	1.039
MBE 57G $\text{ZnSn}_x\text{Ge}_{1-x}\text{N}_2$	0.6592	-	0.5291

Table 5.2: Interfacial lattice parameters calculated from SAED of MBE films on GaN substrates. MBE  $\text{ZnSnN}_2$  films are strained on GaN and an average lattice parameters are given. Films are oriented on the substrate, so only  $a$  and  $c$  parameters can be calculated.

$\text{xN}_2$  MBE films do not have the full electronic properties of sputtered films across the alloy series.

MBE films exhibit photoconductivity like the sputtered films. A long-time re-

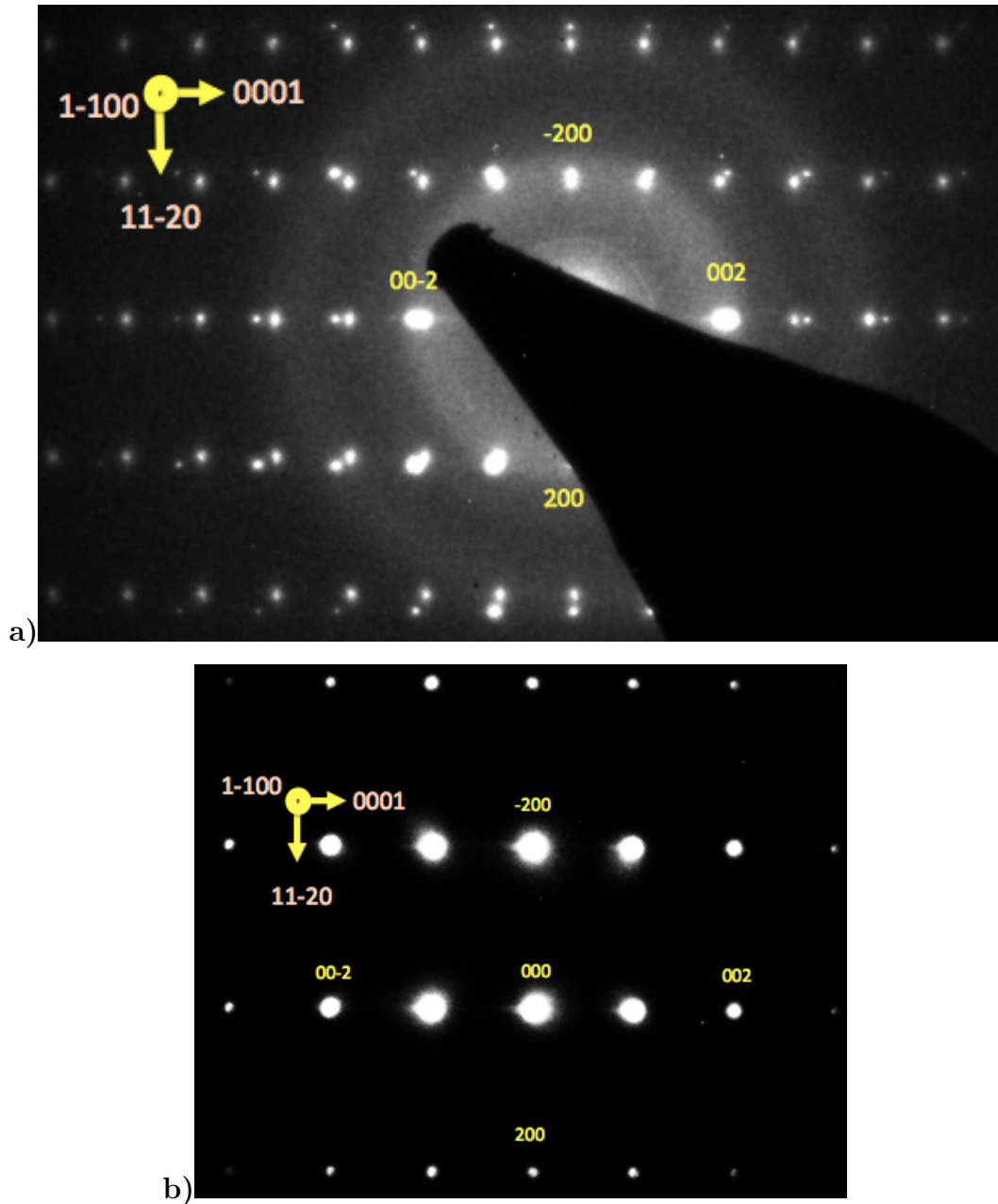


Figure 5.15: Selected Area Electron Diffraction of a)  $\text{ZnSnN}_2$  MBE46G and b)  $\text{ZnSn}_x\text{Ge}_{1-x}\text{N}_2$  MBE57G on GaN. The substrate reflections are clearly separated from the  $\text{ZnSnN}_2$  reflections, showing the lattice mismatch, whereas the  $\text{ZnSn}_x\text{Ge}_{1-x}\text{N}_2$  reflections sit on the substrate peaks. The amorphous rings in the  $\text{ZnSnN}_2$  SAD are from epoxy applied to the sample. Diffraction spots are labeled for the orthorhombic  $\text{ZnSn}_x\text{Ge}_{1-x}\text{N}_2$ .

response is observed for  $\text{ZnSnN}_2$  films, but the response time decreases as the alloys increase in Ge content. For films on GaN, the response time is faster, but may be

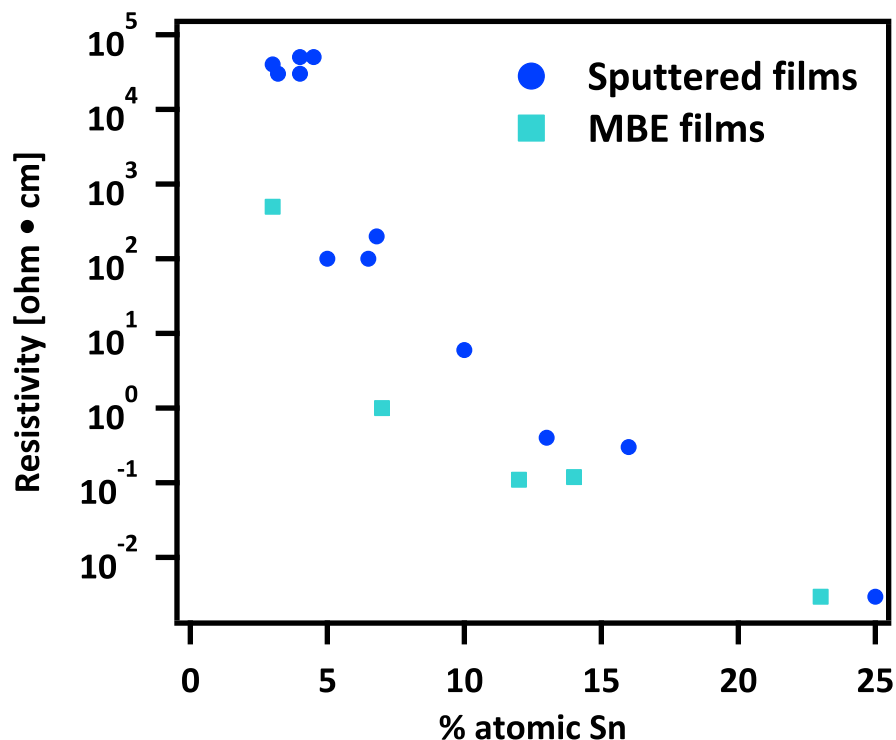


Figure 5.16: Resistivity increases with a similar trend as the sputtered films. Stoichiometry for sputtered films was measured by EDS, where stoichiometry for MBE films were measured by XPS.

linked with the substrate photoactivity. Luminescence for the 30 nm films at room temperature was not observed, potentially because defect states still exist- as evidenced by the photoresponse in Figure 5.17- or lack of active material. Thicker films should be tried for examination of photoluminescence.

Several reasons exist as to why the high-crystalline quality MBE films would not act as the ideal direct band gap materials expected from calculation. Oxygen and gallium impurities from leaks or the chamber walls may still generate unwanted dopants. Analytical techniques such as Secondary Ion Mass Spectrometry (SIMS) can possibly identify dopant level concentrations of these undesirable elements. Although TEM displayed coherency in the cross-section, films were strained and may still include anti-site defects, which induce changes to the band structure and produce results not anticipated from ideal simulations.

Raman spectroscopy reveals the presence of disorder in the lattice. Raman spec-

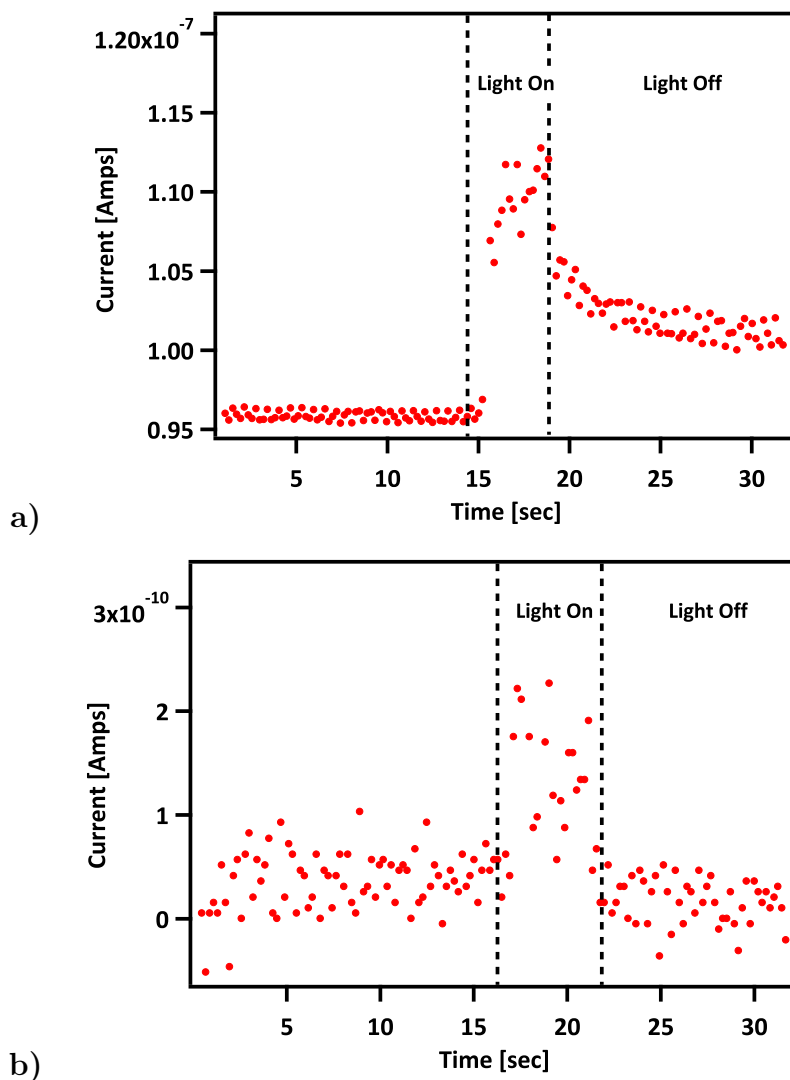


Figure 5.17: Photoactivity using a 2-point probe at a 3V bias with 405nm laser illumination on low-tin MBE  $\text{ZnSn}_x\text{Ge}_{1-x}\text{N}_2$  films on a) sapphire and b) GaN.

troscopy probes bond vibrations and sharp peaks are expected for solids with defined bonds, unlike amorphous solids which have broad features. Although from structural measurements and TEM, MBE films appear with few structural imperfections like grain boundaries, dislocations, or twinning, the Raman spectrum shows broad peaks at  $270\text{ cm}^{-1}$ ,  $650\text{ cm}^{-1}$ , and  $760\text{ cm}^{-1}$ . These peaks match the positions of broad peaks from the sputter-fabricated  $\text{ZnSn}_x\text{Ge}_{1-x}\text{N}_2$  films, reflecting the material congruence. These broad peaks indicate the bond vibrations probed are not well defined, representing the cation disorder occurring in the lattice. Other studies of plasma-assisted

VLS ZnSnN<sub>2</sub> growth at 485C produce similarly broad Raman peaks, attributed to anti-site defects [35]. However, the literature also includes evidence of sharp, defined Raman peaks from experiments on crystalline ZnGeN<sub>2</sub> needles grown at 750C [36]. Therefore, it may be possible to achieve higher cation ordering in ZnSn<sub>x</sub>Ge<sub>1-x</sub>N<sub>2</sub> MBE samples if higher growth temperatures are employed.

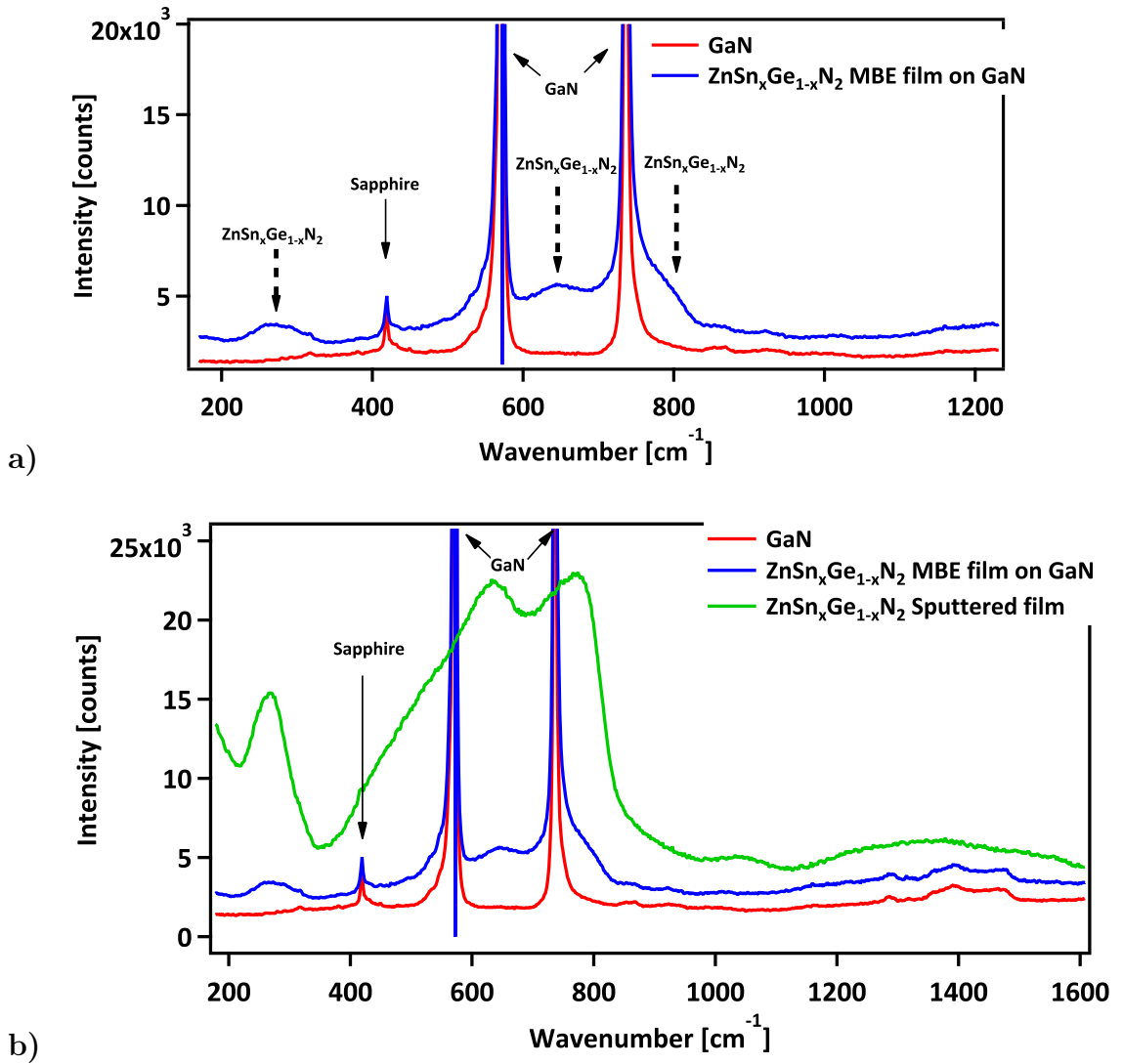


Figure 5.18: a) Raman for alloys and b) comparison to sputtered ZnSn<sub>x</sub>Ge<sub>1-x</sub>N<sub>2</sub> films

### 5.3 Improvements for MBE Growth

At current growth temperatures of 250C, MBE films have shown improved crystallinity and grain sizes leading to greater mobilities. However, the relatively low temperature of 250C can limit the incident atom mobility on the substrate, and inhibit the atom from settling in the lattice position for a perfectly ordered crystal. Although TEM displayed coherency in the cross-section, films were strained and still include anti-site defects, which induce changes to the band structure that may produce deleterious electronic effects.  $\text{ZnSn}_x\text{Ge}_{1-x}\text{N}_2$  growths at higher temperatures may relieve any defect and strain effects. Higher substrate temperatures will allow atoms to find their thermodynamic minima and ideal lattice positions before they settle. Initial attempts with deposition at higher temperatures above 400C resulted in film delamination from the substrates due to thermal expansion mismatch. Therefore, formulating high temperature growths may require different substrates or buffer layers that reduce the difference in thermal expansion coefficients. Choice of substrates affect epitaxy, crystal orientation, and electronic properties. The current  $\text{ZnSn}_x\text{Ge}_{1-x}\text{N}_2$  films grown on polar c-plane-oriented GaN and sapphire- which can also stimulate polarization at interfaces, as in InN- may be experiencing electron accumulation at the surface [70]. Thus, the substrate polarity is a potential influential factor in the resulting  $\text{ZnSn}_x\text{Ge}_{1-x}\text{N}_2$  electronic properties. Growing  $\text{ZnSn}_x\text{Ge}_{1-x}\text{N}_2$  films on non-polar r-plane, m-plane, and a-plane GaN and sapphire substrates will provide evidence to whether electronic transport or accumulation are linked to substrate polarity. Polar, wurtzite materials InN, GaN, AlN, and ZnO also exhibit piezoelectric properties [71], inviting explorations of  $\text{ZnSn}_x\text{Ge}_{1-x}\text{N}_2$  as piezoelectric materials. Probing electronic response to mechanical deformation of films from polar and non-polar GaN and sapphire substrates for piezoelectric potential is another research opportunity.

## Chapter 6

# Chemical and electrochemical stability and non-aqueous electrochemistry

The chemical and electrochemical stability of semiconductor materials have great impact on their employability in devices. Knowledge of both are useful in order to control material composition, electronic properties, and even material morphology. The ability to etch away surface oxides and contaminants, and perform surface treatments to tailor interfaces is valuable to semiconductor device preparation. Understanding these treatments enables more control over interface states that may otherwise induce Fermi level pinning from surface states or surface contamination- elements that can create conduction band spikes, valence band spikes, or shunting avenues and cause poor carrier transport.

In general, nitride materials have shown high chemical stability to solvents, acids, and bases [17]. High temperature acid baths and photoelectrical chemical etching are examples of conditions needed to etch some metal nitrides. In this chapter, the chemical stability of sputtered  $\text{ZnSnN}_2$  and  $\text{ZnSn}_x\text{Ge}_{1-x}\text{N}_2$  and electrochemical stability of sputtered  $\text{ZnSnN}_2$  are explored. These initial studies are to help evaluate the potential for various etchants for the Zn-IV-Nitrides and the potential for them to be employed in photoelectrolysis as either catalysts or light absorbers.

## 6.1 Chemical stability

Sputtered  $\text{ZnSn}_x\text{Ge}_{1-x}\text{N}_2$  thin-films have demonstrated chemical stability with various solvents, acids, and bases. Solvents including acetonitrile, isopropanol, methanol, acetone, and water did not induce any corrosion at ambient conditions. For acidic conditions, films set in concentrated sulfuric and nitric acid for one day do not exhibit immediate damage. However, the  $\text{ZnSn}_x\text{Ge}_{1-x}\text{N}_2$  sputtered films have etched in concentrated HF and HCl solutions and 500 nm films will dissolve or delaminate and dissolve within a day. Etching appears inhomogeneously (Figure 6.1) and is most likely caused by the nanocrystalline film structure. Thus, it is unclear whether grain boundaries or certain crystal orientations are readily etched. AFM of the etched surfaces did not reveal any preferential etch face or morphology. There is also the possibility that oxides are involved in the etching process since ZnO, SnO, and  $\text{SnO}_2$  have solubility in strong HCl [72, 73]. A decomposition reaction would conceivably produce soluble ZnCl and  $\text{SnCl}_4$  in addition to some nitrogen compound or nitrogen gas.

For basic conditions, concentrated aqueous solutions of potassium hydroxide and sodium hydroxide dissolve  $\text{ZnSnN}_2$  and  $\text{ZnSn}_x\text{Ge}_{1-x}\text{N}_2$  films after a day. Solvated  $\text{NaZn}(\text{OH})_3$  and  $\text{Na}_2(\text{Sn}(\text{OH})_6)_2$  and their potassium variants are probable products [74]. After one day in concentrated ammonium hydroxide, the same dissolution was not observed, as ammonium hydroxide is a weaker base than the strong alkali bases. In conclusion, these experiments have demonstrated that strong acids and strong bases may be easily used as  $\text{ZnSn}_x\text{Ge}_{1-x}\text{N}_2$  etchants.

## 6.2 Non-aqueous photoelectrochemistry

Liquid provide conformal contacts at interfaces at a variety of work functions by changing the interacting redox couples dissolved in solution. These are advantages over solid-state contacts, which can produce unfavorable interface states from lattice mismatching or alloying with the deposited material. Liquid contacts were used to

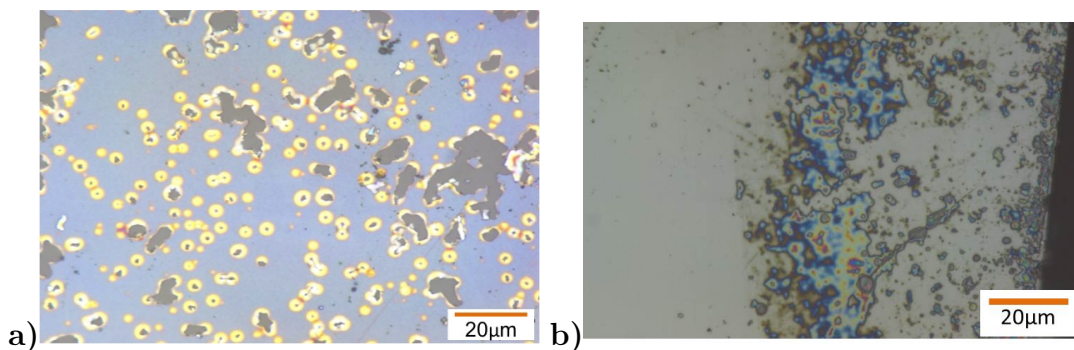


Figure 6.1: Optical micrographs of sputter-fabricated  $\text{ZnSnN}_2$  films on sapphire after sitting in a) 10% HF solution and b) concentrated HCl. Pitting in the film is due to  $\text{ZnSnN}_2$  dissolving in these acids.

test the photoactivity of  $\text{ZnSnN}_2$  by non-aqueous photoelectrochemistry.

$\text{ZnSnN}_2$  electrodes were fabricated by cutting  $\sim 1$  square centimeter samples of the thin films on sapphire. Each sample was electrically contacted by painting silver paint on the film at the edges. A wire was adhered with silver paint to the back of the substrate such that it made electrical connection with the  $\text{ZnSnN}_2$  film. Hysol epoxy was applied to insulate the exposed wire and silver paint and to solidify a scaffold to a glass tube. The glass tube was the conduit for the wire through a teflon thermometer adapter and out of the electrochemical cell. A platinum wire reference electrode and a platinum mesh counter electrode were used. Non-aqueous electrochemical cell preparation and experiments were performed in an argon environment. Redox couples and 1 M lithium perchlorate, functioning as a supporting electrolyte, were dissolved in acetonitrile. Three redox couples at three different work functions were used. A 25 mM/2 mM cobaltocene/cobaltocenium hexafluorophosphate redox couple ratio has an electrochemical potential  $\sim 3.7$  eV below vacuum, while a 25 mM/2-3 mM ferrocene/ferrocenium hexafluorophosphate ratio has an electrochemical potential  $\sim 5$  eV below vacuum. A similar ratio for acetyl ferrocene/acetyl ferrocenium gives an electrochemical potential  $\sim 5.5$  eV below vacuum.

A photoelectrochemical cell was setup as in Figure 6.2 with stirring throughout all measurements. Cyclic voltammetry performed show  $\text{ZnSnN}_2$  ohmically contacted to all redox couple solutions used (Figure 6.3). Several  $\text{ZnSn}_x\text{Ge}_{1-x}\text{N}_2$  electrodes at

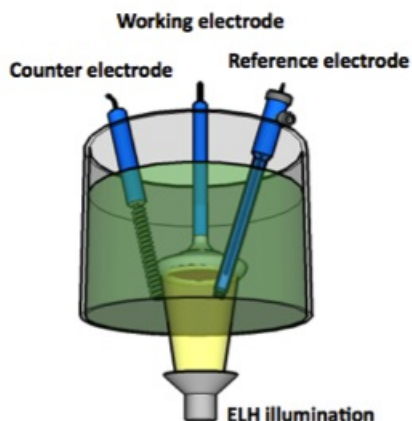


Figure 6.2: Photoelectrochemical cell with three-electrode setup. Image credit: CX Xiang

higher tin compositions were fabricated and tested, and also showed ohmicity with all redox couples. Ohmic results occurred both in dark and illuminated conditions and were probably due to the material degeneracy. Illumination with an ELH lamp produced only a small slope increase in the IV curve, seen in Figure 6.4, indicating photoconductivity. These results qualitatively agree with those found for solid-state contacts. Chronoamperometry of the photoelectrochemical cells could not reproduce the solid state findings because the background electronic noise was too high.

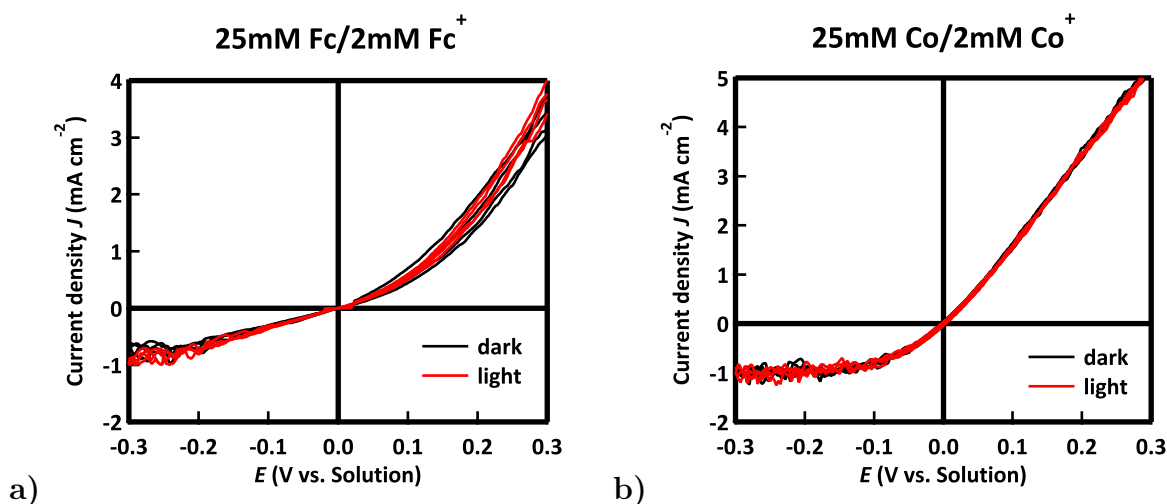


Figure 6.3: Photoelectrochemical devices in a) ferrocene and b) cobaltocene cells. ZnSnN<sub>2</sub> electrodes display ohmic behavior for both redox couples. The smaller concentrations of oxidized species (FcP<sub>2</sub><sup>+</sup> and CoCp<sub>2</sub><sup>+</sup>) cause the limiting current at negative potentials. No photoresponse is apparent.

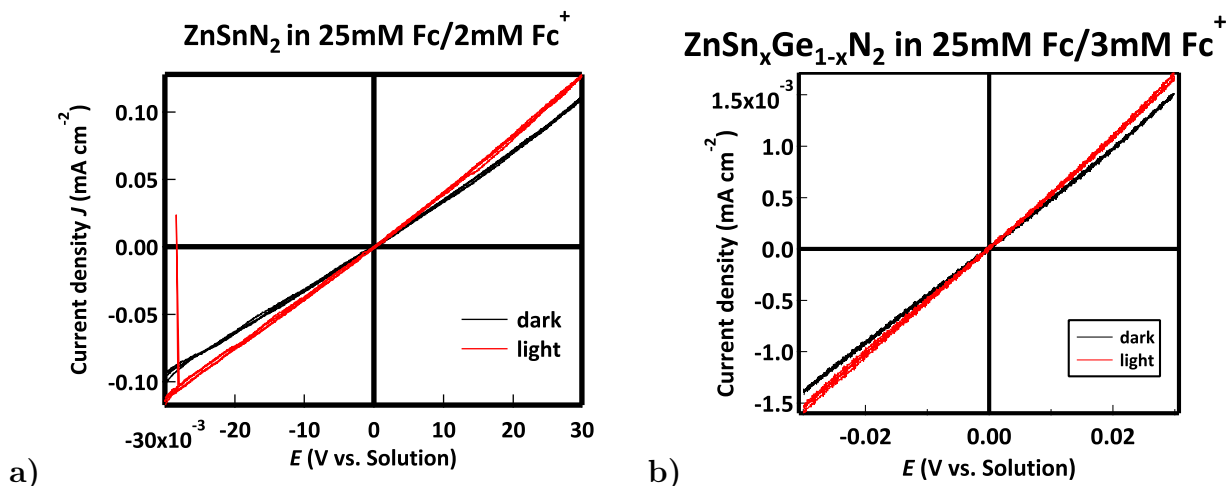


Figure 6.4: Photoelectrochemical tests of a) ZnSnN<sub>2</sub> and b) ZnSn<sub>x</sub>Ge<sub>1-x</sub>N<sub>2</sub> electrodes. A small photoresponse is apparent for both materials.

### 6.3 Aqueous electrochemistry

Regenerative non-aqueous photoelectrochemistry indicated lack of junction formation with ZnSnN<sub>2</sub>, though gave consistent performance without signs of corrosion. Electrochemical stability in non-aqueous systems generally produce fewer deleterious decomposition side reactions, which is why they are used as evaluatory systems. Aqueous solutions, having greater possibility for corrosive or oxidative side reactions instead of electron/hole exchanges with a regenerative redox couple, often produce corroded or oxidized semiconductor electrodes.

Stability tests in aqueous solutions, in the dark and in ambient air, were performed to see how ZnSnN<sub>2</sub> films would sustain in the more reactive aqueous electrolyte. The ferricyanide/ferrocyanide redox couple was used as a regenerative redox couple and without supporting electrolyte. 50 mM potassium ferricyanide and 350 mM potassium ferrocyanide were dissolved in 30mL of NanoPure water, providing a solution potential at about -5 eV below vacuum level, equivalent to approximately -0.3 V vs the normal hydrogen electrode (NHE). The redox ratio provides a higher concentration of ferrocyanide reduced species for the n-type semiconductor's photogenerated holes to potentially oxidize.

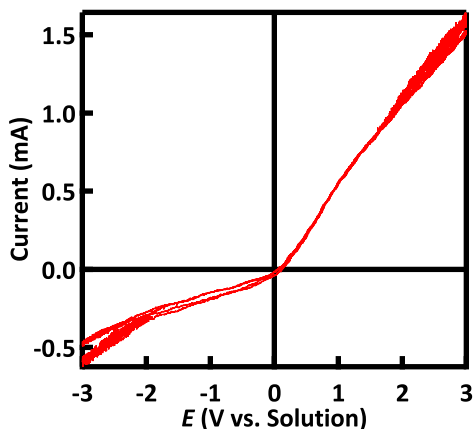


Figure 6.5: Cyclic voltammograms for a  $\text{ZnSnN}_2$  electrode in aqueous media. The decrease in current over two repeated cycles indicates that the electrode is affected by corrosion or oxidation. At  $-2\text{V}$  vs the solution potential, hydrogen bubbles begin to evolve.

Repeated cyclic voltammograms (CVs), shown in Figure 6.5, of  $\text{ZnSnN}_2$  electrodes were taken to find the range of hydrogen evolution. Although NHE was theorized to be within  $1\text{ V}$  of the solution potential, hydrogen bubbles did not begin to evolve until  $-2\text{ V}$  vs the solution potential due to internal resistances and overpotentials. The CVs also show some instability since they don't overlay exactly on top of each other. To discern whether performance degradation was purely oxidative or purely reductive, CVs of fresh  $\text{ZnSnN}_2$  electrodes were tested in only anodic conditions and only cathodic conditions, seen in Figure 6.6. The curves show that both regions have performance decay, so oxidative and reductive corrosion both exist when using a  $2\text{ V}$  range from the  $0\text{ V}$  solution potential. However,  $\text{ZnSnN}_2$  films were more stable with repeated CVs performed within  $\pm 1\text{ V}$  of the solution potential. Chronoamperometry stability test results at select potentials were inconsistent, potentially because of leakages that developed at the edges of the thin film and epoxy.

After electrochemical tests, x-ray photoelectron spectroscopy was performed on the electrodes to determine the chemical composition and elemental oxidation states. Initial results do not denote any obvious corrosion mechanisms.

Overall, aqueous electrochemistry with a fast ferri/ferrocyanide redox couple has demonstrated that the sputtered, nanocrystalline  $\text{ZnSnN}_2$  films are not entirely stable

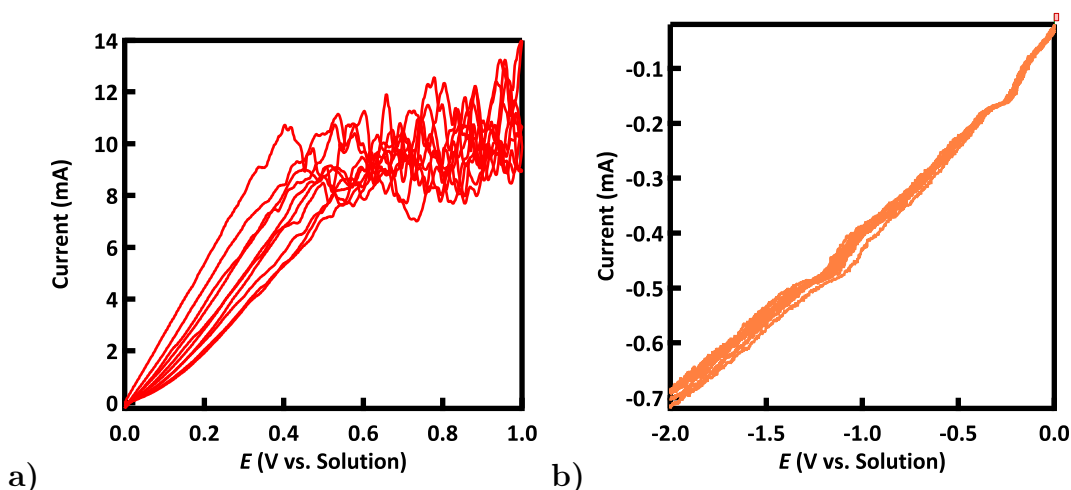


Figure 6.6: Cyclic voltammograms for fresh  $\text{ZnSnN}_2$  electrodes in a) the anodic region and b) the cathodic region in aqueous media. Oxidative effects may be the cause of the current decrease after multiple sweeps in a), while degradation through reductive pathways may be the case for b). The current values differ because they are not normalized to electrode areas, and because there is less ferricyanide for reduction to occur. Thus, the cathodic instability is less dramatic.

in an aqueous environment and have high overpotentials, so would also not work well as an oxygen evolution reaction catalyst or a hydrogen evolution reaction catalyst. MBE films have not been tested, and may provide different results with fewer probable areas of instability, like grain boundaries. If improvements in the photoactivity of the  $\text{ZnSn}_x\text{Ge}_{1-x}\text{N}_2$  films are accomplished, and appropriate protection layers for the  $\text{ZnSn}_x\text{Ge}_{1-x}\text{N}_2$  films are found, then the Zn-IV-Nitride materials may be used as light absorbers in photoelectrochemical cells.

## Chapter 7

# Summary and conclusions

In summary,  $\text{ZnSn}_x\text{Ge}_{1-x}\text{N}_2$  thin films that were fabricated for  $0 \leq x \leq 1$  have tunable band gaps across visible-light wavelengths and do not phase segregate, providing an advantage for the potential device uses of the II-IV-Nitrides relative to  $\text{In}_x\text{Ga}_{1-x}\text{N}$ . This thesis has explored developments in fabrication of  $\text{ZnSn}_x\text{Ge}_{1-x}\text{N}_2$  alloys by three-target co-sputtering and molecular beam epitaxy, the structural and optoelectronic characterization and the solid-state and photoelectrochemical devices produced from the thin films. Initial fabrication was based on the reactive radio-frequency (RF) sputtering technique, was limited to two-target sources, and produced nanocrystalline films. Progression to three-target reactive RF co-sputtering for greater stoichiometric control has been presented, where three-target co-sputtered alloys follow the structural and optoelectronic trends of the initial alloy series. Three-target sputtering further enabled synthesis of alloys having  $< 10\%$  atomic composition ( $x < 0.4$ ) of tin, which exhibited non-degenerate doping as confirmed by low-temperature resistivity measurements. Existence of a non-degenerate alloy regime provided motivation to continue studying and improving the n-type nanocrystalline films.

The electronic structure of sputtered thin-film surfaces for the alloy series were characterized by photoelectron spectroscopy to measure their work functions for device implementation. Using UPS, the work function of reactive RF sputtered  $\text{ZnSnN}_2$  thin-film surfaces was measured to be  $4.04 \pm 0.09$  eV versus vacuum, with a VBM at  $1.22 \pm 0.09$  eV below the Fermi level, which agree with XPS derived measurements. Although minor surface contamination was present ( $< 4\%$  O, C), the freshly vacuum-

transferred values most accurately represent the  $\text{ZnSnN}_2$  surface work function. The work function and valence band onset, combined with band gap measurements, relate the band positions for the  $\text{ZnSnN}_2$  surface versus vacuum. This relative band alignment of  $\text{ZnSnN}_2$  versus vacuum is valuable as it allows predictions for  $\text{ZnSnN}_2$  interactions with electrochemical potentials of other semiconductors, metals, and redox couples. However, surface states cause band bending and put the  $\text{ZnSnN}_2$  Fermi level towards mid-gap, instead of at its bulk degenerate position, convoluting the actual conduction and valence band positions. Though surface states diminish the accuracy of the band positions, the  $\text{ZnSnN}_2$  PES data furnishes guidance for future surface preparation studies to create quality interfaces for devices.

Unfortunately, low electronic mobilities, degenerate carrier concentrations, and limited photoresponse may stem from the defective and nanocrystalline nature of the sputtered films. To improve crystalline quality, films were grown by molecular beam epitaxy (MBE). MBE  $\text{ZnSn}_x\text{Ge}_{1-x}\text{N}_2$  films on sapphire and GaN were epitaxially grown, exhibiting hexagonal symmetry. The films displayed single-crystalline quality, as seen in HRTEM cross sections, which produced higher electronic mobilities, and slightly lower carrier concentrations. However,  $\text{ZnSnN}_2$  films were still degenerate and  $\text{ZnSn}_x\text{Ge}_{1-x}\text{N}_2$  films followed a similar resistivity trend to the sputtered films. Raman spectroscopy of these well structured MBE films revealed that the MBE films, like the sputtered films, still exhibited disordered lattice properties from anti-site defects or mixed layer stacking. Anti-site defects can result in unforeseen defect bands in the band structure that can act as donors or traps, disrupting the ideal direct band gap materials expected from simulation, and influencing the carrier lifetimes and photoresponse. Still, devices from both sputter deposition and MBE exhibited some photoresponse, providing a positive outlook for employment of  $\text{ZnSn}_x\text{Ge}_{1-x}\text{N}_2$  alloys in solar cells or photon sensors.

Looking forward, MBE films can enable critical scientific discoveries of  $\text{ZnSn}_x\text{Ge}_{1-x}\text{N}_2$  phenomena. For the analogous III-Nitrides, it was not until after experiments were performed on InN MBE films that InN's surface electron accumulation layer and Burstein-Moss Effect were discovered. These same efforts on Zn-IV-Nitride MBE

films can reveal if the Zn-IV-Nitrides will carry over optoelectronic trends from the III-Nitrides. Additionally, development of MBE Zn-IV-Nitrides with thicker films and higher temperature growths would provide studies regarding ordering of lattice sites and layer stacking. Results of these studies will enable understanding in the influence of imperfect ordering on semiconducting properties in ternary and quaternary Zn-IV-Nitride compounds, and help reveal the full capability for Zn-IV-Nitrides to be used as an earth-abundant semiconductors that fill the Green Gap and can be used as alternatives to  $\text{In}_x\text{Ga}_{1-x}\text{N}$ .

# Bibliography

- [1] JW Shon, J Ohta, K Ueno, A Kobayashi, and H Fujioka. *Sci. Rep.*, 4:5325, 2014.
- [2] NA El-Masry, EL Piner, SX Liu, , and SM Bedair. *Appl. Phys. Lett.*, 72(1), 1998.
- [3] Vinod Kumar Khanna. *Fundamentals of Solid-State Lighting*. CRCPress/Taylor and Francis, Florida, 2014.
- [4] MR Krames et al. *J. Display Technology*,, 3(2), 2007.
- [5] Z Deng, Y Jiang, Z Ma, W Wang, H Jia, J Zhou, and H Chen. *Scientific Reports*, page 3389, 2013.
- [6] A Punya and WRL Lambrecht. *Phys. Rev. B*, 84:165204, 2011.
- [7] KT Delaney, SK Shukla, and NA Spaldin. First-principles theoretical assessment of earth-abundant nitrides for photovoltaic and optoelectronic applications using hybrid density functionals.
- [8] *CRC Handbook of Chemistry and Physics, Internet Version, 95th ed.* CRC-Press/Taylor and Francis, Florida, 2015.
- [9] L Lahourcade, N Coronel, K Delaney, SK Shukla, NA Spaldin, and HA Atwater. *Adv. Mater.*, 25:2562, 2013.
- [10] N Feldberg, JD Aldous, WM Linhart, LJ Phillips, K Durose, PA Stampe, RJ Kennedy, DO Scanlon, G Vardar, RL Field III, TY Jen, RS Goldman, TD Veal, and SM Durbin. *Appl. Phys. Lett.*, 103:042109, 2013.

- [11] P Quayle, K He, J Shan, and K Kash. Synthesis, lattice structure, and band gap of znsnn2. *MRS Communications*, 3:135, 2013.
- [12] KT Delaney, SK Shukla, and NA Spaldin. First-principles theoretical assessment of earth-abundant nitrides for photovoltaic and optoelectronic applications using hybrid density functionals. *to be submitted*, 2016.
- [13] Punya and WRL Lambrecht. Quasiparticle band structure of zn-iv-n2 compounds. *Phys. Rev. B.*, 84:165204, 2011.
- [14] N Feldberg, JD Aldous, WM Linhart, LJ Phillips, K Durose, PA Stampe, RJ Kennedy, DO Scanlon, G Vardar, RL Field III, TY Jen, RS Goldman, TD Veal, and SM Durbin. Growth, disorder, and physical properties of znsnn2. *Appl. Phys. Lett.*, 103:042109, 2013.
- [15] N Feldberg, JD Aldous, PA Stampe, RJ Kennedy, TD Veal, and SM Durbin. *J. Electron. Mater.*, 43(4):884, 2014.
- [16] L Lahourcade, N Coronel, K Delaney, SK Shukla, NA Spaldin, and HA Atwater. Structural and optoelectronic characterization of rf sputtered znsnn2. *Advanced Materials*, 25:2562, 2013.
- [17] S Strite and H Morkoc. *J. Vac. Sci. Technol., B: Microelectron. Nanometer Struct.*, 10:1237, 1992.
- [18] NC Coronel. Earth abundant zinc-iv-nitride semiconductors. *Caltech Thesis*, 2015.
- [19] M Wintenberger, M Maunaye, and Y Laurent. Groupe spatial et ordre des atomes de zinc et de germanium dans zngen2. *Mater. Res. Bull.*, 8:1049, 1973.
- [20] M Maunaye and J Lang. *Mater. Res. Bull.*, 5:793, 1970.
- [21] WL Larson, HP Maruska, and DA Stevenson. *J. Electrochem. Soc.*, 121(12):1673, 1974.

- [22] K Du, C Bekele, CC Hayman, JC Angus, P Pirouz, and K Kash. *J. Crystal Growth*, 310:1057, 2008.
- [23] T Endo, Y Sato, E Takizawa, and M Shimada. *J. Mater. Sci. Lett.*, 11:424, 1992.
- [24] T Misaki, A Wakahara, H Okada, and A Yoshida. *J. Crystal Growth*, 260:125, 2004.
- [25] S Kikawa and H Morisaka. *Solid State Commun.*, 112(9):513, 1999.
- [26] N Coronel, L Lahourcade, KT Delaney, A Shing, and HA Atwater. *IEEE Photovoltaics Specialist Conference*, page 3204, 2011.
- [27] AM Shing, NC Coronel, NS Lewis, and HA Atwater. Semiconducting  $\text{ZnSn}_{1-x}\text{Ge}_x$  alloys prepared by reactive radio-frequency sputtering. *APL MATERIALS*, 3:076104, 2015.
- [28] AN Fioretti, A Zakutayev, H Moutinho, C Melamed, JD Perkins, A Norman, M Al-Jassim, E Toberer, and AC Tamboli. *J. Mater. Chem. C*, 2015.
- [29] P Sharma, K Sreenivas, and KV Rao. *J. Appl. Phys.*, 93(7):3963, 2003.
- [30] S Kumar, V Gupta, and K Sreenivas. *Nanotechnology*, 16:1167, 2005.
- [31] A Bhatnagar, YH Kim, D Hesse, and M Alexe. *Nanoletters*, 14:5224, 2014.
- [32] M Tarun, F Selim, and M McCluskey. *Phys. Rev. Lett.*, 111:187403, 2013.
- [33] CH Qiu and JI Pankove. *Appl. Phys. Lett.*, 70(15):1983, 1997.
- [34] V Dumitru, C Morosanu, V Sandu, and A Stoica. Optical and structural differences between rf and dc  $\text{Al}_x\text{In}_{1-x}$  magnetron sputtered films. *Thin Solid Films*, 359(1):17–20, 2000.
- [35] PC Quayle, EW Blanton, A Punya, GT Junno, K He, L Hand, H Zhao, J Shan, WRL Lambrecht, and K Kash. Charge-neutral disorder and polytypes in heterovalent wurtzite-based ternary semiconductors. *Phys. Rev. B*, 91:205207, 2015.

- [36] TJ Peshek, TR Paudel, K Kash, and WRL Lambrecht. Vibrational modes in zngen2: Raman study and theory. *Phys. Rev. B*, 77:235213, 2008.
- [37] R Viennois, T Taliercio, V Potin, A Errebbahi, B Gil, S Charar, A Haidoux, and JC Tedenac. Prospective investigations of orthorhombic zngen2 synthesis, lattice dynamics and optical properties. *Mat. Sci. and Engineering B*, 82:45–49, 2001.
- [38] D Briggs and M Seah. Practical surface analysis. *Wiley*, 1990.
- [39] D Briggs. Handbook of x-ray and ultraviolet photoelectron spectroscopy. *Hayden*, 1977.
- [40] RL Anderson. Experiments on ge-gaas heterojunctions. *Solid-St. Electron.*, 5:341, 1962.
- [41] AG Milnes and DL Feucht. Heterojunctions and metal semiconductor junctions. Academic Press, Inc, 1972.
- [42] MJ Adams and A Nussbaum. A proposal for a new approach to heterojunction theory. *Solid-St. Electron*, 22:783–791, 1979.
- [43] A Kudo and Y Miseki. Heterogeneous photocatalyst materials for water splitting. *Chem. Soc. Rev*, 38:253–278, 2009.
- [44] L Yang, H Zhou, T Fan, and D Zhang. Semiconductor photocatalysts for water oxidation: current status and challenges. *Phys. Chem. Chem. Phy*, 16:6810–6826, 2014.
- [45] MG Walter et al. Solar water splitting cells. *Chem. Rev.*, 110:6446–6473, 2010.
- [46] R Schlaf, H Murata, and ZH Kafafi. Work function measurements on indium tin oxide films. *J. Elect. Spect. and Rel. Phen.*, 120:149–154, 2001.
- [47] M Schulz, E Klausmann, and A Hurre. Correlation of surface states with impurities. *CRC Critical Reviews in Solid State Sciences*, 5:3:391–325, 1975.

- [48] CT Au, W Hirsch, and W Hirschwald. Adsorption of carbon monoxide and carbon dioxide on annealed and defect zno(000-1) surfaces studied by photoelectron spectroscopy (xps and ups). *Surface Science*, 197(3):391–401, 1988.
- [49] F Streicher, S Sadewasser, and MC Lux-Steiner. Surface photovoltage spectroscopy in a kelvin probe force microscope under ultrahigh vacuum. *Rev. Sci. Instrum.*, 80:013907, 2009.
- [50] GV Hansson and RIG Uhrberg. Photoelectron spectroscopy of surface states on semiconductor surfaces. *Surface Science Reports*, 9:197–292, 1988.
- [51] PT Andrews and LA Hisscott. X-ray photoelectron spectroscopy of some cu-zn alloys. *J. Phys. F.: Metal Phys.*, 5:1568–1572, 1975.
- [52] J Kubota and K Domen. Photocatalytic water splitting using oxynitride and nitride semiconductor powders for production of solar hydrogen. *ECS Interface*, 24(2):57–62, 2013.
- [53] F Vaz, N Martin, and M Fenker. Metallic oxynitride thin films by reactive sputtering and related deposition methods. *Bentham Science Publishers*, 2013.
- [54] H Moormann, D Kohl, and G Heiland. Work function and band bending on clean cleaved zinc oxide surfaces. *Surface Science*, 80:261–264, 1979.
- [55] K Jacobi, G Zwicker, and A Gutmann. Work function, electron affinity and band bending of zinc oxide surfaces. *Surface Science*, 141(1):109–125, 1984.
- [56] M Batzill and U Diebold. The surface and materials science of sno2. *Prog. Surf. Sci.*, 79:47–154, 2005.
- [57] T Sahm, A Gurlo, N Barsan, and U Weimar. Basics of oxygen and sno2 interaction, work function change and conductivity measurements. *Sensor and Actuators B: Chemical*, 118(1-2):78–83, 2006.

- [58] K Burger, F Tschismarov, and H Ebel. Xps/esca applied to quick-frozen solutions i.- a study of nitrogen compounds in aqueous solutions. *J. Electron Spectrosc. Relat. Phenom.*, 10:461, 1977.
- [59] VI Nefedov, IA Zakharova, II Moiseev, MA Poraikoshits, MN Vargoftik, and AP Belov. Study of palladium complex compounds by x-ray photoelectron spectroscopy. *Zh. Neorg. Khimil*, 18:3264, 1973.
- [60] DE Eastman and JK Cashion. Photoemission from cu, ag, and au in the 10- to 27-ev energy range. *Phys. Rev. Lett.*, 24(7):310–313, 1970.
- [61] CM Eggleston, JJ Ehrhardt, and W Stumm. Surface structural controls on pyrite oxidation kinetics: An xps-ups, stm, and modeling study. *American Mineralogist*, 81:1036–1056, 1996.
- [62] JL Freeouf and DE Eastman. Photoemission measurements of filled and empty surface states on semiconductors and their relation to schottky barriers. *CRC Critical Reviews in Solid State Sciences*, 5(3):245–258, 1975.
- [63] K Nomura, T Kamiya, E Ikenaga, H Yanagi, K Kobayashi, and H Hosono. Depth analysis of subgap electronic states in amorphous oxide semiconductor, a-in-ga-zn-o, studied by hard x-ray photoelectron spectroscopy. *J. Appl. Phys.*, 109:073726, 2011.
- [64] LF Wagner and WE Spicer. Observation of a band of silicon surface states containing one electron per surface atom. *Phys. Rev. Lett.*, 28(21):1381–1384, 1972.
- [65] JN Miller, I Lindau, and WE Spicer. Absence of band-gap surface states on clean amorphous silicon. *Phil. Mag. B*, 43(2):273–282, 1981.
- [66] DR Palmer, SR Morrison, and CE Dauenbaugh. Density and energy of surface states on cleaved surfaces of germanium. *Phys. Rev.*, 129(2):08–613, 1963.

- [67] TD Veal, CF McConville, and WJ Schaff. *Indium Nitride and Related Alloys*. CRC Press, Florida, 2010.
- [68] R Fornari and L Sorba. Crystal growth of materials for energy production and energy-saving applications. *Edizioni ETS*, Pisa, 2011.
- [69] RFC Farrow. Molecular beam epitaxy: Applications to key materials. *Noyes Publications*, Park Ridge, NJ, 1995.
- [70] N Dietz, M Alevli, R Atalay, G Durkaya, R Collazo, J Tweedie, S Mita, and Z Sitar. *APL*, 92:041911, 2008.
- [71] ET Yu, XZ Dang, PM Asbeck, and SS Lau. *J. Vac. Sci. Technol. B*, 17(4), 1999.
- [72] HT Fang, X Sun, and Y Chu. Synthesis and room-temperature hydrogen sensing properties of polycrystalline  $\text{SnO}_2$  coating on multi-walled carbon nanotubes. 2007.
- [73] Jorj Ian Owen. *Growth, Etching, and Stability of Sputtered ZnO:Al for Thin Film Silicon Solar Cells*. Forschungszentrum Julich GmbH, Julich, Germany, 2011.
- [74] AL Chen, D Xu, XY Chen, WY Chang, and XH Liu. *Trans. Nonferrous Met. Soc. China*, 22:1513–1516, 2012.
- [75] A Punya, TR Paudel, and WRL Lambrecht. *Phys. Status Solidi C*, 8:2492, 2011.
- [76] AF Wright and JS Nelson. *Phys. Rev. B*, 5(12):7866, 1995.
- [77] P Quayle, K He, J Shan, and K Kash. *MRS Commun.*, 3:135, 2013.
- [78] A Punya, TR Paudel, and WRL Lambrecht. Electronic and lattice dynamical properties of  $\text{II-IV-N}_2$  compounds. *Phys. Status Solidi C*, 8:2492, 2011.
- [79] A Punya and WRL Lambrecht. Band offsets between  $\text{ZnGe}_2$ ,  $\text{GaN}$ ,  $\text{ZnO}$ , and  $\text{ZnSnN}_2$  and their potential impact for solar cells. *Phys. Rev. B*, 88:075302, 2013.

- [80] N Coronel, L Lahourcade, KT Delaney, A Shing, and HA Atwater. Earth-abundant znsnxge<sub>1-xn2</sub> alloys as potential photovoltaic absorber materials. *2011 IEEE Photovoltaic Specialist Conference*, 2012:003204–003207, 2012.
- [81] TE Fischer. Determination of semiconductor surface properties by means of photoelectric emission. *Surface Science*, 13(1):30–51, 1969.
- [82] JM Zuo and JC Mabon. Web-based electron microscopy application software: Web-emaps. *Microsc. Microanal.*, 10(Suppl 2), 2004.
- [83] S Al-Hilli. *Sensors*, 9(9):7445–7480, 2009.

# Appendix

Drawings for transfer equipment used with AJA Sputterer load-lock, custom vacuum suitcase, and Kratos Axis Ultra photoelectron spectrometer.

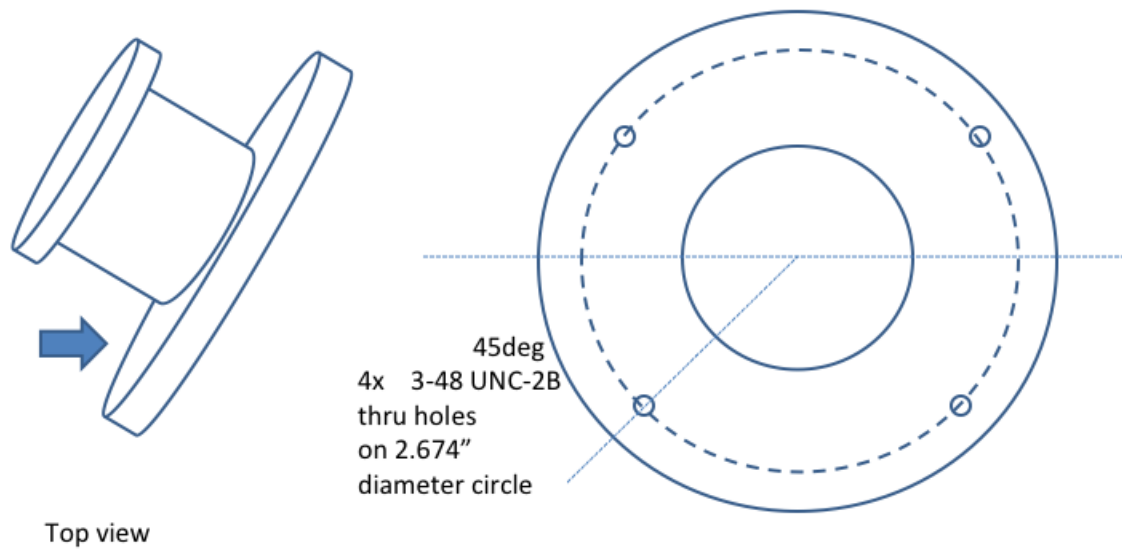


Figure 1: KF Flange for sputterer window.

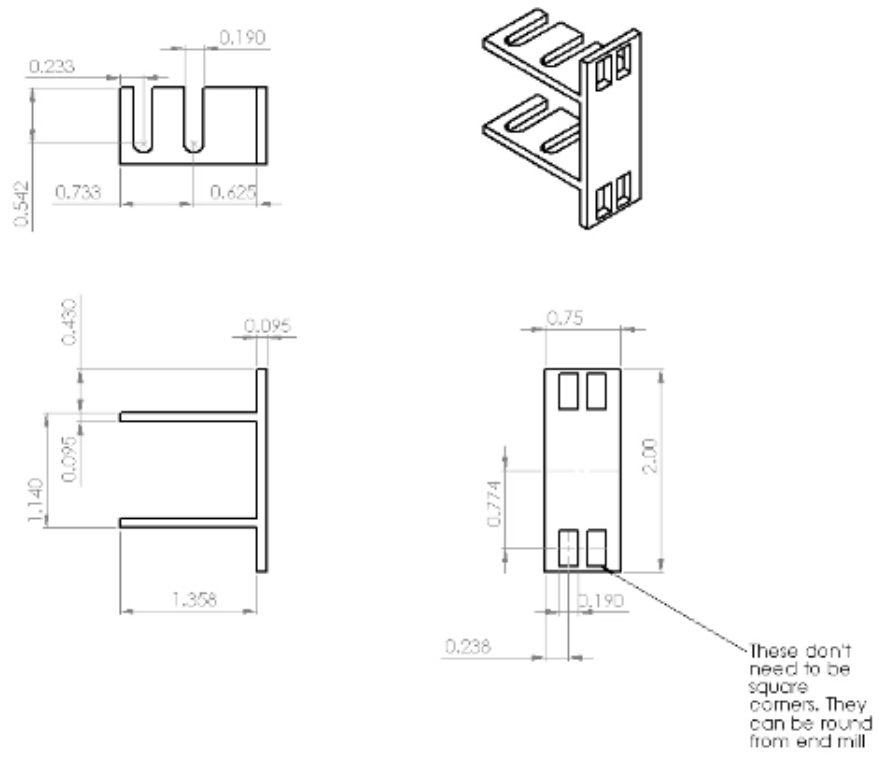


Figure 2: Arm attachment for adjusting the height of the new stage holder.

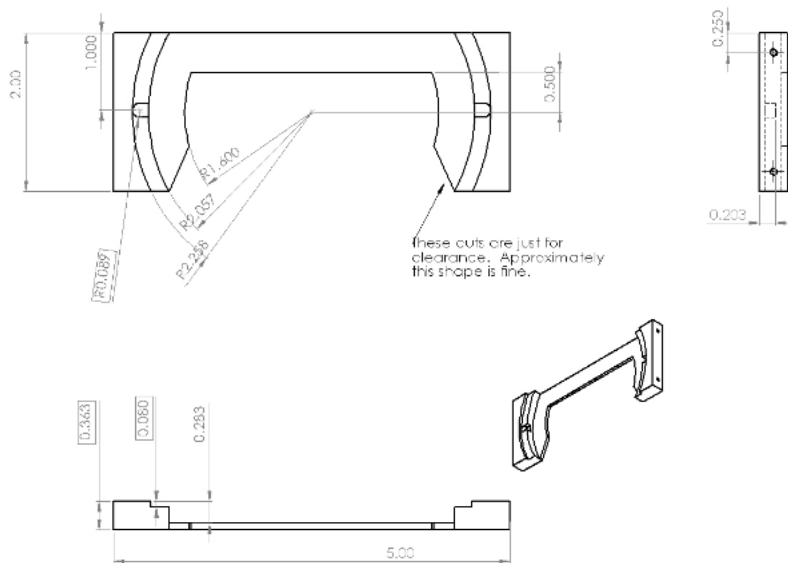


Figure 3: The new stage holder for the sample holder adapter.

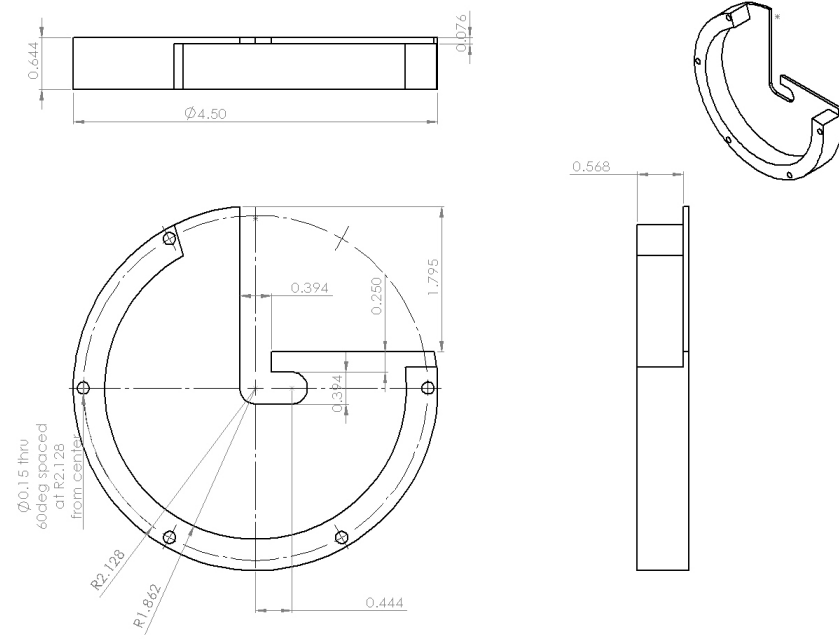


Figure 4: The sample holder adapter for the Kratos sample holder.

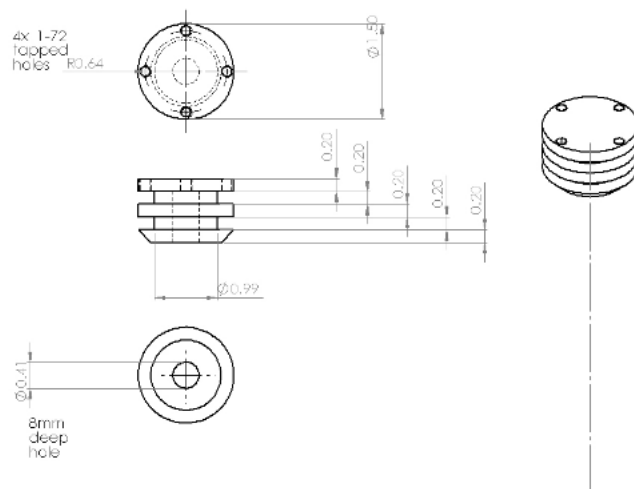


Figure 5: The Cu puck Kratos sample holder.

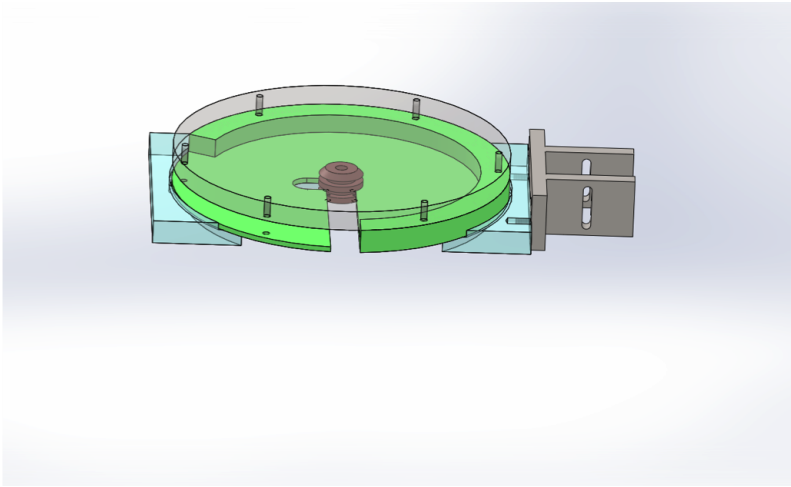


Figure 6: The assembly of sputterer substrate platform (transparent) with sample holder adapter (green) and Kratos sample holder (Cu puck). The substrate platform assembly sits on a new stage holder (light blue), which is held to the sputterer translation arm by the stage support (grey)

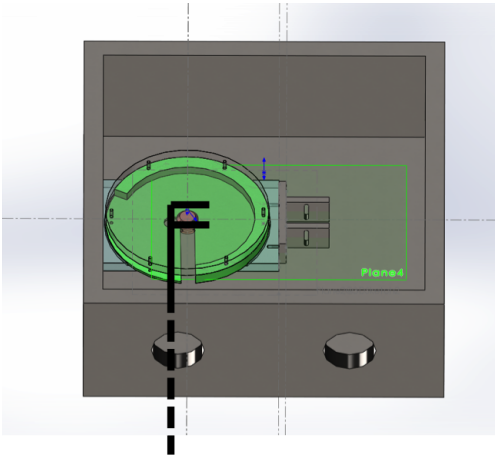


Figure 7: The assembly in the sputterer load-lock and path where the suitcase arm travels.

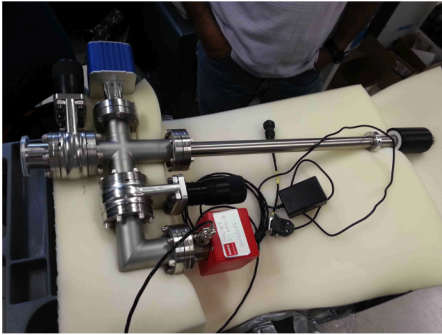


Figure 8: The vacuum suitcase, equipped with a SAES ion and getter pump, used to transfer XPS/UPS samples.